ABSTRACT

Title of dissertation: NOVEL APPLICATIONS OF
HIGH INTENSITY FEMTOSECOND LASERS
TO PARTICLE ACCELERATION
AND TERAHERTZ GENERATION

Andrew G. York, Doctor of Philosophy, 2008

Dissertation directed by: Professor Howard Milchberg
Institute for Research in Electronics and Applied Physics

We have investigated new applications for high intensity femtosecond lasers theoretically and experimentally, including a novel method to accelerate electrons to relativistic energy and a new type of coherent lasing medium for amplification of few-cycle, high energy pulses of terahertz radiation.

We report the development of corrugated 'slow wave' plasma guiding structures with application to quasi-phase-matched direct laser acceleration of charged particles. These structures support guided propagation at intensities up to 2×10^{17} W/cm^2, limited by our current laser energy and side leakage. Hydrogen, nitrogen, and argon plasma waveguides up to 1.5 cm in length with corrugation period as short as 35 μm are generated in extended cryogenic cluster jet flows, with corrugation depth approaching 100%. These structures remove the limitations of diffraction, phase matching, and material damage thresholds and promise to allow high-field acceleration of electrons over many centimeters using relatively small femtosecond lasers. We present simulations that show a laser pulse power of 1.9 TW

should allow an acceleration gradient larger than 80 MV/cm. A modest power of only 30 GW would still allow acceleration gradients in excess of 10 MV/cm.

Broadband chirped-pulse amplification (CPA) in Ti:sapphire revolutionized nonlinear optics in the 90's, bringing intense optical pulses out of large government facilities and into the hands of graduate students in small university labs. Intense terahertz pulses ($\gg 10$ μJ, < 5 cycles), however, are still only produced at large accelerator facilities like Brookhaven National Labs. CPA is theoretically possible for terahertz frequencies, but no broadband lasing medium like Ti:sapphire has been demonstrated for terahertz. Dipolar molecular gases such as hydrogen cyanide (HCN) or nitrous oxide (N_2O), 'aligned' or rotationally excited by intense optical pulses, are a novel and promising medium for amplification of broadband few-cycle terahertz pulses. We present calculations that show rotationally excited molecules can amplify a few-cycle seed pulse of terahertz radiation: a short, intense optical pulse (or sequence of pulses) aligns a dipolar gas (such as HCN), driving the molecules into a broad superposition of excited rotational states. A broadband seed terahertz pulse following the optical pulses can then be amplified on many pure rotational transitions simultaneously. We also discuss plans and progress towards experimental realization of a few-cycle terahertz amplifier.

NOVEL APPLICATIONS OF HIGH INTENSITY FEMTOSECOND LASERS TO PARTICLE ACCELERATION AND TERAHERTZ GENERATION

by

Andrew G. York

Dissertation submitted to the Faculty of the Graduate School of the
University of Maryland, College Park in partial fulfillment
of the requirements for the degree of
Doctor of Philosophy
2008

Advisory Committee:
Professor Howard M. Milchberg, Chair/Advisor
Professor William Dorland
Professor Julius Goldhar
Professor Wendell T. Hill III
Professor Steven Rolston

Dedication

To Kelli, naturally.

Hey Kelli, let me know if you ever notice that I dedicated my thesis to you.

Acknowledgments

First and foremost, this thesis obviously wouldn't be possible without Howard Milchberg. I've learned more in Howard's lab than any other time in my life. Of course, this learning wouldn't have been nearly as fun without Sanjay Varma to share the ups and the downs. My wife Kelli has listened to far more physics than she deserves, and that goes double for my old roommate Ben Cooper, but I think he likes it more. John Palastro, Brian Layer, and Yu-Hsin Chen were amazing colleagues and made so much possible that I could never have done alone, and Matt Aubuchon gives me hope for our lab's future creativity and intelligence. Evan Merkel, Mike Harrington, Chris Pesto, and Darryl Waddy all showed me how much more I could have done with my undergrad years. Thomas Antonsen never locked me and my incessant questions out of his office for some reason, and helped guide my questions in more productive directions more than once. Tom Murphy let me 'borrow' an out-of-print textbook for more than a year, and helped correct several of my grosser misconceptions about fiber optics. Yongzhang Leng's fabrication work made the corrugated waveguide possible, and his kindness and patience made it easier to keep bothering him. Edd Cole taught me everything I know about machining, and tells some pretty cool stories too. Jane Hessing saved me from my own mistakes more times than I can count, retroactively. Finally, I think this thesis owes a lot to my dad flipping over restaurant placemats to show me sine waves, my mom's love of a good puzzle, and my brother being so much better at art that I had to pursue science.

Table of Contents

List of Tables

List of Figures

Chapter 0

Introduction

0.1 High intensity lasers

Multi-millijoule, subpicosecond laser pulses have given scientists amazing ability to observe and manipulate matter. University laboratories have produced laser intensities of more than 10^{22} W/cm^2, corresponding to an electric field of more than 10^{12} V/cm [1], almost 1000 times the electric field that binds an electron in a hydrogen atom. More modest intensities (10^{15} W/cm^2) are routinely achieved by compact commercial laser systems [2]. These compact, intense lasers allow small laboratories to 'push' on electrons with extreme power and precision, driving relativistic electron velocities, deep ionization of atoms and molecules, megavolt plasma temperatures, and even initiating nuclear reactions [3]. At the same time, the ultrashort nature of these pulses allows observation of the resulting dynamics with few-femtosecond time resolution [4], essential for observing such violent motion.

Such short, intense pulses are made possible by several recent advances in laser technology. An optical pulse with duration <100 fs neccesarily has a bandwidth of many nanometers. Titanium sapphire, studied by Moulton *et al.*, [5], is an excellent amplifying medium for such pulses, with an amplification bandwidth extending from 660-986 nm. Combined with the technique of Kerr-lens modelocking, titanium-sapphire oscillators routinely produce trains of optical pulses with duration less

than 30 femtoseconds [6].

Chirped pulse amplification (CPA), invented by Strickland and Mourou [7, 8] in the 1980's, allows these short pulses to be amplified to many joules of energy without damage to their amplifiying medium. CPA uses dispersive optics to reversibly stretch ultrashort pulses to multi-picosecond duration, reducing their intensity to avoid nonlinear effects in amplifier rods. After amplification, similar dispersive optics return the amplified pulses to nearly their original femtosecond duration, giving high energy in a short pulse. Focused to micron-scale spots, these pulses reach enormous energy density despite containing fewer calories of energy than a stick of gum.

0.2   Some of applications of high intensity femtosecond lasers

Femtosecond laser pulses have a tremendous number of applications. The 'Virtual Journal of Ultrafast Science' tracks journal articles related to femtosecond lasers from a variety of journals, and has routinely indexed more than 100 articles each month since 2002 [9], including entries on chemistry, biology, and materials science.

The 1999 Nobel prize in chemistry was awarded for the study of chemical bonds and dynamics on a femtosecond timescale using subpicosecond pulsed lasers [10]. Subpicosecond lasers were used both to initiate and control chemical reactions, and also to probe the resulting behavior.

Intense femtosecond lasers have enabled new kinds of imaging and manip-

ulation in biotechnology. Multiphoton imaging exploits nonlinear absorption to confine fluorescence to the laser's focal region while minimizing heat and photodamage; a sample can be transparent to a converging femtosecond pulse until the pulse focuses tightly enough to exceed the intensity threshold for nonlinear absorption. Nanosurgery exploits a similar technique to destroy targeted regions in a 3-D sample without damaging the surrounding material [11].

Even simple laser ablation can be improved by intense femtosecond pulses. Laser ablation by nanosecond pulses typically heats a target, causing thermal stress. Femtosecond laser ablation ionizes and ablates without depositing much heat, and has been used in dentistry to reduce cracking caused by thermal stresses [12].

The 2005 Nobel prize in physics was awarded for precision spectroscopy, including the 'optical frequency comb'. By stabilizing the round-trip time and dispersion of a femtosecond laser oscillator cavity, the megahertz repetition rate of the cavity can be directly connected to the femtosecond-scale oscillations of the laser pulse, allowing researchers to literally count the number of optical cycles emitted by a source. This gives some of the most precise measurements of time ever made [13].

0.3 Outline of thesis

The compact, inexpensive nature of femtosecond oscillators and chirped pulse amplification has been crucial to all these applications, driving rapid progress by enabling many small labs to work simultaneously on a problem. The lesson is clear: if you can reach higher power, higher energy, shorter pulses, or a new type of beam

with a smaller, cheaper setup, countless applications will quickly follow.

Laser wakefield acceleration [14] uses the extreme intensity of multi-terawatt femtosecond laser pulses to accelerate electrons to relativistic energy. This technology aims to eventually replace enormous microwave-based electron accelerators with laboratory-scale laser systems. However, these multi-terawatt laser systems are much larger and more expensive than gigawatt regenerative amplifiers, and still out of the reach of many small labs and hospitals. In Chapters 1, 2, and 3, we describe our work towards a new kind of laser-based electron accelerator which could function with much smaller lasers but still reach high electron energy.

Chapter 1 briefly surveys the field of electron acceleration. Chapter 2 describes our theoretical work to design our novel acceleration structure, and Chapter 3 details our experimental realization of this structure.

Terahertz generation by amplified femtosecond lasers [15] can produce short pulses that contain only a few cycles of the electromagnetic field. This technolgy is hampered by low conversion efficiency, limiting terahertz pulse energies to microjoule levels, even with terawatt lasers or large electron accelerators. Chapters 4-9 describe our work to create a new kind of terahertz source based on rotating dipolar molecules, which could amplify existing few-cycle terahertz pulses to much higher energies.

Chapter 4 briefly surveys the interaction of intense optical and terahertz pulses with molecular rotation. Chapter 5 describes the details of how we simulate these interactions. Chapter 6 describes our simulation results, which show intense optical pulses can drive a gas of molecules into a rotational population inversion, and Chap-

ter 7 shows how the resulting excited gas can amplify terahertz radiation. Chapter 8 shows some interesting results that suggest optically-aligned molecules could amplify terahertz pulses even without rotational population inversion. Finally, Chapter 9 discusses experimental implementation of these schemes.

Chapter 1

Review of laser-driven particle acceleration

1.1 Direct acceleration by electromagnetic waves

The Stanford Linear Accelerator (SLAC), shown in Figure 1.1, is currently the longest linear accelerator in the world [16]. The accelerator itself is fairly simple, a long copper tube with annular discs partially blocking the tube every few centimeters. Charged particles are accelerated by the E_z field at the center of a TM-mode microwave guided in this axially modulated copper waveguide.

In an ordinary unmodulated metal waveguide, the guided wave phase velocity $v_p = \omega/k$ is greater than c [17], so a charged particle would be accelerated and then decelerated as the wave oscillations pass the particle, giving zero net acceleration. However, each annular copper disc partially reflects microwaves, forming a long chain of coupled microwave resonators. Through careful design, the phase of each resonator is related to the next by just the right amount such that $v_p < c$, and particle and wave speeds can be matched. Called a 'slow wave structure', this type of guide finds wide application in both accelerators and microwave sources [18].

The accelerating gradient of the SLAC structure is limited by the microwave damage threshold of the copper tube. Microwave fields stronger than $\sim 10^7$ V/m breakdown the walls catastrophically. In order to reach high energy (~ 50 GeV), the SLAC structure is roughly two miles long. Amplified femtosecond laser pulses,
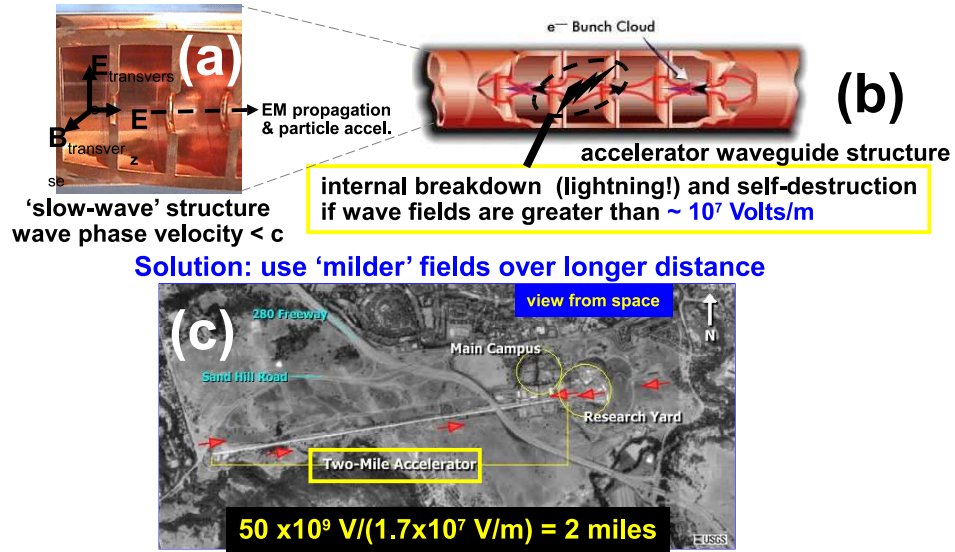
Figure 1.1: The Stanford Linear Accelerator (SLAC) accelerating structure is **(a)** a long copper waveguide filled with discs to control the phase velocity of guided microwaves. **(b)** Breakdown of the copper limits the maximum microwave intensity, so to accelerate electrons to 40 GeV energy, **(c)** an extremely long structure is neccesary.

in comparison, can easily reach intensities of 10^{15} W/cm^2, corresponding to electric field strengths >60 GV/m, and laser intensities $>10^{19}$ W/cm^2 are not uncommon. If some fraction of this field could be used to accelerate electrons, then electron energies comparable to SLAC could be made over meters instead of miles.

A wide variety of structures have been used to allow the exchange of energy between laser radiation and relativistic electrons, from a hydrogen-filled gas cell fed by a conically-focused, radially-polarized nanosecond CO_2 laser [19], to a simple reflective metal tape positioned at the focus of a picosecond laser [20]. While the efficiency and expense of these schemes varies greatly, the electron acceleration gradients they can achieve are ultimately limited by the radiation intensity they can produce and control, and typically are significantly less than 1 MV/cm. Mod-

ern femtosecond lasers based on chirped-pulse amplification [8] can produce focused field strengths in excess of 10 GV/cm. An accelerating structure that could control this field strength would allow enormous acceleration gradients, but no material can survive this intensity un-ionized.

Schemes to use a laser's electric field to accelerate electrons *without* an acceleration structure have been proposed [21], but none have been demonstrated, possibly because they violate the Woodward-Lawson theorem [22, 23] and are therefore impossible. Generally, the electric field of radiation is perpendicular to the propagation direction. A relativistic electron in vacuum can either be phase-matched with radiation, or it can can have a component of velocity parallel to the radiation's electric field, but not both since radiation moves at c in vacuum. Radiation which appears to have a component of its electric field point along its propagation direction can always be described as a superposition of plane waves, which either do not actually move in the apparent propagation direction, or have no component of their electric field pointing in this direction.

1.2   Wakefield acceleration

Laser wakefield acceleration was proposed in 1979 [24] to solve the problems of phase matching and material damage threshold. An intense laser beam cannot accelerate electrons in vacuum [22, 23], and will ionize anything it touches, so high-intensity laser acceleration of electrons must therefore happen in plasma.

The principle of wakefield acceleration is fairly simple: a sufficiently intense
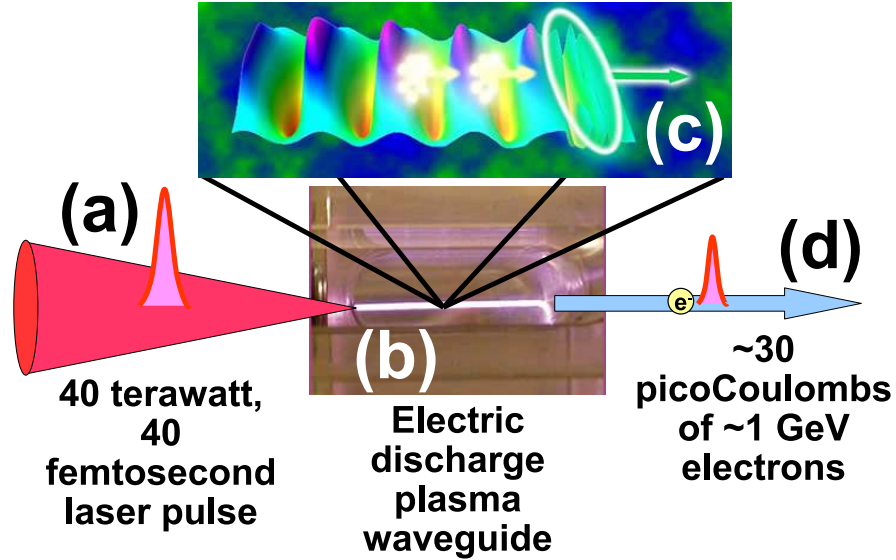
Figure 1.2: **(a)** A 40 TW, 40 fs laser pulse enters **(b)** an electric discharge plasma waveguide, where it drives **(c)** a nonlinear wakefield, which accelerates **(d)** a nearly monoenergetic ~ 30 pC bunch of electrons to ~ 1 GeV energy [26]. Figure adapted and modified from Leemans *et al.*, Nature Physics **2**, 696-699 (2006).

laser pulse propagating in a plasma will deflect electrons to the side as it passes, through the nonlinear ponderomotive force [25]. Heavier ions are nearly unaffected ($> 10^6 \times$ acceleration) by this ponderomotive effect [25], creating a region of net positive charge in the wake of the laser pulse. After the laser pulse is gone, this positive region pulls the expelled electrons back, creating a region of excess negative charge. This transverse motion creates a 'wake' that travels at the group velocity of the driving laser pulse. Even though the laser pulse itself has negligible electric field pointing along the laser propagation direction, the wake produces significant axial electric fields that can point and propagate in the same direction.

Laser wakefield acceleration [24, 27, 28] of electrons to relativistic velocities

is often described as a 'tabletop' experiment [29], promising to make high-energy electrons available outside of large, multi-user accelerator facilities. Recent advances in wakefield acceleration have produced monoenergetic beams [30, 31, 32] and impressive electron energies exceeding 1 GeV [26]. These experiments, however, all use expensive multi-terawatt laser systems that cannot reasonably be considered 'tabletop'.

Figure 1.2 illustrates the setup used by Leemans *et al.* to produce ~ 1 GeV electrons in a few centimeters [26]. A 40 TW, 40 fs laser pulse is injected into an electric discharge plasma waveguide. The waveguide helps suppress diffraction of the laser pulse, enabling high-intensity interaction over many centimeters. The intense pulse nonlinearly drives a wakefield, which has sufficient field strength to accelerate and trap thermal background electrons in the plasma. This accelerator produces a nearly monoenergetic ~ 30 pC bunch of electrons with ~ 1 GeV energy.

1.3 Proposed acceleration scheme

Direct laser acceleration would be an attractive alternative to wakefield acceleration for accelerating relativistic electrons if it weren't for the damage threshold of solid or gaseous accelerating structures [19, 33]. Wakefield acceleration is a nonlinear process and is inefficient at sub-terawatt powers, but direct laser acceleration (a linear process) has no threshold intensity. Small, inexpensive few-mJ chirped-pulse regenerative amplifiers with gigawatt peak power that could never reach the intensity threshold for wakefield acceleration could still be used for direct laser acceleration.

(a)

1 inch (approx.)

(b) 500μm

650 μm

Tube made of plasma. No more "damage threshold"

(c)

Klystron

25 Feet of Earth

Waveguide

Accelerator Structure

Incident radially polarized beam
(arrows show the field line directions)

Plasma Waveguide

Propagation Direction

(d)
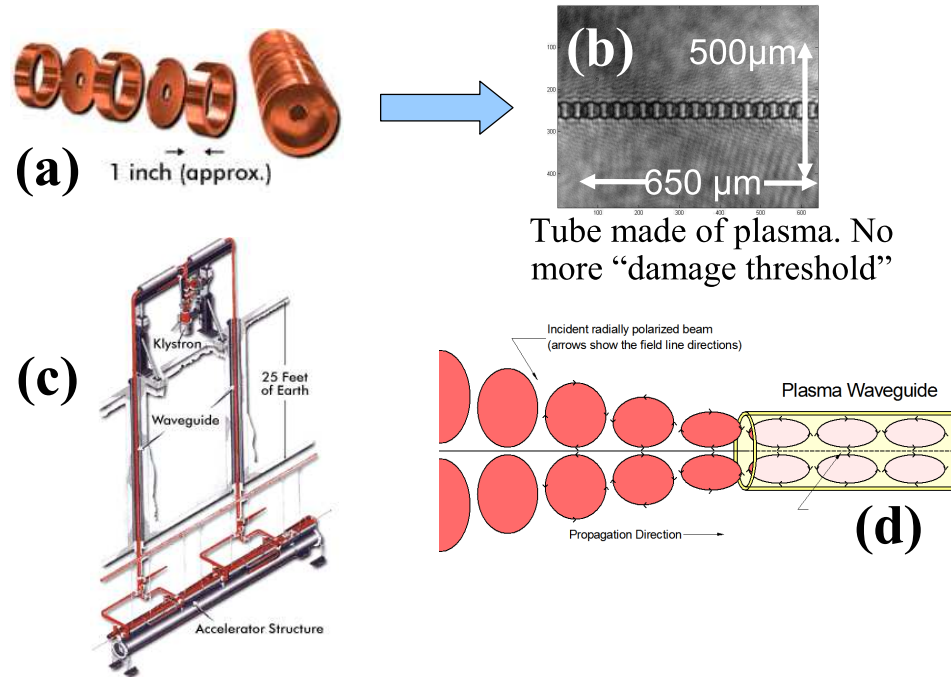
Figure 1.3: Our idea is to replace the SLAC structure, **(a)** a centimeter-scale, kilometers-long microwave-frequency waveguide made of copper, with **(b)** a micron-scale, centimeters-long, optical frequency waveguide made of plasma. Instead of **(c)** megawatt klystrons, we drive the structure with **(d)** gigawatt or terawatt laser pulses.

We describe experimental [34] and theoretical [35] progress towards a practical scheme for direct electron acceleration at multi-MeV/cm gradients by sub-terawatt femtosecond pulsed lasers. The essence of our scheme is illustrated in Figure 1.3. Just as the segmented copper structure of the Stanford Linear Accelerator channels the megawatt power of microwave-frequency klystrons to accelerate electrons over several kilometers [16], we have created a corrugated plasma structure to guide the giga- or terawatt power of optical frequency femtosecond pulses over centimeters. Our simulations show that if this structure is correctly tuned and injected with a radially polarized laser beam and a simultaneously copropagating electron bunch, true 'tabletop' electron acceleration is possible: a laser pulse power of 1.9 TW should allow an acceleration gradient larger than 80 MV/cm, and a modest power of only 30 GW would still allow acceleration gradients in excess of 10 MV/cm.

Just as the annular discs in the SLAC structure control the effective phase velocity of guided microwaves, the corrugations in our plasma guiding structure control the local phase velocity of a guided optical pulse. Unlike any other direct acceleration scheme, our structure is completely ionized and can withstand laser intensity at least six orders of magnitude more than any solid accelerating structure. Unlike wakefield acceleration, we can use smaller, cheaper gigawatt regenerative amplifier laser systems to drive acceleration instead of larger, more expensive multi-terawatt systems. We describe the details of our simulations in Chapter 2

We recently achieved the first ever high intensity optical guiding in an extended corrugated plasma slow wave structure. The application of these structures to coherent electromagnetic wave generation was first discussed in reference [36].

Spontaneous, but uncontrolled modulated channels were reported in reference [37]. We have produced exceptionally stable plasma waveguides with adjustable axial modulation periods as short as 35 μm, where the period can be significantly smaller than the waveguide diameter. The axial modulations can also be extremely sharp and deep, with nearly 100% modulation in plasma density. We have measured guided propagation at intensities up to 2×10^{17} W/cm^2, limited only by our current laser energy and waveguide leakage. We describe the creation and characterization of this structure in Chapter 3.

Chapter 2

Direct laser acceleration in plasma

2.1 Toy model

Using uncorrugated plasma waveguides [38] for direct electromagnetic accel-
eration was suggested by Serafim *et al.* [39], who proposed guiding a radially
polarized laser pulse to accelerate a copropagating relativistic electron bunch, as
shown in Figure 2.1. The laser's dominant radial component E_r guides as a hollow
mode with peak intensity at $r = w_{\mathrm{ch}}/\sqrt{2}$, where the mode radius w_{ch} is given by
$w_{\mathrm{ch}} = (1/\pi r_e \Delta N_e)^{1/2}$, r_e is the classical electron radius and ΔN_e is the electron den-
sity difference between $r = 0$ and $r = w_{\mathrm{ch}}$. The accelerating field is the associated
axial component E_z, which peaks at $r = 0$ and passes through zero at $r = w_{\mathrm{ch}}$. Fol-
lowing reference [39], the peak axial acceleration gradient from hollow beam guiding
in a plasma channel is given by

$$E[\mathrm{GV/cm}] = 98\lambda P^{1/2}/w_{\mathrm{ch}}^2 \tag{2.1}$$

where λ (the laser wavelength) and w_{ch} are in μm and P is the peak laser power
in TW. This accelerating field is proportional to the square root of laser intensity,
which scales with P/w_{ch}. The accelerating field is also proportional to $k_\perp/|k| \approx$
λ/w_{ch}, the effective 'ray angle' of the guided mode. Small guided mode diameters
are therefore especially important for high acceleration gradients.
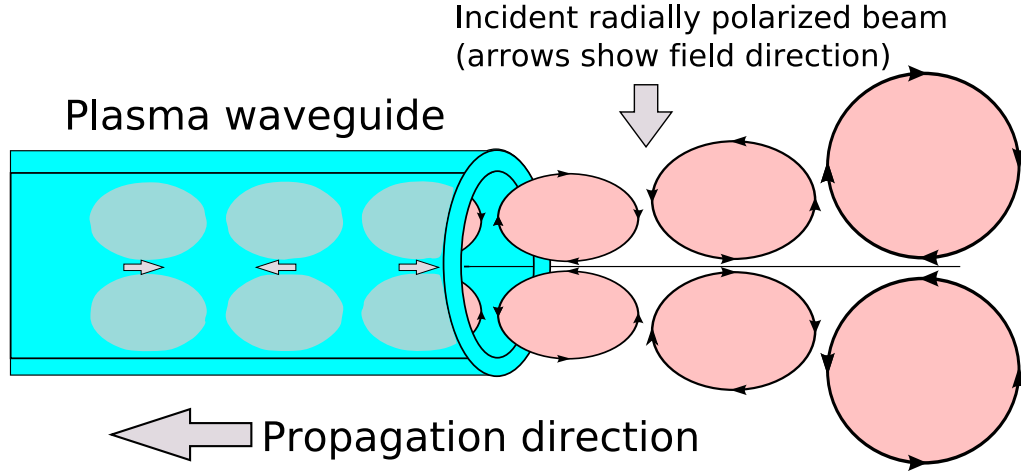
Figure 2.1: Radially polarized light entering a plasma waveguide to accelerate a copropagating bunch of relativistic electrons.

For a 1.9 TW laser pulse with $\lambda = 800$ nm in a channel supporting $w_{ch} = 15 \, \mu$m, E_z is an impressive 0.49 GV/cm. The plasma waveguide prevents the tightly focused pulse from diffracting rapidly away, extending this high energy density over many centimeters of propagation [40].

If there were no slippage between the laser phase velocity and the electron velocity (essentially c), this would compare very favorably to laser wakefield acceleration: Malka *et al.* used a 30 TW laser to produce an acceleration gradient of 0.66 GV/cm (200 MV over 3 mm) [28]. Wakefield acceleration (a nonlinear process) would not even work with a laser pulse power of only 1.9 TW. However, even a regenerative amplifier with ~ 1 mJ output (much smaller and cheaper than a terawatt laser) can easily produce 20 GW peak power, giving a 49 MV/cm gradient for direct acceleration.

Of course, a means must be found to slow the laser phase velocity to c or less to
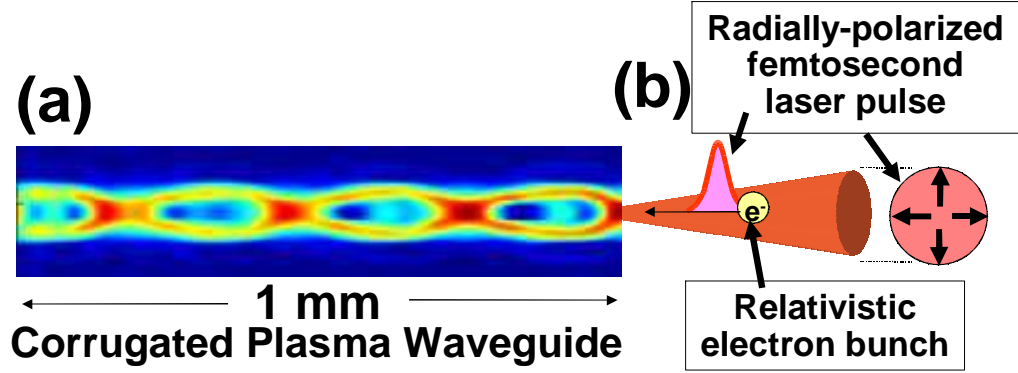
Figure 2.2: Radially polarized light entering a corrugated plasma waveguide to accelerate a copropagating bunch of relativistic electrons. Instead of phase matching the interaction with neutral gas as in Figure 2.1, the corrugations *quasi*-phase match the acceleration.

match the relativistic electron velocity. Neutral gas as proposed in [39] will not survive the laser intensities essential for high values of accelerating field E_z; even pulses well below the terawatt level will propagate in fully ionized waveguides. Without neutral gas, the laser phase velocity in an uncorrugated plasma waveguide is strictly superluminal [38]: a relativistic electron would slip 2π out of phase with the accelerating pulse after propagating a dephasing length $L_d = \lambda(N_0/N_{\text{cr}} + 2\lambda^2/\pi^2 w_{\text{ch}}^2)^{-1}$ [41], where N_0 is the on-axis plasma electron density of the channel and N_{cr} is the critical plasma electron density for wavelength λ [17]. Dephasing occurs because the guided mode phase velocity is not c. The term N_0/N_{cr} is due to plasma dispersion and would occur even in plane-wave geometry, and the term $2\lambda^2/\pi^2 w_{\text{ch}}^2$ is geometric dispersion due to waveguiding; both these effects increase the laser phase velocity above c. The electron receives no net acceleration: it would accelerate for a distance $L_d/2$, then decelerate an equal amount over the next $L_d/2$. Since L_d is typically a

16

One full dephasing cycle

$n_1 > n_2$

n1 n2 n1 n2 n1 n2 n1

Accelerating-phase region: low density for long interaction

Decelerating-phase region: high density for short interaction
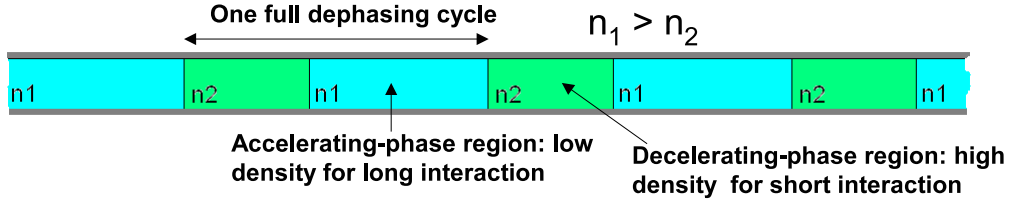
Figure 2.3: Toy model of electron density to estimate quasi-phase matched electron acceleration gradients in the corrugated plasma waveguide.

few tens or hundreds of microns, limiting the interaction length to $L_d/2$ gives very little acceleration [20].

Figure 2.2 shows how the corrugated plasma waveguide can *quasi*-phase match this interaction [42]. Laser phase velocity is locally faster in high plasma-density regions and slower in low plasma density. If L_d and the corrugation period are matched, the symmetry between acceleration and deceleration in a dephasing cycle is broken, and a properly phased electron will gain net energy; this process can be viewed as the inverse of transition radiation [43].

Figure 2.3 shows a toy model of the corrugated plasma waveguide that allows simple estimates of effective acceleration gradients with quasi-phase matching. The waveguide is assumed to consist of alternating segments which support the same guided mode radius w_{ch} but have either high or low on-axis electron density N_0. The length of each segment is chosen to equal the dephasing length L_d for that segment's radially polarized guided mode; the low density regions are therefore longer than the high density regions. Assuming a small density discontinuity at the interface between segments, we can neglect reflections at the boundaries, and a
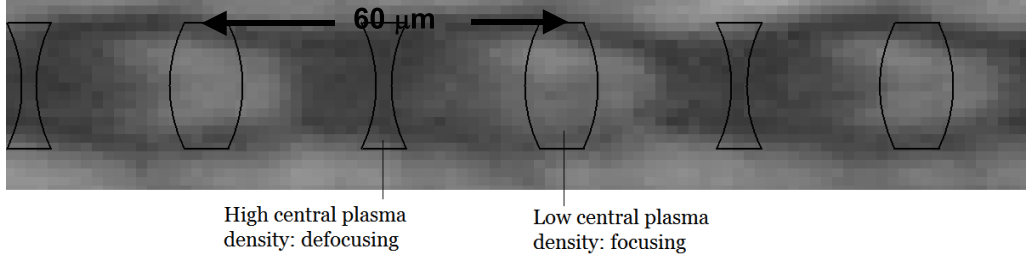
Figure 2.4: High magnification view of an experimental modulated waveguide. The waveguide has alternating peaks and troughs of central electron density, acting as focusing and defocusing microlenses. This geometry could potentially eliminate out-of-phase decelerating intensity on axis and further enhance in-phase acceleration intensity.

properly phased relativistic electron will gain energy

$$
\begin{aligned}
\Delta U &= \int_0^{L_{d1}} e E_{z1} \sin\left(\pi z / L_{d1}\right) dz - \int_0^{L_{d2}} e E_{z2} \sin\left(\pi z / L_{d2}\right) dz \qquad (2.2) \\
&= \frac{2}{\pi} e (E_{z1} L_{d1} - E_{z2} L_{d2})
\end{aligned}
$$

giving an effective accelerating gradient

$$
E_{z,\text{eff}} = \frac{2 E_z}{\pi} \frac{L_{d1} - L_{d2}}{L_{d1} + L_{d2}} \qquad (2.3)
$$

where the axial accelerating field E_z can be calculated from equation 2.1. Supposing $N_{0,1} = 3 \times 10^{18}$ cm^{-3} and $N_{0,2} = 6 \times 10^{18}$ cm^{-3} for a channel supporting $w_{\text{ch}} = 15~\mu m$, then $L_{d1} \approx 340~\mu m$ and $L_{d2} \approx 195~\mu m$, giving an effective accelerating field $E_{z,\text{eff}} \approx 0.17 E_{z,\text{max}}$. This promising result deserves further study with more sophisticated models.

A more realistic model would include the effects of diameter modulation, backscattering, changes in electron velocity, nonparabolic waveguide profiles, and plasma and optical nonlinearities. Note also that this simple model is far from opti-

18

mized. A waveguide with alternating focusing and defocusing segments (see Figure 2.4) could allow further enhancement of in-phase acceleration and greatly reduce or eliminate out-of-phase acceleration. Annular plasma waveguides have been also been demonstrated [44, 45] which guide annular modes with zero on-axis intensity. A corrugated waveguide consisting of alternating annular-mode and Gaussian-mode regions is another possible scheme for eliminating the decelerating regions and giving a higher effective gradient.

2.2 Finite difference time domain model: leakage, group velocity, dispersion

We obtain physical insight into the quasi-phase matching process from finite-difference time-domain (FDTD) simulations of linear pulse propagation in the simplified plasma density shown in Figure 2.5(a). This simulation was performed using MEEP, a freely available software package with subpixel smoothing for increased accuracy [46]. These simulations assume cylindrical symmetry, and include plasma dispersion, finite pulse duration, and pulse leakage out of the channel. Finite computing resources force us to use an unrealistically long wavelength of 6.4 μm, so the waveguide density was scaled to make the laser phase velocity comparable to experimental conditions.

We launch a radially polarized pulse into a corrugated plasma waveguide, and calculate the propagating electric and magnetic fields. Figure 2.5(b) shows the relative longitudinal and 2.5(c) the transverse electric field (scaled for visbility) felt
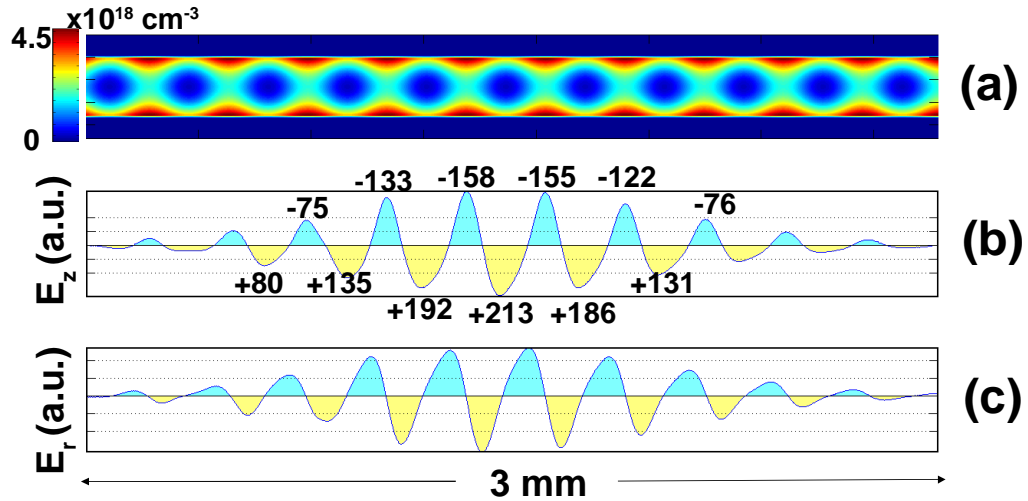
Figure 2.5: We approximate the plasma waveguide shown in Fig. 2.2 with **(a)** a simple electron density profile to model laser pulse propagation and electron acceleration. FDTD simulation results show **(b)** accelerating and **(c)** focusing forces felt by a properly phased relativistic ($v = c$) electron copropagating with a femtosecond laser pulse. Several acceleration (yellow, below axis) and deceleration (blue, above axis) half-dephasing cycles in **(b)** are labeled to show the work done on the electron in that region, with acceleration clearly dominating. The focusing force **(c)** is similarly quasi phase matched for this electron, to a lesser degree.

by a relativistic ($v_z = c$) electron copropagating with the laser pulse nearly on-axis. The transverse force depends strongly on the electron's transverse position; a truly on-axis electron would experience no transverse force due to the cylindrical symmetry of a radially-polarized beam. The channel's corrugation period is matched to L_d, and the initial phase between the electron and the laser field is chosen so that the electron is accelerated in the low-density section of each corrugation. Phase velocity is lower in these regions, so dephasing is slower and the electron spends more than half of each L_d in-phase with the accelerating field. If the initial phase were shifted by π, deceleration would occur instead of acceleration.

This simple picture is complicated somewhat by the modulation in waveguide diameter, which causes additional modulations in the guided pulse phase and intensity, but the electron clearly gains more energy during acceleration than it loses during deceleration. Each oscillation in 2.5(b) represents one dephasing cycle, and the number at each half-cycle is proportional to the energy gained or lost by the electron in that region. The transverse electric field shown in 2.5(c) is similarly quasi-phase matched, which contributes to a net radial focusing/defocusing force. The laser group velocity is subluminal; the electron starts behind the laser pulse and overtakes it. This 'pulse length dephasing' limits the interaction length. Leakage of the laser pulse out of the waveguide is minimal, and plasma dispersion does not interfere with acceleration.

Simulations with more extreme diameter modulation [47] show the importance of the detailed shape of the corrugation. The effects of diameter modulation can also quasi-phase match acceleration, and under some conditions this effect can even

oppose the acceleration due to modulation of N_0. Luckily, good experimental control of the corrugated waveguide has been demonstrated [34].

2.3 Analytic model, scaling law

Starting from these encouraging results, we introduce an analytic model in order to study more realistic parameters. This model neglects leakage and dispersion, which were found to be unimportant in FDTD simulations, and which will also be less pronounced for 0.8 μm light than it was at 6.4 μm. We start with the radial component of the laser vector potential:

$$A_r = \hat{A}_r(r, z, t) \exp\left[\mathrm{i}(k_0 z - \omega_0 t)\right] + \text{c.c.} \tag{2.4}$$

where k_0 and ω_0 are the central wave number and frequency of the laser pulse respectively and $\hat{A}_r(r, z, t)$ is a slowly varying envelope. We assume the pulse is azimuthally symmetric, and consider plasma channels with low electron densities such that the plasma frequency satisfies $\omega_p \ll \omega_0$, where $\omega_p^2 = 4\pi e^2 N_e(r, z)/m_e$, $-e$ is the electron charge, m_e the electron mass, and N_e is the electron density. In this regime the envelope $\hat{A}_r$ evolves on a time scale much longer than the laser period. The slowly varying envelope equation then determines the evolution of the laser pulse:

$$\left[2\mathrm{i}k_0\left(\frac{\partial}{\partial z} + \frac{1}{c}\frac{\partial}{\partial t}\right) + \frac{1}{r}\frac{\partial}{\partial r}r\frac{\partial}{\partial r} - \frac{1}{r^2}\right]\hat{A}_r = \frac{\omega_p^2(r, z)}{c^2}\hat{A}_r \tag{2.5}$$

where $\omega_0 = k_0 c$, and we have assumed that the electron plasma responds as a linear non-relativistic cold fluid. Because the laser-electron dephasing length L_d depends on the electron's velocity [41], acceleration of sub-relativistic electrons or

22

protons requires a structure with a graded modulation period to ensure L_d remains matched to the modulations over the entire interaction length. For mathematical simplicity we consider a fixed modulation period, suited to acceleration of electrons with $\gamma \gg 1$ for which the relativistic electron velocity depends only weakly on γ and L_d is nearly constant. We limit our analysis to a periodic electron density profile that models Figure 2.2(a), $N_e(r,z) = N_0(1 + \delta \sin(k_m z)) + N_0'' r^2/2$, where δ is the relative amplitude of the density modulation, N_0'' determines the radial dependence, and k_m is the wave number describing the axial periodicity of the channel. Exact solutions to Eq. (2.5) exist for this profile, which simplifies analysis of electron beam dynamics. Once A_r has been determined, A_z and the axial electric field can be determined by $\vec{\nabla} \cdot \vec{A} \approx 0$, which is consistent with the assumption $\omega_p \ll \omega_0$. The slowly varying envelope approximation neglects second derivatives in z and t in the wave equation which are responsible for subluminal group velocity, but the group velocity can be explicitly restored by replacing $c^{-1}\partial/\partial t$ with $v_g^{-1}\partial/\partial t$ in Eq. 2.5. Here $v_g = 1 - \omega_{p,0}^2/2\omega^2 - 4/(k_0 w_{\text{ch}})^2$, and we define $\omega_{p,0}^2 = \langle \omega_p^2(0,z)\rangle_z$, where the brackets represent an average over z. The lowest eigenmode solution of Eq. (2.5) is:

$$\hat{A}_r(r,z,t) = A_0 \frac{r}{w_{\text{ch}}} e^{-r^2/w_{\text{ch}}^2 - (z - v_g t)^2/\sigma_z^2} \sum_n \imath^n J_n(\psi) e^{-\imath\psi + \imath(\delta k + n k_m)z} \qquad (2.6)$$

where $J_n(\psi)$ is the nth order Bessel function of the first kind, $\psi = \delta\omega_{p,0}^2/2c^2 k_0 k_m$, and $\delta k = -k_0^{-1}(\omega_{p,0}^2/2c^2 + 4/w_{\text{ch}}^2)$. The pulse has a Gaussian temporal shape with duration σ_z/v_g.

In Eq. (2.6), we view the laser pulse as a sum of axial (z) spatial harmonics. Because our channel is axially periodic, each spatial harmonic moves with its own

23

constant phase velocity and amplitude. Matching the corrugation period to L_d is equivalent to matching the phase velocity of a spatial harmonic to the electron velocity. The harmonics have a relative amplitude given by $J_n(\psi)$ and the effective phase velocity $v_{p,n}$ for the nth spatial harmonic is $v_{p,n}/c = 1 - nk_m/k_0 + \omega_{p,0}^2/2\omega^2 + 4/(k_0 w_{\text{ch}})^2$. An appropriate choice of n and k_m gives a 'slow wave' spatial harmonic $(v_p < c)$ necessary for electron acceleration.

To determine a scaling law for direct electron acceleration, we consider an electron with initial conditions $(r, v_r) = (0, 0)$, and $(z, v_z) = (z_0, v_{z,0})$, where $v_{z,0}$ is assumed to be close enough to c such that the electron remains in the accelerating phase of the quasi-matched field over the process of acceleration. For our experimental conditions of $(\omega_{p,0}/\omega_0)^2(k_0/k_m) \ll 1$ [38], $\psi \ll 1$, and $J_n(\psi) \sim \psi^n/2^n n!$. The amplitude of the spatial harmonics decreases quickly with harmonic number, so we focus on the $n = 1$ spatial harmonic, and set $v_{p,1} = v_{z,0}$. Choosing z_0 to optimize acceleration and integrating the axial electric field over the pulse length dephasing time $\sigma_z/(v_g - v_{z,0})$ using $v_{z,0} \approx c$, we obtain for the energy gain

$$\left.\frac{\Delta E}{m_e c^2}\right|_{\text{DA}} \sim 4\delta a_0 \left(\frac{\sigma_z}{w_{\text{ch}}}\right) \left(\frac{\lambda_p}{\lambda}\right)^2 \left(1 + \frac{2\lambda_p^2}{\pi^2 w_{\text{ch}}^2}\right)^{-2} \tag{2.7}$$

where $\lambda_p = 2\pi c/\omega_{p,0}$ is the plasma wavelength. The pulse length dephasing time limits the interaction length. By comparison, the dephasing-limited energy gain for resonant laser-wakefield acceleration is [48]:

$$\left.\frac{\Delta E}{m_e c^2}\right|_{\text{WF}} \sim \frac{a_0^2}{(1 + a_0^2/2)^{1/2}} \left(\frac{\lambda_p}{\lambda}\right)^2 \left(1 + \frac{\lambda_p^2}{\pi^2 w_{\text{ch}}^2}\right)^{-1} \tag{2.8}$$

For a wavelength $\lambda = 800$nm, matched beam radius $w_{\text{ch}} = 15\mu$m, normalized amplitude $a_0 = 0.25$ corresponding to a laser power of 1.9TW, pulse length $\sigma_z/c = 300$fs,

on axis plasma density $N_0 = 7 \times 10^{18} \text{cm}^{-3}$, corrugation amplitude $\delta = 0.9$, and modulation period of $T_m = 349 \mu$m (we use these parameters in our following calculations), we have $\Delta E / mc^2|_{\text{DA}} \sim 1000$. In [48], a 7.16TW, 100fs pulse in a suitable plasma channel gives $\Delta E / mc^2|_{\text{WF}} \sim 750$, a slightly reduced acceleration with similar pulse energy. However, it is with smaller lasers that direct acceleration (a linear process) has its strongest advantage: replacing 1.9TW with 30GW would still give $\Delta E / mc^2|_{\text{DA}} \sim 125$, whereas (extremely nonlinear) wakefield acceleration is inoperable with such small lasers.

Equation 2.7 shows how important an optimized waveguide is for high acceleration gradients. Acceleration is proportional to δ, so waveguides with sharp density structure like those shown in Fig. 5 of [49] may be ideal. Waveguide diameter is even more important; for fixed laser power, a smaller waveguide diameter w_{ch} will give both a larger a_0, and a larger ratio of $E_{z,\text{peak}}$ to $E_{r,\text{peak}}$, so accelerating gradient scales roughly like w_{ch}^{-2}. Luckily, optically generated cluster-target waveguides can be precisely controlled, as shown in Figures 2-5 of [49].

2.4   Transverse dynamics

To study electron beam dynamics, we integrate the relativistic electron equations of motion in the laser electromagnetic field determined by Eqs. (2.4) and (2.6). We neglect space-charge effects, which become important when the axial electric field due to the bunched beam current becomes comparable to the quasi-phase matched accelerating field. We estimate this gives an upper limit on the beam current of

$I_{\max}[A] < 1.7 \times 10^4 a_0 J_1(\psi) w_{\mathrm{ch}}/\lambda$, which for our parameters is 3×10^4 A, or 40 pC per microbunch.

Figures 2.6(a) and (b) show maximum particle energy gain versus time, for a pulse of duration $\sigma_z/c = 300$ fs. The pulse length dephasing time for this simulation is 130 ps. In Figure 2.6(a), the effective phase velocity of the $n = 1$ spatial harmonic is matched to three different initial electron velocities by tuning the modulation period, which could be accomplished experimentally by inserting imaging optics in the channel formation beam used to create the corrugated plasma waveguide. In Figure 2.6(b),the phase velocity of the $n = 1$ spatial harmonic was set to c for all three initial electron energies. The red lines labeled 'scaling' give the maximum energy gain based on the amplitude of the $n = 1$ component of the axial electric field. In all cases, the phase velocity of the $n = 1$ spatial harmonic is constant, but the electron velocity changes, so phase matching is imperfect, eventually resulting in oscillating energy gain, most noticably for $\gamma_0 = 30$. Clearly it can be better to have electrons 'catch up' to a slightly faster wave than for them to be initially resonant with but eventually overtake a slower one. As mentioned earlier a graded corrugation period would give better phase matching and eliminate this oscillation in energy gain.

An electron displaced from the axis will experience two types of transverse force. The first type is a quasi-phase matched focusing or defocusing due to the radial component of the slow wave spatial harmonic. For an electron near the peak
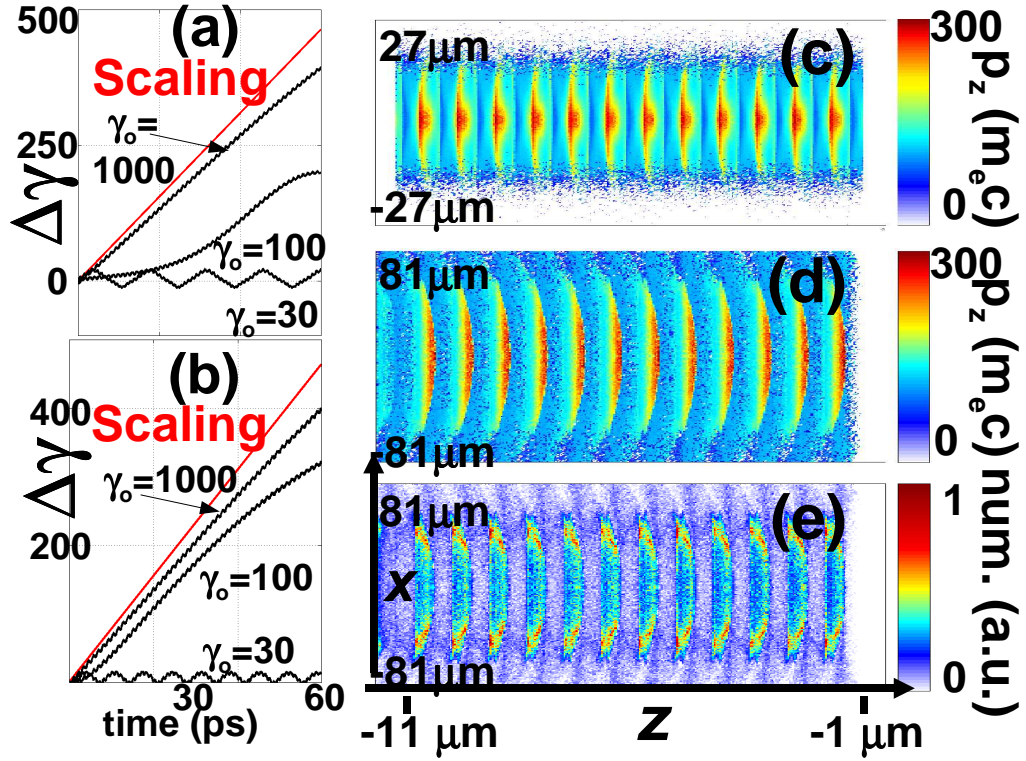
Figure 2.6: **(a)** Energy gain $\Delta\gamma$ vs. time with the slow wave phase velocity matched to the initial electron velocity and **(b)** the slow wave velocity is set to c, for $\gamma_0 = 30$, 100, and 1000. Allowing the electrons to catch up to the slow wave velocity reduces the dephasing due to acceleration at higher energies. **(c)** Average final z momentum (color scale) as a function of initial position (z_0, x_0). **(d)** Average final z momentum (color scale) as a function of final position (z_f, x_f) relative to the leading electron. **(e)** Final electron density as a function of final position (z_f, x_f). The electron beam has become bunched and focused.

of the pulse and slightly off axis ($r \ll w_{\text{ch}}$), this force is

$$F_r^{\text{sw}} = \frac{m_e c^2 k_0 \delta a_0}{1 + 2\lambda_p^2/(\pi^2 w_{\text{ch}}^2)} \frac{r}{w_{\text{ch}}} \left[1 - \frac{v_z}{c} \left(1 + \frac{8}{k_0^2 w_{\text{ch}}^2} \right) \right] \cos\left(k_0 z - \omega t \right) \tag{2.9}$$

For electrons distributed uniformly over several wavelengths in z, an equal number will experience focusing as experience defocusing from the quasi-phase matched fields. The quasi-phase matched radial force is 90° out of phase with the corresponding axial force, so the focusing and defocusing force vanishes for particles in the maximum accelerating phase. The second force is the ponderomotive force on the electrons from the $n = 0$ fundamental laser mode:

$$F_r^{\text{pm}} = -\frac{2mc^2}{\gamma_0} \frac{r}{w_{\text{ch}}^2} |a_0|^2 \left[1 - \frac{4}{\pi^2} \frac{v_z}{c} \left(\frac{\lambda_p}{w_{\text{ch}}} \right)^2 \left(1 + \frac{\lambda_p^2}{\pi^2 w_{\text{ch}}^2} \right)^{-1} \right]^2 \tag{2.10}$$

which is obtained by linearizing the equations of motion about $v_z = v_{z,0}$ and averaging over the fast time scale $(k_m v_z)^{-1}$. Because the mode fields peak off axis, this force focuses regardless of initial electron phase. Generally the peak quasi-phase matched force exceeds the ponderomotive force, except in the maximum accelerating phase for which the radial quasi-phase matched force vanishes.

The use of a radially-polarized laser pulse rather than simple linear polarization, as shown in Figure 2.2(b), is crucial for accelerating high-quality electron beams. At the center of a cylindrically-symmetric radially polarized beam, the accelerating force is maximized and transverse forces vanish. A cylindrically-symmetric electron beam fits nicely in this high-gradient region, and electrons that make small excursions from the center of the beam can feel a time-averaged restoring force back to the beam center [35]. An electron beam injected into the center of a linearly

polarized waveguide mode, however, would experience transverse forces that dwarf the longitudinal acceleration and be quickly expelled from the waveguide.

2.5   Test particles

To examine transverse dynamics we distribute electrons uniformly in z from 1 μm to 11 μm behind the pulse maximum and with a Gaussian distribution in r with width σ_r. The pulse length is 300 fs. Figures 2.6(c) and 2.6(d) show the number-averaged final z momentum as a function of initial and final position respectively for an initial electron beam radius of 9 μm. Efficiency is very injector-dependent: to be accelerated, electrons must start in 'buckets' one half of a slow wavelength long and less than one laser spot size wide; for our parameters, the space charge limit per bucket is < 40 pC. Figure 2.6(e) shows the final electron beam density as a function of position; the beam has acquired a significant transverse spread which peaks off axis. Comparing Figures 2.6(d) and 2.6(e) we see that these peaks are mostly composed of lower energy electrons that have been expelled from the center of the buckets. These effects can be clearly seen in the linked multimedia file [50], which shows the time evolution of a subset of the particles from Figure 2.6(c)-(d) in a window moving to the right at $\gamma = 100$. The particle bunch is longer than one accelerating 'bucket'; some electrons are decelerated and some are defocused. Electrons that don't accelerate slip into a defocusing region and are ejected from the waveguide. The highest-energy electrons simply plow ahead while absorbing energy, largely unaffected by transverse forces, and gain 151 MeV over 1.8 cm, a gradient

of 84 MeV/cm. A 40 pC 'bucket' would absorb about 6 mJ of energy, $\sim 1\%$ of the driving pulse, while the number of loaded buckets depends on the injector. Since this acceleration process is linear and scales with the square root of laser power, a laser power of only 30 GW would give a respectable gradient of 10.6 MeV/cm.

The fact that low-energy electrons are expelled from the waveguide suggests an interesting method to obtain high-quality monoenergetic electron beams from low-quality injected electrons. Study of Figure 2.6(d) and (e) reveals that spatially filtering electrons at a radius greater than ~ 40 μm would greatly decrease the number of low-energy electrons while leaving the high-energy electrons relatively unscathed. A carefully aligned pinhole following the waveguide thus might allow filtration of a low-quality injected beam. The injected beam will still heavily influence the quality of the accelerated electron beam, but the single-particle results shown in Figure 2.6 allow simple estimation of how an injected beam will map to a final, accelerated beam for any given injector.

2.6   Remaining challenges: radial polarization, electron injection

With the demonstration of the corrugated plasma waveguide [34, 49], two challenges remain: the generation of femtosecond, millijoule pulses of radially polarized light, and the creation of a short, tightly-focused electron bunch suitable for injection into our micron-scale structure.

Efficient conversion of linearly polarized laser beams to radial polarization has been demonstrated for continuous-wave beams [51], and we are working to extend

these results to femtosecond pulses.

For proof-of-principle experiments, we plan to use our lab's new 30 TW laser to generate relativistic seed electrons through wakefield acceleration, but a simple, inexpensive electron injection technique is crucial to the success of electron acceleration with sub-terawatt lasers.

Non-periodic corrugations can phase match the acceleration of non-relativistic electrons or protons, but the minimum corrugation length gives a minimum electron injection speed. An injector based on either radio-frequency acceleration [52], or millijoule-level illumination of solid targets [53] could potentially produce an initial high-quality electron bunch fast enough to be injected without too much added expense.

Chapter 3

The corrugated plasma waveguide

3.1 Generation

Figure 3.1 shows our experimental setup for creating corrugated plasma waveguides. Our lab is already experienced at generating unmodulated waveguides in cluster jets [54] using conical-wavefront (Bessel beam) pulses produced by an axicon-focused collimated beam from a 10 Hz, 1064 nm, 100 ps Nd:YAG laser with pulse energy of 200-500 mJ. The axicon, a conical lens, produces a long (~ 2.5 cm), thin ($< 3\ \mu$m) focal region with high enough intensity to first ionize the clusters and then collisionally heat the resulting plasma. As described in [54], the center of this plasma is hotter than the edges and expands more rapidly, producing a 'hollow' tube of plasma with a density minimum on axis.

The cluster source in these experiments was a cryogenically cooled supersonic gas jet with a 1.5 cm long by 1 mm wide nozzle exit orifice [34]. The 2.5 cm line-focus length of the Bessel beam overlapped the 1.5 cm length of the cluster jet, resulting in 1.5 cm long plasma channels. Waveguides were injected through a hole in the axicon (Fig. 3.1(a)) with a 70 mJ, 70 fs, 800 nm Ti:Sapphire laser pulse synchronized [55] and delayed with respect to the channel-generating Nd:YAG pulse. A small portion of this pulse (~ 1 mJ) was split off into a delay line, directed transversely through the waveguide, and then imaged through a femtosecond folded
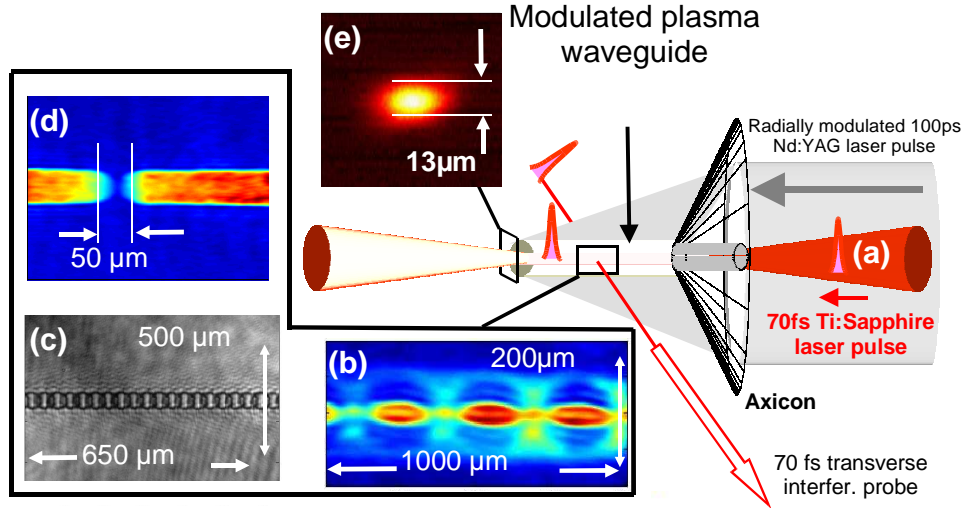
Figure 3.1: Experimental geometry: radially modulated Nd:YAG laser pulse $(200 - 500$ mJ, 100 ps, 1064 nm) from ring grating imaging system (not shown) focused by an axicon onto a liquid nitrogen-cooled elongated cluster jet target, generating a 1.5 cm long corrugated plasma channel. **(a)** Ti:Sapphire laser pulse guided down the channel at an adjustable delay with respect to the Nd:YAG pulse. A 1 mJ portion of the 70 fs, 800 nm pulse was directed transversely through the corrugated guide and into a folded wavefront Michelson interferometer for time-resolved interferometric/shadowgraphic images. Phase images of channels with **(b)** 300 μm modulation period in argon clusters, **(c)** a 35 μm period in air, and **(d)** a single, deep corrugation in nitrogen clusters. **(e)** Lowest order exit mode from the guide of Fig. 3.4(b)(1ii), with $w_{\mathrm{hwhm}} = 13$ μm.

wavefront Michelson interferometer onto a CCD camera. Electron density profile images of the evolving corrugated waveguide were obtained by phase extraction of the time-resolved interferograms, followed by Abel inversion.

In order to axially modulate the plasma channel, we placed a transmissive 'ring grating' (RG) and an imaging telescope between the Nd:YAG laser and the axicon. The RGs used in these experiments were lithographically etched fused silica discs with variable groove period, groove structure, and duty cycle. The ring grating

shown in Figure 3.2(b), used to generate the waveguide shown in Fig. 3.1(c), is a set of concentric rings regularly spaced with a radial period of 10 μm, a groove depth of 1 μm, and a duty cycle of $\sim 70\%$ The telescope images the RG diffraction pattern through the axicon and onto the optical axis, leading to axial intensity modulations of the Bessel beam. The axial modulation of the central spot intensity imposes axial modulations in the heating and plasma generation in the cluster jet. For the present work, we used a periodic modulation, but arbitrary RG patterns are possible. Phase matching direct laser acceleration of ions or nonrelativistic electrons, for example, would require a graded modulation period.

The 100 ps heater pulse is very short compared to the hydrodynamic evolution timescale ($\sim 0.1 - 0.5$ ns) of the heated bulk plasma (formed from merged cluster explosions) that remains after the pulse [54]. This plasma undergoes axially periodic radial hydrodynamic shock expansion, producing a corrugated plasma waveguide. Two examples of phase images of the magnified central waveguide region are shown in Fig. 3.1, with 300 μm RG-generated modulations in argon clusters (b) and a 25 μm wire-generated corrugation in nitrogen clusters (d). Corrugated guides can also be generated in static gases: Fig. 3.1(c) shows a shadowgram of a modulated channel produced in air with a period of 35 μm. A typical guided exit mode from a modulated cluster plasma channel (half-width-at half-maximum mean radius 13 μm) is shown in Fig 3.1(e). Note that the cluster-generated channels are stable and reproducible: the shot-to-shot extracted density variation is less than 5%.

Ring gratings were designed using ICED editor [56]. Microtronics Inc. [57] fabricated chrome-on-sodalime masks from these designs with ~ 1 μm resolution.
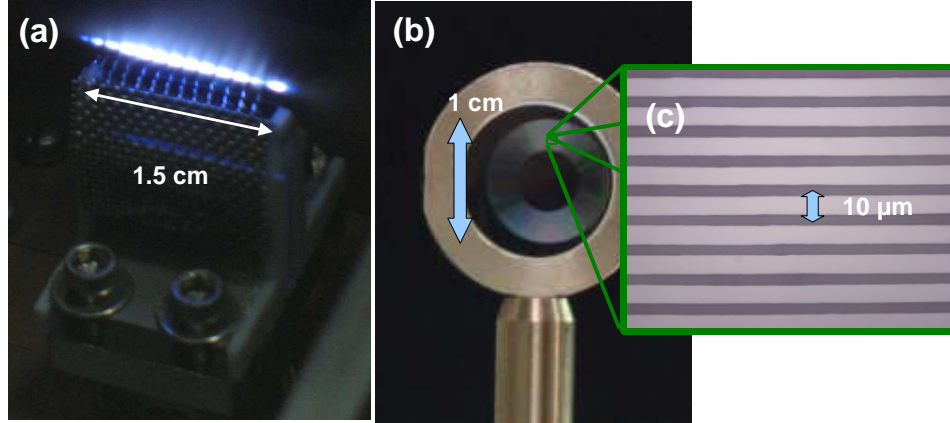
Figure 3.2: Different corrugation methods: **(a)** Wire mesh obstructing cluster jet flow, producing a waveguide with ~ 1 mm corrugation period and near 100% density modulation. **(b)** Transmissive 'ring grating' used to produce the waveguide shown in Fig. 3.1(c). This corrugation method modulates ionization and heating rather than material density. High-magnification image of the ring grating **(c)** shows the ~ 10 μm groove period required to produce periodic ~ 35 μm corrugations.

At the University of Maryland LPS facility [58], contact lithography transferred the mask patterns to photoresist on 1" fused silica discs, which were then exposed to reactive ion etching. The grooves on the RG were etched ~ 1 μm deep, chosen so that each groove would give approximately a π phase shift to the 1064 nm Nd:YAG pulse.

Depending on the groove period of a ring grating, diffractive or ray optics may be more appropriate to describe the effect of the grooves on the channel creation beam. The 10 μm groove period in Figure 3.2(c), for example, produce only a few diffracted orders that are clearly distinguishable after a few centimeters of propagation; imaging optics are neccesary to relay the image of the RG to the axicon focal region. These individual diffracted orders are similar to the Bessel beam produced

by an axicon, with conical wavefronts converging or diverging from the axis. Converging diffracted orders produce a line focus, just like an axicon, and care must be taken not to damage intermediate imaging optics.

Depending on the numerical aperture of the imaging optics, different diffractive orders may be truncated, resulting in distortion of the image. In the case where only a single diffracted order is selected (in addition to the undiffracted beam), the axicon focal region looks like the interference of two Bessel beams, producing a periodic axial intensity modulation. It is essential that the RG be co-axial with the axicon; axial mismatch by more than a groove period between these optics destroys the overlap of their focal regions giving poor corrugations.

For longer-period corrugations such as those shown in Figure 3.1(b), diffractive effects from the RG are less noticable, appearing as a blurring of the edges of each groove. Imaging optics suppress this blurring, but only one axial position on the waveguide is perfectly imaged, resulting in possible nonuniformity of the corrugations even for a uniformly grooved RG. For longer period RG's, an additional fast azimuthal variation was added to each radial groove, producing diffracted light at too high an angle for our imaging system to capture. This effect made each groove effectively opaque, allowing for deep corrugations without using truly opaque grooves which would be rapidly destroyed by the high-energy Nd:YAG beam.

Alternatively, the plasma channel can be corrugated by obstructing the flow of clusters from the gas jet. Figure 3.1(d) shows the effect of placing a single 25 μm diameter tungsten wire directly between the jet nozzle and the focus of the Bessel beam. The resulting corrugation is extremely sharp. Unlike the waveguides

shown in Fig. 3.4(b), guiding an intense femtosecond pulse in this channel reveals no measureable scattering or ionization in this gap.

These two methods of corrugation offer complementary strengths. RG-generated corrugations are computer-designed, easy to align and extremely precise and regular, but cannot be 'tuned' much without switching ring gratings. Wire-generated corrugations, on the other hand, can be easily adjustable in the lab. RG-generated corrugations modulate heating and ionization, so they tend to produce channels with strong modulation in diameter (Fig. 3.1(b)), whereas wire-generated corrugations strongly modulate density without affecting waveguide diameter much at all (Fig. 3.1(d)). Our simulations of laser acceleration in these channels have focused on density modulations for mathematical simplicity, but diameter modulation could have important effects on acceleration gradients.

Figure 3.3 shows results for a corrugated hydrogen plasma waveguide. Hydrogen plasma waveguides are important for laser-plasma acceleration [24, 27, 28] because they are easily fully ionized during their formation, making impossible further ionization by guided intense pulses, which can lead to distortion and ionization-induced refractive defocusing. Figure 3.3(a) shows the electron density $N_e(r, z)$ of a 3 mm section near the entrance of a 1.5 cm hydrogen waveguide, 1 ns after generation. The density profiles of the injected and uninjected waveguides are very similar, showing that the guide was relatively unchanged by the intense guided pulse, implying that the hydrogen target was fully ionized by the channel creation pulse. With modulated hydrogen guides, energy throughput is $\sim 10\%$, yielding output intensity of 10^{17} W/cm^2. The low throughput is due to low coupling efficiency, leakage and
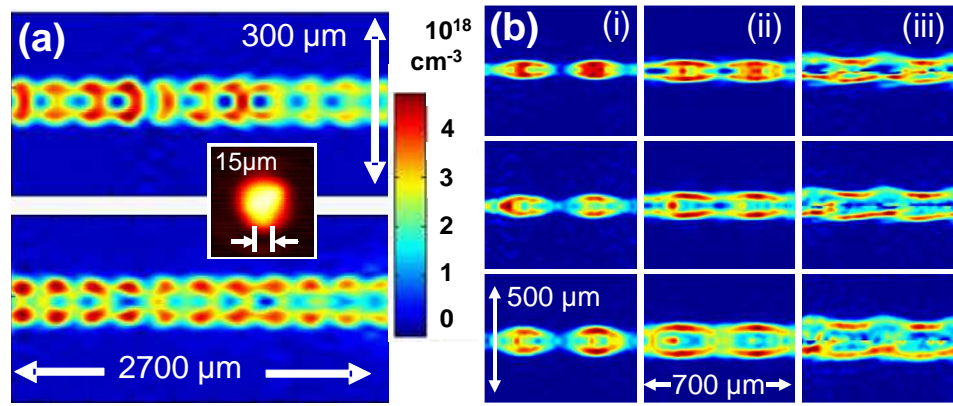
Figure 3.3: Corrugated channels produced in a hydrogen cluster jet at 800 psi and $-145°$ C backing pressure and temperature. (a) ~ 3 mm section of channel without (top panel) and with (bottom panel) injection at 1 ns delay of a 70 mJ, 70 fs, 800 nm laser pulse, viewed 100 ps after pulse passage. The channel exit mode of $w_{hwhm} = 15$ μm is shown in the inset. (b) Higher magnification Abel-inverted electron density profiles of 2 corrugation periods for channel creation pulse energies of (i) 200 mJ, (ii) 300 mJ, and (iii) 500 mJ (with RG/axicon misalignment) at interferometer probe delays of, top to bottom, 0.5 ns, 1 ns, and 2 ns.

side scattering out of the guide due to the modulations; this leakage is directly seen in argon results. We made no effort to optimize coupling efficiency or leakage, so throughput could likely be improved.

Figure 3.3(b) shows higher magnification profiles of two modulation periods as a function of interferometer probe pulse delay (0.5, 1, and 2 ns), for channel creation pulse energies of (i) 200 mJ and (ii) 300 mJ. It is seen that lower pulse energy ((i)) can produce 'beads' of plasma, separated by zones of neutral clusters and atoms, while higher energy ((ii)) results in a more continuous channel. The plasma beads act as tiny lenses, collecting the light emerging from a neutral gap and focusing the beam into the next gap. Figure 3.3(b)(iii) shows the result of misalignment (at 500 mJ) of the axicon axis and the RG optical axis: a continuous plasma fibre is generated, but is no longer cylindrically symmetric.

Channels with higher ionization Z were generated in argon cluster jets. Figure 3.4(a) shows an extended region of channel at 1.5 ns delay with and without guided pulse injection (bottom and top panels respectively) for a probe delay ~ 10 ps after guided pulse passage. The channel itself isn't affected much by the guided pulse, but in contrast to the hydrogen results, there is a significant electron density 'halo' located at a radial distance ~ 100 μm from the channel. Scanning the delay of the transverse imaging pulse (not shown) shows that the halo propagates right-to-left at the speed of light with the guided pulse. The halo radial position remains constant over the full 1.5 cm length of the corrugated channel but decays in density, suggesting that it originates from additional cluster ionization from channel side leakage [38] rather than from uncoupled entrance light skimming the outside of the
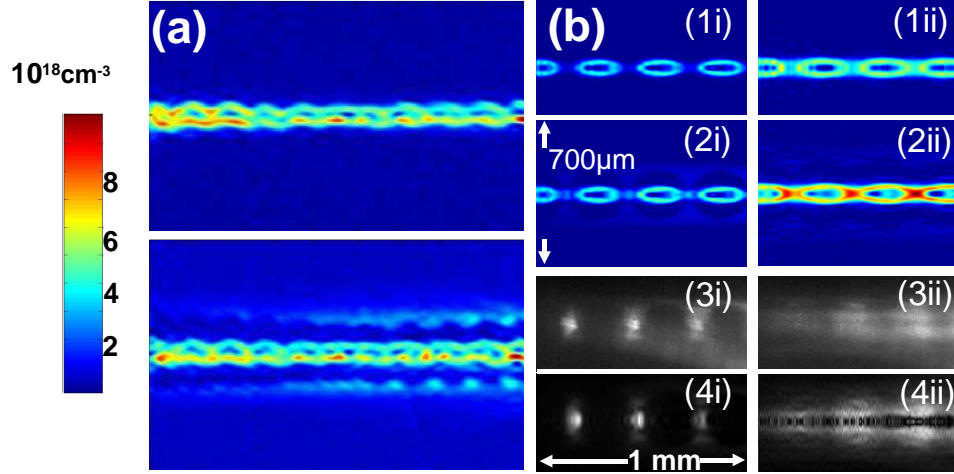
Figure 3.4: Corrugated channels in an argon cluster jet at 800 psi backing pressure and room temperature. Laser 70 mJ, 70 fs, 800 nm. **(a)** 3 mm section of channel without (top panel) and with (bottom panel) injection at 1.5 ns delay. **(b)** Magnified images at 2 ns delay of beaded (300 mJ pump, left column) and more continuous (500 mJ pump, right column) channel modulations. Left and right columns: (1): density profile of uninjected guide, (2): density profile of injected guide, (3): Guided scattering image at 800 nm corresponding to (2), (4): Abel-inversion of (3).

channel. The leakage light moves radially across a zone of low density plasma and neutrals until it reaches the layer of argon clusters that was undisturbed during channel formation. Hydrogen clusters are smaller and more fragile, so it is unlikely they survive so close to the channel after its formation, so don't see a halo in Fig. 3.3.

Higher resolution images of three periods of modulation near the argon channel centre are shown in Fig. 3.4(b), for cases of beaded (300 mJ pump, left column) and continuous (500 mJ pump, right column) modulations, without guided pulse injection (panels (1)) and with injection (panels (2)-(4)). In the case of the beaded guide, Fig. 3.4(b)(2i) shows strong additional ionization by the guided pulse in the

neutral gaps as the beam is focused by each plasma microlens and collected by the next. Remarkably, the channel energy throughput (including losses from incoupling) is still 10%, showing that the tiny plasma microlenses capture and refocus much of the guided pulse over the full 1.5 cm length of the channel. Throughput for the continuous modulation case is 20%, yielding 2×10^{17} W/cm^2 peak intensity at a beam waist, estimating the beam waist by the observation that the beam exits the channel at a guide bulge. By comparison, throughput for this injection delay in unmodulated waveguides is 60%.

Panels (2) both show the ionization halo induced by side-leakage of the guided pulse in more detail. Side-imaged Thomson/Rayleigh scattering of guided 800 nm light shows scattering strongly localized in the neutral gaps in the beaded guide (Fig. 3.4(b)(3i)), and more smoothly modulated from leakage at the beam waists in the more continuous guide (Fig. 3.4(b)(3ii)). Panels (4i) and (4ii), which show the scattering source (r, z) profiles, are Abel inversions of panels (3i) and (3ii). These images make clear that the dominant scatterers are likely clusters, either those surviving in the gaps between beads, or those external to the continuously modulated guide.

Detailed images of wire-generated corrugations are shown in Figure 3.5. A 25 μm-diameter tungsten wire placed just above the gas jet nozzle produces a sharp density notch in the cluster target. The phase images shown in Fig. 3.5 show that this 50 μm density notch is persistent in (b) liquid nitrogen-cooled nitrogen clusters and (c) room-temperature argon clusters as the waveguide expands over more than 2 ns. Figure 3.5(a) is the Abel-inverted electron density of the 1 ns-delay phase
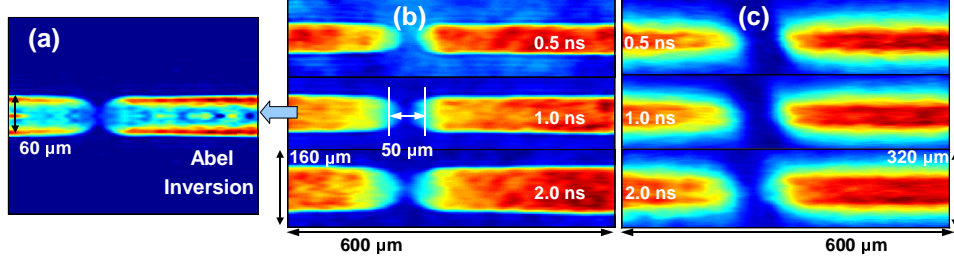
Figure 3.5: Abel-inverted electron density **(a)** of a wire-generated corru-gation in nitrogen clusters 1 ns after creation shows nearly 100% density modulation. Phase images of these corrugations at 0.5, 1.0, and 2.0 ns delay in **(b)** nitrogen and **(c)** argon clusters show that this sharp density structure persists for the entire useful life of the waveguide.

image from Fig. 3.5(b). The electron density peaks at approximately 9×10^{18} cm^{-3} at the channel wall, and falls to below the noise floor of our measurement in the middle of the 50 μm corrugation. The 60 μm waveguide diameter, however, is nearly unchanged, in contrast to RG-generated corrugations.

Guiding a 70 mJ, 70 fs, 800 nm laser pulse in these structures shows no further scattering from this gap, indicating the absence of clustered or unclustered gas rather than a simple ionization modulation. Future experiments will explore extended wire-modulated guides and attempt to reduce leakage of the guided pulse. However, we note that even with the $\sim 80\%$ leakage shown here, the guided laser *field* at the channel exit is reduced by only $\sim 50\%$ from that at the entrance.

3.2 Plasma density measurement: phase extraction, Abel inversion

Shadowgraphs, as shown in Figure 3.1(c), are useful for visualizing corrugated waveguides, but do not give quantitative measurement of plasma density. Transverse

interferometry gives information about plasma density, but produces a less intuitive image that must be processed to extract the phase shifts [59] used to calculate plasma density. The corrugated plasma waveguide has many 'knobs' which can be adjusted to control its creation (Nd:YAG pulse energy, optical alignment, gas jet pressure and temperature, etc), and plasma density measurements are useful to help optimize these parameters. In order to reduce the time lag between taking data, processing it, and adjusting control parameters, we incorporated the phase extraction algorithm directly in our data-taking software to display measured plasma density in real time.

LabView [60] is a convenient interface to our CCD cameras because of its wide selection of hardware drivers. The phase extraction algorithm [59] is awkward to code in LabView's graphical programming language, and we found it to be too slow for satisfactory frame rates (> 5 seconds per processed frame). The same algorithm implemented in MATLAB is much faster (several frames/second), but was not easily interfaced with our CCD cameras, so we compiled a MATLAB DLL to implement the phase extraction algorithm and called it from within LabView to combine speed with convenience. At the time, this was nontrivial and poorly documented, but provided an elegant solution to our optimization problem. More recent versions of LabView have since improved the speed and convenience of matrix manipulation however, making this solution somewhat obsolete.

One important step of the phase extraction algorithm is choosing a Fourier window to isolate the spatial frequencies of the interferogram which contain plasma density information. This choice is somewhat subjective, and can introduce artifacts into the measured plasma density if chosen poorly. Displaying extracted phase in

real time had the unexpected advantage that it becomes easy to tune this Fourier window to minimize artifacts.

Another troublesome step of the phase extraction algorithm is phase unwrapping; phase jumps of 2π do not represent discontinuities in plasma density, just artifacts in the measurement which must be removed. The phase unwrapping algorithm included in MATLAB is fast but naive, simply moving along each column and each row adjusting neighboring pixels by 2π to remove these discontinuities. Noise which disrupts the measured phase at any single pixel by $\sim\pi$ can cause errors which propagate through the rest of the image, requiring annoying fixes 'by hand' to recover the data. To minimize these problems, we instead used the phase unwrapping method described in [61], which is more computationally expensive but more robust. Errors in this phase unwrapping algorithm due to noise produce local disturbances, but do not disrupt the entire image.

Initially, Abel inversion was another bottleneck in our data processing. Converting a measured interferogram to radial density profiles like those shown in Figures 3.3, 3.4, and 3.5 involves computating a numerical integral of each vertical column of the measured data, for each *pixel* of the processed data [62]:

$$f(r, z) = -\frac{1}{\pi} \int_r^R \frac{dS(y, z)}{dy} \left(y^2 - r^2\right)^{-1/2} dy \tag{3.1}$$

where $S(y, z)$ is our measured plasma density integrated along the x-direction (transverse to the plasma waveguide), and $f(r, z)$ is the plasma density in cylindrical coordinates. Even on a reasonably fast computer, processing a single image took

44
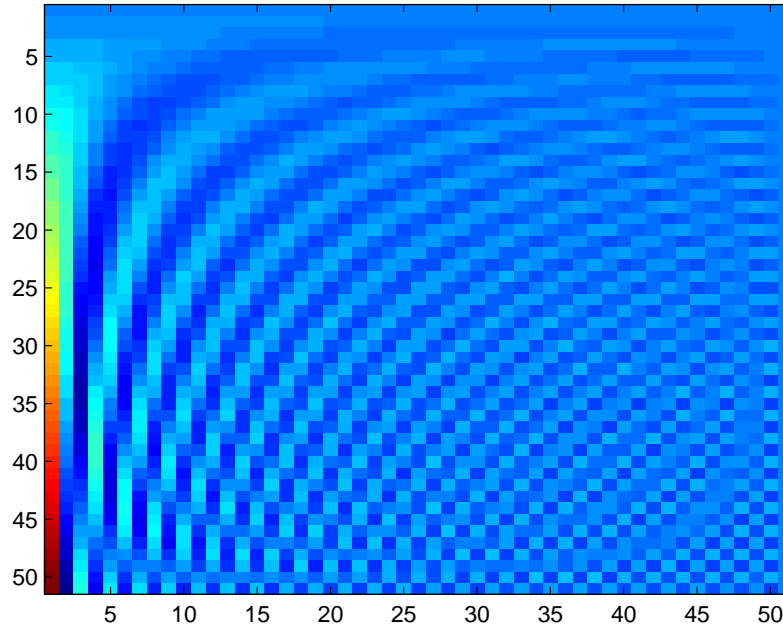
Figure 3.6: Abel transform of the 50-point FFT basis. Each row is the Abel inverse of the corresponding basis function used in the fast Fourier transform.

upwards of ten minutes using straightforward numerical integration. However, the algorithm of Kalal and Nugent [62] speeds up this process immensely.

Since Abel inversion is a linear process, you can compute the Abel inversion of each function in a complete set of basis functions. Then, to perform Abel inversion of an arbitrary $S(y)$, you represent $S(y)$ as a sum of these basis functions. Since you have stored the Abel inversion of each of these basis functions, you can simply sum up the transformed basis functions with appropriate weights to give $f(r)$.

Figure 3.6 shows the Abel inversions of each basis function in the 50-point FFT basis. An FFT of a 50-pixel signal decomposes that signal into a sum of 50 Fourier

basis functions of the form $\exp(\mathrm{i}kx)$; each horizontal row of Figure 3.6 is the Abel inversion of the corresponding FFT basis function. An arbitrary $S(y)$ represented with 50 pixels or less can be padded with zeros to a length of 50 pixels, and then the FFT of this signal gives the weight of each Fourier basis function in the signal. Each row of Figure 3.6 is weighted by this factor, and then the rows are added together to give a single 50-pixel row which is $f(r)$, the Abel inverse of $S(y)$.

Notice that the far left column of Figure 3.6 is much more intense than the rest of the figure, especially for the lower (high spatial frequency) rows. This is because measurement of $S(y)$ gives very little information about $f(r = 0)$. Only one pixel of $S(y)$ contains any information about $f(r = 0)$, and that column represents a ray of light that traveled through the full width of the plasma to get to the center of the waveguide. Noise or error in the measurement of $S(y)$ for *any* y will have an impact on the value of $f(r = 0)$, so uncertainty in plasma density increases towards $r = 0$. In practice, this uncertainty often takes the form of negative plasma density, which while physically absurd serves as a good indication of the region of validity of $f(r)$.

Computing the Abel inversion of these 50 basis functions is time consuming (> 10 minutes), but only has to be done once. We also computed Abel inverison of larger FFT basis sets to process signals with more pixels, but 50 pixels was often enough. This algorithm is much faster than direct numerical integration of $S(y)$, finishing in milliseconds rather than minutes. This robust, real-time phase extraction and Abel inverion is crucial for fully exploiting the control we have over the fine structure of the corrugated plasma waveguide.

Chapter 4

Review of pulse-driven molecular alignment

4.1 Laser-driven alignment, multishot measurement techniques

Small linear molecules like nitrogen (N_2), oxygen (O_2), or nitrous oxide (N_2O) typically rotate at terahertz frequencies in their room-temperature gas phase [63]. Rotational transitions in molecules resonantly absorb and emit terahertz radiation if the molecule has a dipole moment, while optical frequencies are completely non-resonant with molecular rotation. However, intense optical pulses can influence the rotation of small molecules by distorting the molecule's cloud of bound electrons [64]. This distortion oscillates rapidly with each optical cycle, but produces a cycle-averaged torque that aligns the molecular axis with the laser polarization direction.

Molecular alignment by intense lasers has been used to control high-harmonic generation [65], where the efficiency of the harmonic generation process depends on the direction of the molecular axis relative to the exciting laser field. Molecular alignment drives refractive index changes in gas, which has been used to compress short wavelength pulses [66]. These same refractive index modulations have significant impact on the propagation of intense laser pulses over extended distances in the atmosphere [67].

When the aligning laser pulse is short compared to the terahertz timescale of molecular rotation, molecular alignment can persist long after the laser pulse
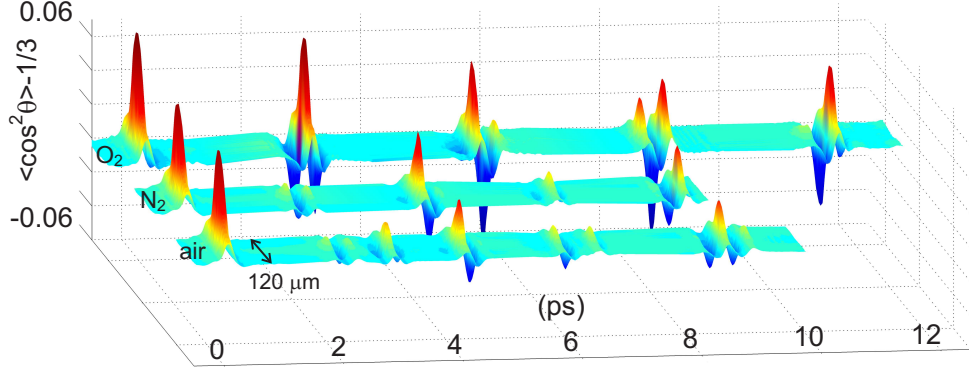
Figure 4.1: Measured alignment $\langle \cos^2(\theta) \rangle$ vs. time and space, of nitrogen (N_2), oxygen (O_2), and air, driven by a single 100 fs, $\sim 10^{13}$ W/cm^2, 800 nm pulse. The measurement technique is described in [69].

has departed. This 'field-free' alignment was originally observed using multi-shot pump-probe techniques [68]. Figure 4.1 shows data from a single-shot measurement technique used recently in our lab to measure the modulation of the refractive index of air by an intense optical pulse [69].

The optical pulse driving alignment is intense ($\sim 10^{13}$ W/cm^2) and short (~ 100 fs) compared to the picosecond timescale typical of molecular rotation. After a prompt increase due to this short pulse, the refractive index of the gas returns to its equilibrium value with $\langle \cos^2(\theta) \rangle = 1/3$. However, several picoseconds *after* the optical pulse, the molecules realign, producing a fast refractive transient. This is a purely quantum mechanical phenomenon, showing that molecular rotation is coherent and nearly undisturbed by collisions for many picoseconds, at room temperature and atmospheric pressure. A detailed study of these transients in air and other gases is given in [69], including the first single-shot measurements of alignment of deuterium and hydrogen molecules.
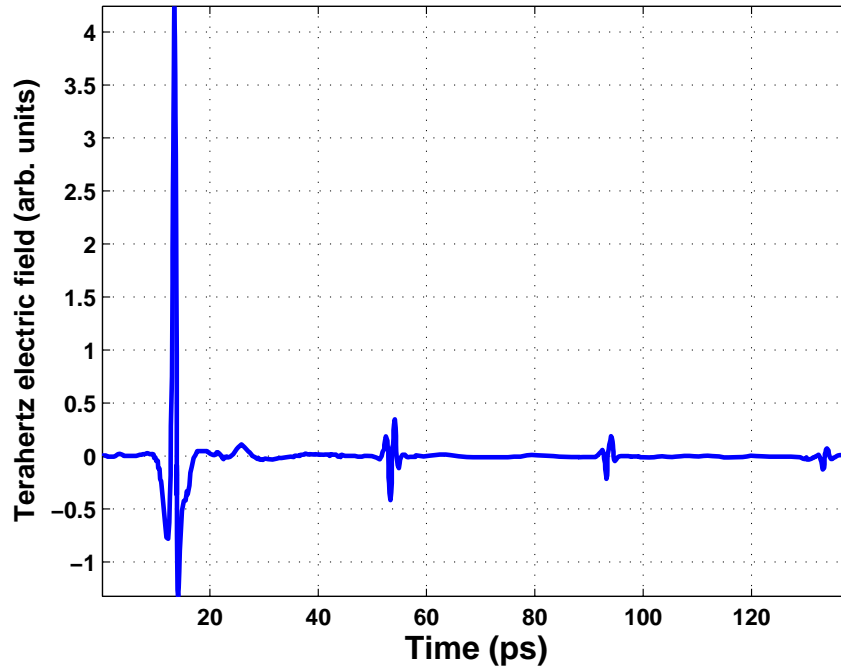
Figure 4.2: Initially few-cycle terahertz pulse measured after transmission through 38.7 cm of 800 hPa N_2O. Adapted from Harde and Grischkowsky, J. Opt. Soc. Am. B Vol. **8**, No. 8, Aug. 1991 [70].

4.2 THz-driven alignment

Molecular alignment can also be driven resonantly at terahertz frequencies. Figure 4.2 shows the result of passing a few-cycle, ~ 3 picosecond terahertz pulse through 38.7 cm of 800 hPa N_2O [70]. The similarity to Figure 4.1 is striking; a prompt response driven by the initial pulse is followed by several 'bursts' of signal each separated by a constant number of picoseconds. However, this signal is not refractive index, as in Figure 4.1; it is the electric field of the transmitted terahertz pulse.

Because N_2O has a permanent dipole moment, its rotation can be resonantly

driven by terahertz radiation. During each oscillation of the terahertz pulse's electric field, the molecule has enough time to change orientation significantly, exchanging energy with the terahertz field. The dipoles which are rotating away from the electric field direction are slowed down, and the dipoles which are rotating towards the field direction are sped up, driving coherence between the orientations of each molecule. By orienting the molecular dipoles, this drives a net polarization of the N_2O gas. After the initial terahertz pulse has passed, the molecules continue rotation as in Figure 4.1, but when the molecules realign many picoseconds later, their dipole moments produce a net polarization that re-radiates at terahertz frequencies. This re-radiation produces the few-cycle pulses of terahertz radiation visible at delays near 55, 95, and 135 picoseconds in Figure 4.2.

4.3 The possibility of terahertz emission from laser-driven molecular alignment

Figure 4.1 shows that intense laser pulses can control molecular rotation, and Figure 4.2 shows that molecular rotation can emit few-cycle pulses of terahertz radation. This raises an intriguing question: Can optical pulses be used to drive molecular rotation to emit terahertz radiation?

High-power terahertz radiation is notoriously difficult to produce. CO_2 lasers have been used to pump vibrational transitions in dipolar molecules like D_2O and methanol (CH_3OH), which can drive rotational population inversion for lasing at teraherz frequencies [71]. Commercial cw CO_2/CH_3OH terahertz lasers are avail-

able [72], but produce only a few tens of milliwatts of peak power. More powerful terahertz pulses can be produced by using short CO_2-laser pump pulses [73, 74], but these vibrationally resonant techniques only drive population inversion of one rotational transition, producing terahertz pulses with hundreds of cycles.

Amplified femtosecond lasers can produce few-cycle pulses of terahertz radiation using optical rectification [75] or photoconductive switching [76]. However, the conversion efficiency of these schemes is typically fairly low; a review of these methods is presented in [15]. One should read [15] carefully; they appear to confuse micro-joules with nano-joules in several places (perhaps due to typographical error), overstating terahertz pulse energies by three orders of magnitude.

Recent work has produced terahertz pulses with ~ 10 μJ energy, using sub-picosecond, 20 mJ optical pulses and a novel phase matching technique in lithium niobate [77]. However, even this record energy still gives conversion efficiency of only 5×10^{-4}. Higher-power terahertz pulses have been produced using transition radiation from relativistic electrons [78, 79], but this requires large accelerator facilities or multi-terawatt lasers, in addition to the health hazards of relativistic electrons.

Molecular rotation after terahertz orientation as shown in Figure 4.2 produces few-cycle terahertz pulses, but obviously the energy of these pulses must be less than the energy of the incident terahertz pulse which produces the orientation. It is much easier to produce high-energy optical pulses, and as shown in Figure 4.1 optical pulses drive similar rotational behavior in small linear molecules.

N_2 and O_2 will not re-radiate terahertz upon alignment, of course, because they have no permanent dipole moment. Even laser-aligned molecules *with* a dipole

moment (like N_2O) will not re-radiate terahertz. The laser alignment mechanism torques a molecule to point co-axially with the electric field, but since this mechanism does not depend on the dipole moment of the molecule [80], there is no preference between parallel and anti-parallel molecular orientations. An initially thermal gas will exhibit no net polarization after laser alignment, and so it will not re-radiate terahertz.

However, since both optical and terahertz radiation interact with the rotation of small linear molecules, a combination of optical and terahertz pulses incident on a molecular gas could result in a transfer of energy from the optical pulse to the terahertz pulse. We hope to combine the high average power of optically pumped terahertz lasers [72] with the few-cycle pulses typical of impulsively-excited molecular rotation to produce extremely high power terahertz pulses. In the remainder of this work, we describe our theoretical and experimental progress towards terahertz generation from laser-aligned molecules.

Chapter 5

Molecular alignment simulation

5.1 The rigid rotor model of molecular rotation

A small linear molecule in a low-pressure, room temperature gas is likely to be in its vibrational and electronic ground state [63]. The lowest excited vibrational energy of hydrogen cyanide (HCN), for example, is 88.3 milli-eV higher than the ground state [81], and therefore ~ 30 times less populated at 300 K. Rotational excitation is much more likely; HCN's lowest excited rotational energy is only 0.36 milli-eV above the ground state [63]. At 300 K, the ground and first excited rotational state population of HCN differ by $< 2\%$.

A rotating molecule in the electronic and vibrational ground state can be modeled as a *rigid rotor* [63]. The rigid rotor Hamiltonian $\hat{H}_{\mathrm{rr}}$ is similar to the hydrogen atom Hamiltonian but with no radial degree of freedom, given in spherical coordinates by:

$$\hat{H}_{\mathrm{rr}} = -\frac{\hbar^2}{2I} \left[\frac{1}{\sin\theta} \frac{\partial}{\partial\theta} \left(\sin\theta \frac{\partial}{\partial\theta} \right) + \frac{1}{\sin^2\theta} \frac{\partial^2}{\partial\varphi^2} \right] \tag{5.1}$$

where I is the moment of inertia of the molecule. The spherical harmonics $Y_j^m(\theta, \varphi)$ are eigenfunctions of this Hamiltonian:

$$\hat{H}_{\mathrm{rr}} Y_j^m(\theta, \varphi) = \frac{\hbar^2}{2I} j(j+1) Y_j^m(\theta, \varphi) \tag{5.2}$$

Each $Y_j^m(\theta, \varphi)$ represents a state of definite rotational angular momentum; j is the

angular momentum quantum number, and m ($|m| \leq j$) is the quantum number for the z-component of angular momentum. Since the rigid rotor eigenenergies differ by integer multiples of the $j = 0 \rightarrow j = 1$ transition energy $\hbar^2/I$, a rigid rotor wavepacket

$$\Psi_{rr}(\theta, \varphi, t) = \sum_{j=0}^{\infty} \sum_{m=-j}^{j} a_j^m Y_j^m(\theta, \varphi) \exp\left(-i\frac{\hbar}{2I}j(j+1)t\right) \tag{5.3}$$

is periodic with period $T_r = 2\pi I/\hbar$ (neglecting collisions). Each a_j^m is a complex number specifying the amplitude and phase at $t = 0$ of each spherical harmonic in the wavepacket. T_r is typically many picoseconds for small linear molecules. HCN, for example has $T_r = 11.49$ ps, whereas for the heavier carbonyl sulfide (OCS), $T_r = 82.65$ ps [63].

Applied electric fields modify molecular rotation. A rigid rotor with permanent dipole moment μ along the internuclear axis and polarizability components $\alpha_\parallel$ and $\alpha_\perp$ parallel and perpendicular to this axis, in an external electric field $\vec{E}$ has the modified Hamiltonian [82]:

$$\begin{aligned}
\hat{H}_{rr+\vec{E}} &= \hat{H}_{rr} + V_\mu(\theta) + V_\alpha(\theta) \tag{5.4} \\
&= \hat{H}_{rr} - \mu E \cos\theta - \frac{1}{2}E^2\left(\alpha_\parallel \cos^2\theta + \alpha_\perp \sin^2\theta\right)
\end{aligned}$$

where θ is the angle between $\vec{E}$ and the molecular axis, and $E \equiv |\vec{E}|$. Instantaneous 'eigenfunctions' of this modified Hamiltonian [82] are less useful to us, because in our lab the disturbance $\vec{E}$ is often in the form of a subpicosecond pulse with pulse duration $T_{\text{pulse}} \ll T_r$. For short pulses of $\vec{E}$ it is convenient to work in the rigid rotor basis and keep track numerically of how $\vec{E}$ drives changes in the coefficients a_j^m of Equation 5.3.

Note that a circularly polarized optical pump pulse has nearly the same interaction with a gas of linear molecules as a linearly polarized pump pulse with the same pulse duration and energy. The only change in the cycle-averaged Hamiltonian is that the effective sign of $\Delta\alpha$ changes from positive to negative, and the polar (z) direction now points in the laser propagation direction instead of in the laser polarization direction [83]. Our simulations (not shown) show that this interaction drives the same changes in rotational populations $\Delta\rho_{j,j}^m$ with positive or negative $\Delta\alpha$. Circular polarization has been observed to drive alignment and anti-alignment like linear polarization [84], in contrast with the predictions of [85].

In moderate strength, low frequency electric fields, the permanent dipole interaction $V_\mu(\theta)$, if it exists, dominates the induced polarization interaction $V_\alpha(\theta)$. For example, HCN has a dipole moment of 2.98 debye and a differential polarizability $\Delta\alpha$ ($\equiv \alpha_\parallel - \alpha_\perp$) of 1.91 Å^3 [63, 86]. In a 1 V/m electric field, $\mu_{HCN}E = 9.9 \times 10^{-30}$ J, while $\Delta\alpha_{HCN}E^2 = 2.13 \times 10^{-40}$ J.

Gigahertz or terahertz ($10^9 - 10^{12}$ Hz) radiation is near resonance for most rotational transitions [63], and affects the rotation of molecules primarily through the permanent dipole interaction, if it exists. The electric fields of optical pulses, however, oscillate at nearly petahertz (10^{15} Hz) rates (much faster than T_r for HCN) and the $V_\mu(\theta)$ interaction time-averages to zero, leaving only the $V_\alpha(\theta)$ interaction, which cycle-averages to half the DC value ($V_{\alpha,\text{AC}} = \frac{1}{2}V_{\alpha,\text{DC}}$) for linearly polarized radiation [82]. Despite the smallness of $\Delta\alpha$ for most molecules, amplified femtosecond optical pulses can reach high enough intensity to drive significant changes in the a_j^m coefficients and strongly modify molecular rotation [85, 87].

Such strong optical pulses might also drive vibrational or electronic transitions in a molecule, invalidating the rigid rotor approximation. This excitation could have serious impact on the design of an optically pumped broadband terahertz laser. However, electronic transitions from the ground state are generally resonant with ultraviolet wavelengths, and vibrational transitions from the ground state are typically resonant in the infrared [63]; many molecular gases such as HCN are transparent (nonresonant) near the ~ 800 nm wavelength of most intense femtosecond lasers.

Nonresonant excitation of vibrational and electronic transitions is still possible, but since electronic and vibrational timescales are so much shorter than most femtosecond optical pulses ($T_{\text{electronic}} \ll T_{\text{vibrational}} \ll 15$ fs $< T_{\text{pulse}}$), electronic and vibrational excitation can adiabatically remain in the 'ground state' of an applied optical pulse, and return smoothly to the true ground state after the pulse is gone [88]. Experiments comparing measured molecular alignment in CO_2 to the rigid rotor model [89] have found good agreement even for laser intensity exceeding the molecular ionization threshold, implying that neglect of electronic and vibrational excitation is an acceptable approximation for 90 fs, 800 nm alignment pulses.

5.2   Statistical description using a density matrix

To study the feasibility of an optically pumped broadband terahertz laser, we need to perform full-scale nonperturbative numerical simulations of the rotational quantum state of a gas of dipolar molecules illuminated by femtosecond optical

and terahertz pulses. Direct simulation of $\Psi(\theta, \varphi, t)$ is straightforward for a single molecule, but for an ensemble of molecules (such as a small volume of gas), the thermal distribution of initial quantum states means a large number ($\gg 10^3/\mu\mathrm{m}^3$) of molecules must be simulated and averaged for accurate results.

The density matrix formalism [90] describes an ensemble of identical noninteracting quantum mechanical systems with a statistical distribution of initial conditions. If each quantum system can be described by a superposition of N_{st} basis states, the density matrix contains at most N_{st}^2 variables. Direct simulation of each of N_{sys} quantum systems would require keeping track of $N_{\mathrm{st}} N_{\mathrm{sys}}$ variables, so the computational savings are considerable when the number of systems greatly exceeds the number of quantum basis states needed to describe each system ($N_{\mathrm{sys}} \gg N_{\mathrm{st}}$), as in the case of a gas of rigid rotors.

Using the Dirac notation and defining $|j, m\rangle$ by

$$\langle \theta, \varphi | j, m \rangle = Y_j^m(\theta, \varphi) \tag{5.5}$$

where $|\theta, \varphi\rangle$ is an angular position eigenstate, we define a density matrix $\boldsymbol{\rho}$:

$$\boldsymbol{\rho} = \sum_{j=0}^{\infty} \sum_{m=j}^{-j} \sum_{k=0}^{\infty} \sum_{n=k}^{-k} \rho_{j,k}^{m,n} |j, m\rangle \langle k, n| \tag{5.6}$$

$\boldsymbol{\rho}$ describes the quantum state of an ensemble of identical, noninteracting rigid rotor molecules subjected to the same electromagnetic field, such as a volume of gas much smaller than one cubic optical wavelength. The expectation value of any observable $\boldsymbol{O}$ of the ensemble can be computed from $\boldsymbol{\rho}$ according to:

$$\langle \boldsymbol{O} \rangle = \mathrm{Tr}(\boldsymbol{O}\boldsymbol{\rho}) \tag{5.7}$$

where Tr() is the trace operation [90]. A density matrix modeling a system with Hamiltonian $\hat{H}$ evolves in time according to:

$$i\hbar\frac{\partial \boldsymbol{\rho}}{\partial t} = [\hat{H}, \boldsymbol{\rho}] \tag{5.8}$$

where $[A, B] \equiv AB - BA$ is a commutator.

Substituting the Hamiltonian from equation 5.4 for $\hat{H}$ and assuming $\vec{E}$ is linearly polarized in the z-direction, $\boldsymbol{\rho}$ time-evolves according to [69, 91]:

$$\begin{aligned}
\frac{d}{dt}\rho_{j,k}^m(t) &= -i\omega_{j,k}\rho_{j,k}^m(t) + (d\rho_{j,k}^m/dt)_{\text{diss}} + \\
&\quad \frac{-i\Delta\alpha}{4\hbar}E_{\text{optical}}^2(t)\sum_q[O_{j,q}^m\rho_{q,k}^m(t) - O_{q,k}^m\rho_{j,q}^m(t)] + \\
&\quad \frac{-i\mu}{\hbar}E_{\text{terahertz}}(t)\sum_q[T_{j,q}^m\rho_{q,k}^m(t) - T_{q,k}^m\rho_{j,q}^m(t)]
\end{aligned} \tag{5.9}$$

Where:

- $\omega_{j,k} = \omega_j - \omega_k$, $\omega_j = (\pi/T_r)j(j+1)$, $\Delta\alpha$ is the difference in the molecule's parallel and perpendicular polarizability and μ is its permanent dipole moment. For HCN $T_r = 11.49$ ps, $\Delta\alpha = 1.91$ Å^3, and $\mu = 2.98$ debye [63, 86].

- $E_{\text{optical}}^2(t)$ is the squared envelope of a nonresonant optical electric field which interacts through $V_\alpha(\theta)$, and $E_{\text{terahertz}}(t)$ is the full electric field (not the envelope) of a low frequency terahertz or gigahertz pulse that interacts primarily through $V_\mu(\theta)$ [70, 83].

- Since we are only considering electric fields which point in the z-direction, quantum states with different values of m are not coupled to each other [69] (they're also zero in thermal equilibrium, as we will discuss). For this reason,

we neglect elements of the density matrix for which $m \neq n$ and substitute $\rho_{j,k}^{m,n} \rightarrow \rho_{j,k}^m$.

- $O_{j,k}^m$ and $T_{j,k}^m$ describe how optical (O) and terahertz (T) radiation couple different elements of the density matrix. $O_{j,k}^m = \langle j, m | \cos^2(\theta) | k, m \rangle$, which is zero unless $j = k$ or $j = k \pm 2$, so optical radiation drives coherence only between states with the same parity [69]. Sufficiently intense optical radiation can be nonlinearly absorbed (or emitted) by $j \rightarrow j \pm 2$ population transitions [85]. The terahertz coupling term $T_{j,k}^m = \langle j, m | \cos(\theta) | k, m \rangle$ is zero unless $j = k \pm 1$, so terahertz radiation drives coherence between states of opposite parity, and is resonantly absorbed and emitted by $j \rightarrow j \pm 1$ transitions at frequency $\omega_{j,j+1}$.

- Finally, $(d\rho_{j,k}^m / dt)_{\text{diss}}$ accounts for the fact that a gas of molecules is not really a set of identical noninteracting quantum systems. Dissipative effects like collisions and emission of radiation drive the gas towards thermal equilibrium [91]. Interactions between the gas molecules are generally extremely complicated and prohibitively difficult to model precisely, but this term at least acknowledges the complication and leaves it to be specified later.

So $\boldsymbol{\rho}$ describes a gas of rigid rotor molecules (equation 5.6), from which we can compute observables (equation 5.7), and we know how to time-evolve $\boldsymbol{\rho}$ (equation 5.9). We only need the initial condition of $\boldsymbol{\rho}$ to begin simulation, and most of the gas targets in our lab start in thermal equilibrium. In thermal equilibrium at temperature T, the population of rotational states $\rho_{j,j}^m$ is given by Boltzmann

statistics:

$$\frac{\rho_{j,j}^m}{\rho_{0,0}^0} = \exp\left(\frac{-\hbar\omega_j}{k_B T}\right) \tag{5.10}$$

Where k_B is Boltzmann's constant. In thermal equilibrium there is no coherence between molecules and no preferred direction, so $\rho_{j,k\neq j}^m = 0$ and we normalize $\boldsymbol{\rho}$ such that $\sum_{j,m} \rho_{j,j}^m = 1$. Our simulations apply a sequence of optical and terahertz pulses to an intially thermal HCN gas, and the resulting changes in population $\Delta\rho_{j,j}^m$ give the average energy absorbed/emitted per molecule $\Delta E = \sum_{j,m} \hbar\omega_j \Delta\rho_{j,j}^m$ from each of the pulses.

Since we neglect back-action of the molecular emission on the ensemble, we can calculate transitions driven by the applied pulses but not self-stimulated transitions like those observed in free-induction decay [70]. A more accurate simulation would take into account the macroscopic polarization and radiation of the medium and allow self-generated electric fields to influence $\boldsymbol{\rho}$, but this would require including nonlocal effects such as propagation (solving the coupled Maxwell-Bloch equations) and increase the simulation burden beyond our resources. Since we are primarily concerned with prompt absorption or amplification of short optical and terahertz pulses, and self-stimulated emission generally occurs many picoseconds after applied electric fields, this is a reasonable approximation.

5.3 Details of the simulation algorithm

$\boldsymbol{\rho}$ as described in equation 5.6 is specified by an infinite number of terms $\rho_{j,k}^m$. In practice, only a finite number of these terms are nonzero. The Boltzmann factor

in equation 5.10 decreases rapidly with increasing j, and the vast majority of terms $(\rho_{j,k\neq j}^m)$ in the thermal density matrix are negligible. Selecting which elements of the density matrix to include is the primary challenge of our numerical simulations.

Applied optical and terahertz fields drive these initially negligible elements of the density matrix to nonzero values. However, because of the $j \pm \{1,2\}$ coupling in equation 5.9, external fields must drive amplitude changes sequentially. $\rho_{3,7}^2$, for example, will have negligible amplitude until the amplitude of at least one of $\rho_{3\pm\{1,2\},7}^2$ or $\rho_{3,7\pm\{1,2\}}^2$ is significant.

Sufficiently weak applied fields may only drive one 'generation' of amplitude away from thermal equilibrium. In ref. [69], for example, experiment agrees well with 'first order' theory that only considers the time evolution of density matrix elements $\rho_{j,j\pm2}^m$, for laser intensity $\sim 10^{13}$ W/cm^2. However, in order to study an optically-pumped terahertz laser, we must be able to accurately calculate large fractional changes in $\rho_{j,j}^m$ which are neccesary for population inversion. Clearly this requires more than a 'first order' simulation, in which changes in $\rho_{j,j}^m$ are assumed zero.

We initially tried a naive approach of numerical simulation including *all* $\rho_{j,k}^m$ with $\{j,k,m\} \leq j_{\max}$. This approach is very accurate and simple to code, and allows simulation of very high intensity applied fields. However, this approach ultimately was too computationally intensive and limited us to simulation of low initial-temperature gases for which $j_{\max}$ can be small. By including elements with large differences between j and k which have rapid phase evolution, we force ourselves to use a small timestep, and we waste simulation effort by including elements

61

which never become significantly nonzero.

A more intelligent approach is required; we want our simulation to include the $\rho_{j,k}^m$ which will be nonnegligible, but no others, and we don't know before we run a simulation if our parameters will drive significant amplitude into a given $\rho_{j,k}^m$. Perhaps the best way to proceed is to *grow* our density matrix adaptively, adding elements $\rho_{j,k}^m$ to our simulation as they become important. The following algorithm provided a nice balance between computational burden and accuracy: For a given set of molecular parameters and a given applied optical/terahertz field pattern, determine which $\rho_{j,k}^m$ are above an 'amplitude threshold', and declare this to be the set of 'fully considered' elements $\{\rho_{j,k}^m\}_f$. Then:

- Construct the set of all elements which are not 'fully considered', but are coupled to 'fully considered' elements by the applied optical and terahertz fields. Declare these elements to be 'boundary' elements $\{\rho_{j,k}^m\}_b$. For example, if $\rho_{4,6}^1$ is a 'fully considered' element, and terahertz fields are present ($j \pm 1$ coupling), and $\rho_{5,6}^1$ (which is coupled to $\rho_{4,6}^1$ by terahertz radiation) is not an element of $\{\rho_{j,k}^m\}_f$, then $\rho_{5,6}^1$ is an element of $\{\rho_{j,k}^m\}_b$.

- If the set of $\{\rho_{j,k}^m\}_f$ and $\{\rho_{j,k}^m\}_b$ is large enough for accurate simulation, the boundary elements should not get very big. If any of $\{\rho_{j,k}^m\}_b$ were to reach large amplitude, they should couple to elements that are not included in the simulation, and inaccuracy in the time evolution of the boundary elements will result. Therefore, if any of $\{\rho_{j,k}^m\}_b$ exceeds the 'amplitude threshold', stop the simulation before much inaccuracy results. If no $\{\rho_{j,k}^m\}_b$ exceeds the amplitude

threshold at $t = t_{\text{final}}$, the simulation is finished.

- If the simulation stops due to a large boundary element, promote that element to a 'fully considered' element, go back a few time steps in the simulation, and return to the first step in this list.

Accuracy of the simulation is sensitive to the 'amplitude threshold'. Halving the amplitude threshold and rerunning the simulation is a good way to check results for convergence; the second simulation will take much longer, but if it returns the same result, you can trust it. Running the simulation over again from the start using $\{\rho_{j,k}^m\}_f$ and $\{\rho_{j,k}^m\}_b$ from a prior run with the same parameters often results in slightly different results, which is another way to tell if your amplitude threshold is too big.

Symmetry offers several important speedups. Note that there is no difference in the differential equation for positive or negative values of m, and that $\rho_{j,k}^m = \rho_{k,j}^{m,*}$, which gives a factor of four improvement in speed and memory. The fact that different m-values do not couple is also helpful. For some simulation parameters, the full simulation including all $\rho_{j,k}^m$ is too big to fit nicely in the memory of a single workstation, and running separate simulations for different m-values simultaneously gives a nice speed boost. We took advantage of the Maryland high-performance computing cluster *deepthought* [92] to run 20 or more m-values at a time.

One might expect the final sets $\{\rho_{j,k}^m\}_f$ and $\{\rho_{j,k}^m\}_b$ to give enough information for an intelligent guess about $\{\rho_{j,k}^{m\pm1}\}_f$ and $\{\rho_{j,k}^{m\pm1}\}_b$. In practice, this could often lead to more rapid convergence to a sufficiently small 'amplitude threshold', but it

also lead to unneccesary inclusion of $\rho_{j,k}^m$ with large values of $|j - k|$, which rapidly oscillate and slow the simulation. For serial jobs (one m after another) this offered some advantage, but was nearly useless for parallel jobs.

For future optimization we plan to make the change of variables $\lambda_{j,k}^m = \rho_{j,k}^m \exp\left(-\mathrm{i}\omega_{j,k}t\right)$, which leads to a modified differential equation. Initial tests show this gives approximately a factor of two improvement in simulation speed, but this may depend on simulation parameters and the exact mechanism of speedup is unclear.

Chapter 6

Using optical pulses to drive population inversion in aligned

molecules

6.1   Motivation

Broadband chirped-pulse amplification (CPA) in Ti:sapphire revolutionized

nonlinear optics in the 90's, bringing intense optical pulses out of large govern-

ment facilities and into the hands of graduate students in small university labs.

High peak-power terahertz pulses ($\gg$ 10 μJ, $<$ 5 cycles), however, are still only

produced at large accelerator facilities like BNL [78]. CPA is theoretically possi-

ble for terahertz frequencies, but no broadband lasing medium like Ti:sapphire has

been demonstrated for terahertz. Dipolar molecular gases such as hydrogen cyanide

(HCN) or nitrous oxide (N_2O), 'aligned' or rotationally excited by intense optical

pulses, are a novel and promising medium for amplification of broadband few-cycle

terahertz pulses.

Using the techniques described in the previous chapter, we perform calcula-

tions to study if rotationally excited molecules can amplify a few-cycle seed pulse

of terahertz radiation. Our proposed scheme is shown in Fig. 6.1: a short, intense

optical pulse (or sequence of pulses) aligns a dipolar gas (such as HCN), driving the

molecules into a broad superposition of excited rotational states. If the right rota-
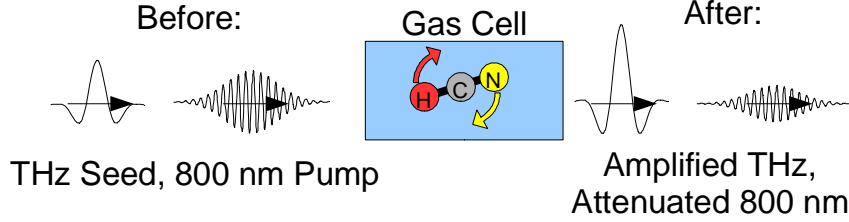
Figure 6.1: Proposed broadband terahertz amplification

tional ensemble is prepared, a broadband seed terahertz pulse following the optical pulses can then be amplified on many pure rotational transitions simultaneously.

Since HCN or N_2O have a dipole moment, they can absorb and emit radiation through rotational transitions. The rotational spectrum of a gas of linear molecules is a series of regularly spaced lines in the low-terahertz frequency range [63]. Absorption and emission depend on the state of the gas; there is no coherence in thermal equilibrium ($\rho_{j,k \neq j}^m = 0$), so the strength of the linear absorption in the terahertz region depends on the population differences $\delta\rho_{j,j}^m$ ($\equiv \rho_{j,j}^m - \rho_{j-1,j-1}^m$) between adjacent rotational states [70]. Since $\delta\rho_{j,j}^m < 0$ in thermal equilibrium, the rotational spectrum is purely absorbing.

Following intense, femtosecond optical pumping, however, molecular gas is driven into an 'aligned' excited rotational state [69]; the terahertz spectrum of this excited state is strongly modified. If the gas is sufficiently excited, $\delta\rho_{j,j}^m > 0$ for many j, and its rotational spectrum contains a set of regularly spaced amplification lines. The duration of the 'aligned' excited state is determined by collisions. The pressure-dependent alignment lifetime of small linear molecules is tens or hundreds of picoseconds at or below atmospheric pressure (68.5 ps for N_2O at 1 atm [69]),

and increases linearly with decreasing pressure. A few-cycle terahertz seed pulse could follow a few picoseconds behind an optical pump pulse train and be strongly amplified by many of these lines simultaneously. Of course, if the gas is in a coherent ensemble, absorption can also depend on the correlation between molecules $\rho_{j,k\neq j}^{m}$, as discussed in Chapter 8.

6.2 Low pressure, room temperature

As shown in Fig. 6.2, a series of short intense optical pulses can drive HCN gas into an excited, inverted rotational state suitable for broadband terahertz amplification. Figure 6.2(a) shows the initial rotational population of the gas in thermal equilibrium at 310 K: $\rho_{j,j}^{m}$ decreases with j and is independent of m. Illumination by a single 15 TW/cm^2, 100 fs, 800 nm optical pulse drives coherence ($|\rho_{j,k\neq j}^{m}| > 0$) between the gas molecules, but as shown in Fig. 6.2(b), causes little change in the rotational populations $\rho_{j,j}^{m}$. Arbitrarily increasing the intensity of the optical pulse would drive larger changes in the rotational populations, but would also cause undesired effects like vibrational excitation, self-focusing, or ionization.

Luckily, a *train* of pulses can drive *much* larger changes in rotational populations. At low gas pressures ($\ll$ 1 atm) collisions are rare and $(d\rho_{j,k}^{m}/dt)_{\text{diss}} \ll T_r$. The field-free $\boldsymbol{\rho}(t)$ of a rigid-rotor gas is then perfectly periodic with period T_r, and a sequence of small pulses separated by T_r build up resonantly to the same effect as a single pulse with the same total energy. In Fig. 6.2(c), four 15 TW/cm^2, 100 fs, 800 nm optical pulses separated by $T_{r,HCN} = 11.49$ ps strongly invert the popu-

lation of the HCN gas; each molecule absorbs $\sim 4.6 \times 10^{-21}$ J of rotational energy (for pressures < 1atm, this is a small fraction of the optical energy). $\rho_{j,j}^m$ increases with j for nearly every transition from $j = 5$ to $j = 19$; a broadband terahertz pulse could be amplified simultaneously by all these transitions. The optical pulses drive population to higher j values by strongly aligning the molecules; a rigid rotor highly localized in θ must occupy a broad spectrum of j states, and tighter angular localization projects into higher j. The irregularity of $\rho_{j,j}^m$ at low j shown in Figure 6.2(c) is due to the strong dependence of $O_{j,k}^m$ (from equation 5.9) on j for $j \approx m$.

The simulation results are identical (neglecting ionization) to a single pulse with intensity 60 TW/cm^2. Impressively, a train of 600, 0.1 TW/cm^2 pulses separated by T_r gives the same result. Splitting the pulse energy into a train of smaller pulses avoids undesired intensity-dependent effects, and would allow recycling the same optical pulse in a cavity for high efficiency. The number of times a pulse can be reused for pumping is limited by the pressure-dependent alignment lifetime; the results in Fig 6.2(c, f) are appropriate for pressures $< 10^{-2}$ atmospheres.

6.3 Moderate pressure, room temperature: the effects of dissipation

High pressures are desirable for high single-pass gain and high saturation energy. Low pressures are desirable because they allow many optical pulses to contribute to the population inversion; a compromise is necessary. In general, the dissipation of the density matrix toward thermal equilibrium is complicated [91] and not well studied experimentally, so we adopt the simple model $(d\rho_{j,k}^m/dt)_{\text{diss}} =$
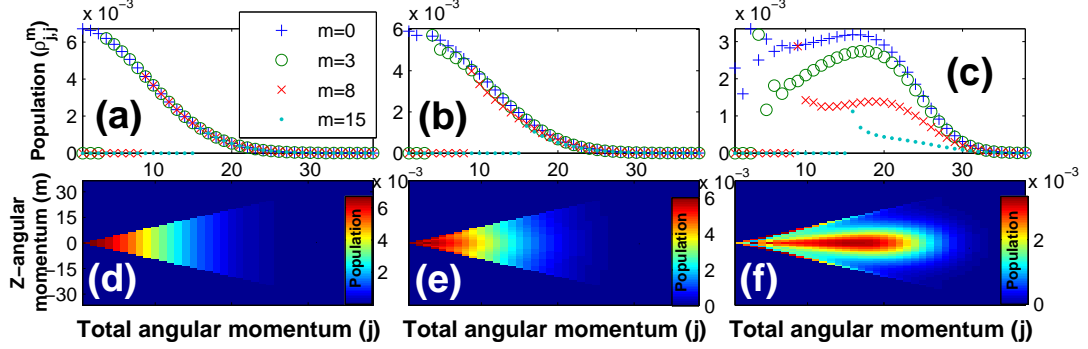
Figure 6.2: Rotational state populations ρ_{jj}^m vs. j of HCN gas for selected m-values **(a)** before illumination (thermal population), **(b)** after illumination by a 15 TW/cm^2, 100 fs, 800 nm optical alignment pulse, and **(c)** after a train of four such pulses separated by 11.49 ps (the revival time of HCN). Below are intensity plots of ρ_{jj}^m vs. j and m for **(d)** thermal, **(e)** one-pulse, and **(f)** four-pulse illumination.

$\gamma(\rho_{j,k}^m - \rho_{j,k,\text{thermal}}^m)$. As shown in Fig. 6.3, for very low pressures ($1/\gamma > 1$ ns), four-pulse optical pumping drives a strong population inversion, but dissipation in the range $1/\gamma = 200 - 300$ ps (corresponding to pressures of ~ 0.01 atm) decreases the strength and the bandwidth of the population inversion for the $m = 0, 1$ cases (other m's are similar). Increasing the number of pump pulses from four to five, however, returns some of the inversion strength and more than restores the bandwidth. Estimating $\Delta\nu_{j-1,j} \approx \Delta\nu_{0,1}$ and $\gamma \approx 2\pi\Delta\nu$, these decay times are appropriate for a pressure of ~ 0.014 ($1/\gamma = 300$ ps) and 0.02 ($1/\gamma = 200$ ps) atmospheres [93].

Gain at these pressures would be fairly low. Further simulations at higher pressure (> 0.02 atm) (not shown) suggest that the number of pump pulses required to drive strong population inversion rises prohibitively. As the collision time becomes comparable to T_r, the decay of rotational excitation between pump pulses balances the pumping excitation and a pumping equilibrium is reached. For a given pump
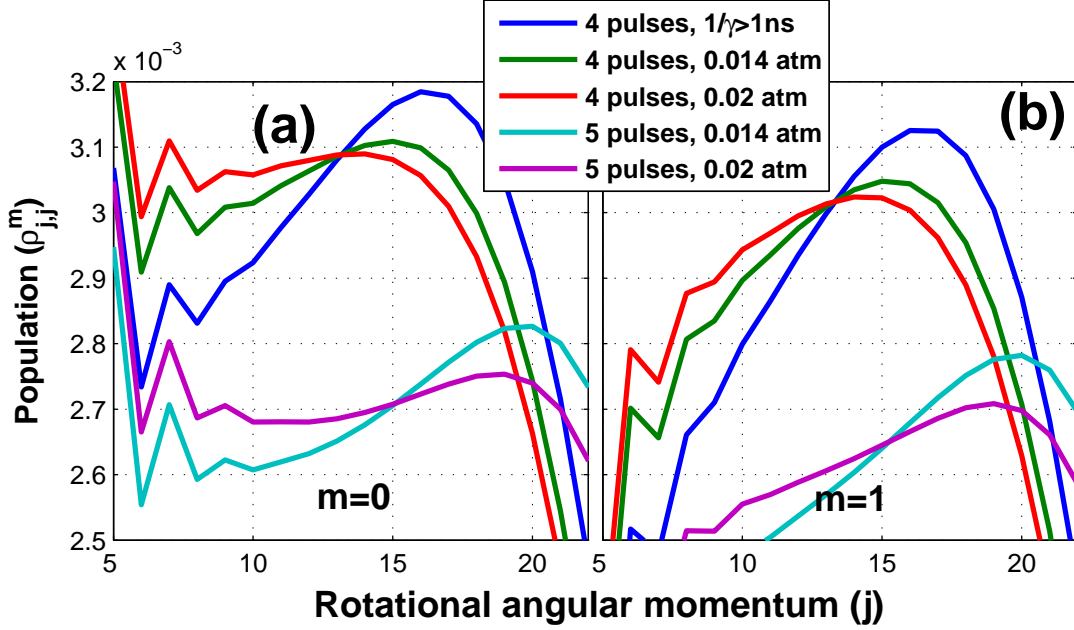
Figure 6.3: Population $\rho_{j,j}^m$ for different dissipation rates γ and number of optical pump pulses for (a) $m = 0$ and (b) $m = 1$.

intensity, there is some critical pressure above which no population inversion is possible, no matter how many pump pulses are used. Fortunately, increasing the pressure of a room-temperature gas target is not the only way to increase gain.

6.4 Low temperature gas jet targets

Decreasing temperature to decrease collisions without sacrificing density is appealing, but HCN's vapor pressure drops off rapidly for temperatures below 300 K. The use of a gas jet rather than a static gas target allows the use of higher density targets at lower rotational temperature and long collision times.

When a gas expands into a vacuum through a nozzle, the pressure and temperature both drop abruptly. If the backing pressure is high enough, collisions in

70
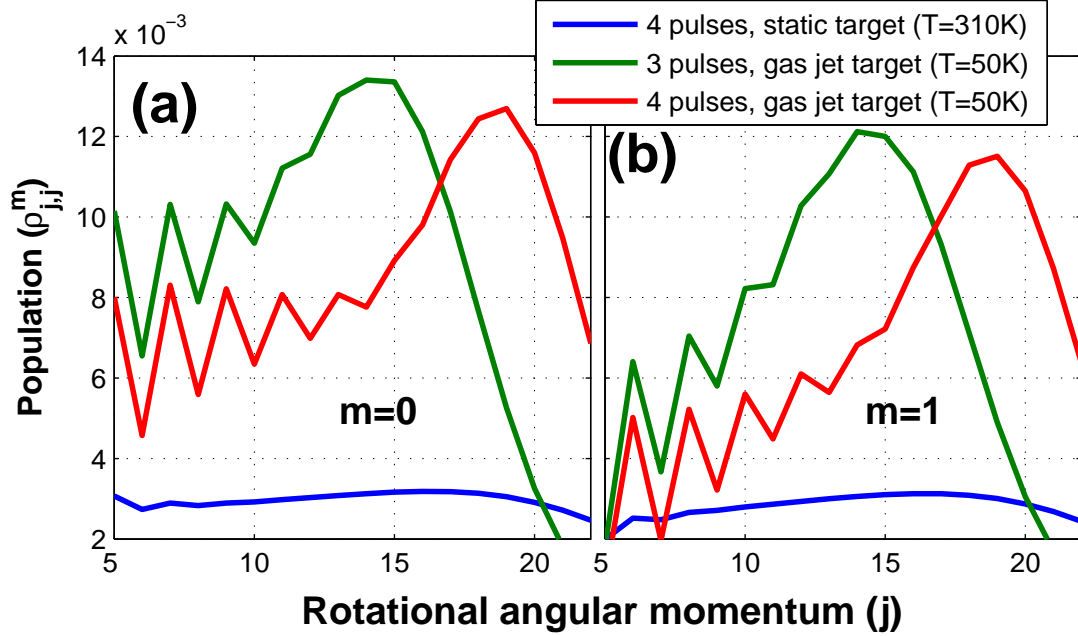
Figure 6.4: Population $\rho_{j,j}^m$ for static gas and gas jet initial temperatures T for (a) $m = 0$ and (b) $m = 1$, neglecting collisions ($1/\gamma \gg 1$ns).

the nozzle bring the gas molecules to nearly the same direction and velocity. This process efficiently cools molecular rotation and to a lesser extent, vibration [94, 95]. Rotational cooling in a supersonic gas jet has been shown to increase the efficiency of optical alignment of molecules [96].

As shown in Fig. 6.4, a low temperature ($T = 50$K) HCN gas jet target gives a much stronger population inversion after four-pulse optical pumping than in uncooled ($T = 310$K) static HCN, resulting in much more optical absorption and terahertz gain per molecule. Additionally, low temperatures concentrate population in low m-states which have a larger effective dipole interaction with terahertz fields. Estimating $\gamma_{\mathrm{jet}} = \gamma_{\mathrm{static}} \sqrt{T_{\mathrm{jet}}/T_{\mathrm{static}}}$ at comparable density, collisional decay would be 2.5 times slower in a gas jet. The lower temperature of the gas jet also makes

population inversion easier to achieve. At low pressures ($1/\gamma \gg$ 1ns), only three optical pulses still drive a strong population in 50K HCN, although with a reduced inversion bandwidth.

6.5   Overpumping

As shown in Fig. 6.2(c), four pump pulses drive a population inversion in low-pressure, room temperature HCN gas from $j = 5$ to $j = 19$, corresponding to resonant transitions at frequencies < 1.6 THz. To amplify higher frequencies, the population inversion must be pushed to higher j values. One way to accomplish this is to use more pump pulses: Figure 6.5 shows the $m = 0$ populations $\rho_{j,j}^0$ vs j after each of 12 pulses in a train of of 15 TW/cm^2, 100 fs pulses spaced by the revival time T_r, for the same parameters used in Figure 6.2. Four pulses drives a population inversion, but each successive pulse drives this inversion to higher j, extending the inversion as far as $j = 36$ by the twelfth pulse, nearly doubling the highest inverted resonant frequency.

This behavior suggests a simple intensity-based mechanism to tune the center frequency of terahertz gain. Unfortunately, our computational resources are insufficient to explore the limits of this behavior, but the trend shown in Figure 6.5 is promising.
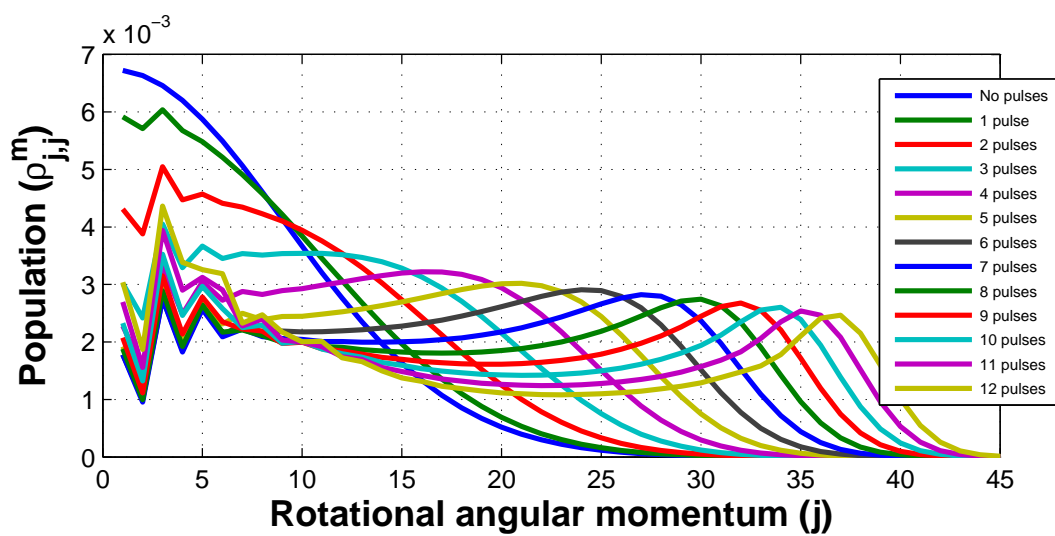
Figure 6.5: Population $\rho_{j,j}^m$ driven by a variable number of 15 TW/cm^2, 100 fs optical pump pulses, for a static HCN gas target at 310 K neglecting collisions $(1/\gamma \gg 1\text{ns})$.

Chapter 7

Using inverted rotational populations to amplify THz pulses

7.1 Amplification bandwidth, THz pulse duration

In Chapter 6, we showed that four optical pulses can drive a strong population

inversion in low pressure, room temperature HCN (Fig. 6.2). Figure 7.1 shows the

effect of this four-pulse optical excitation on HCN's absorption of a 200 fs, single-

cycle terahertz pulse that follows $T_r/2$ behind the last optical pulse. In Chapter

6 we were interested in driving population inversion, so we displayed rotational

populations $\rho_{j,j}^m$. Here we are primarily concerned with absorption or amplification

of terahertz pulses, which may drive small fractional changes in $\rho_{j,j}^m$, so we instead

display energy absorbed or emitted due to the terahertz pulse, $\Delta E_j^m = \hbar \omega_j \Delta \rho_{j,j}^m$.

Since transition frequency is m-independent, we also display $\Delta E_j = \sum_m \Delta E_j^m$.

At 310 K without optical excitation, the $j \to j-1$ transitions are purely

absorptive (Fig. 7.1(**a, c**)) at resonant frequencies $2jf_0$ when illuminated with the

broadband single-cycle pulse shown in Fig 7.1(**e**). Some of this energy is reemited as

a train of short terahertz pulses at integer multiples of T_r [70]; however, as mentioned

in Chapter 5, this free induction decay is beyond the scope of our simulation. The

width of these absorption lines (alternatively, the number of pulses emitted by free

induction decay) depends on pressure. The HCN $j = 0 \to 1$ linewidth $2\Delta f \approx$

38 GHz/atm [93], corresponding to an alignment lifetime of ~ 200 ps at 0.02 atm

Figure 7.1: Energy absorbed/emitted (ΔE_j^m) by 200 fs-pulse THz-driven $j \rightarrow j \pm 1$ transitions vs. j and m of the upper state for **(a)** an initially thermal HCN gas and **(b)** the optically-excited rotational populations shown in Fig. 6.2**(c, f)**. Summed over m, this gives energy absorbed/emitted (ΔE_j) near each resonant frequency $2jf_0$ for **(c)** thermal and **(d)** excited gas. The ~ 200 fs terahertz pulse driving these transitions **(e)** follows at $T_r/2$ after the last optical excitation pulse.

pressure.

However, if the same terahertz pulse follows $T_r/2$ behind the last optical excitation pulse from Fig. 6.2(c), the 19 lowest absorption lines become amplification lines. This comb of amplification frequencies extends from 0.08 THz to 1.6 THz, as shown in Fig. 7.1(b, d) and the degree of amplification is comparable to the degree of absorption without excitation. In the 0-1.6 THz band, each unexcited HCN molecule would absorb about $\sim 6.4 \times 10^{-29}$ J of energy; with excitation, each molecule instead emits $\sim 3.6 \times 10^{-29}$ J. The seed terahertz pulse has a fluence of about 5 nJ/cm^2, which could be generated in femtosecond-illuminated ZnTe. Extracting 3.6×10^{-29} J from each molecule means a small-signal gain of about 0.85 nJ/cm^2 per centimeter of propagation, per atmosphere of HCN pressure. After propagating only a few centimeters, the high-frequency component (> 1.6 THz) of the seed pulse's spectrum will be completely absorbed and the remaining amplified spectrum will closely match the amplification band ($0 - 1.6$ THz), indicating significant pulse reshaping.

The absorption of the terahertz pulse depends on relative delay between the optical pump pulses and the terahertz pulse. $\Delta t = T_r/2$ was chosen after limited exploration because it seemed to maximize gain, but full exploration of Δt for the parameters discussed here is beyond our computational resources. Chapter 8 discusses the effect of Δt on terahertz absorption in more detail.

The ~ 200 fs terahertz pulse used in Fig. 7.1 is too short to be efficiently amplified, since most of its spectrum lies above the 0-1.6 THz amplification band. Figure 7.2 shows the same calculation for a longer (~ 800 fs) terahertz pulse with the
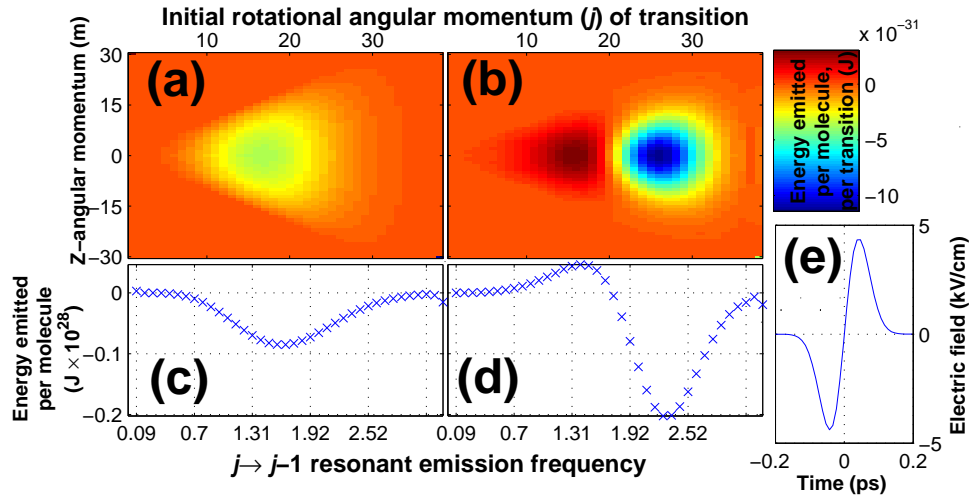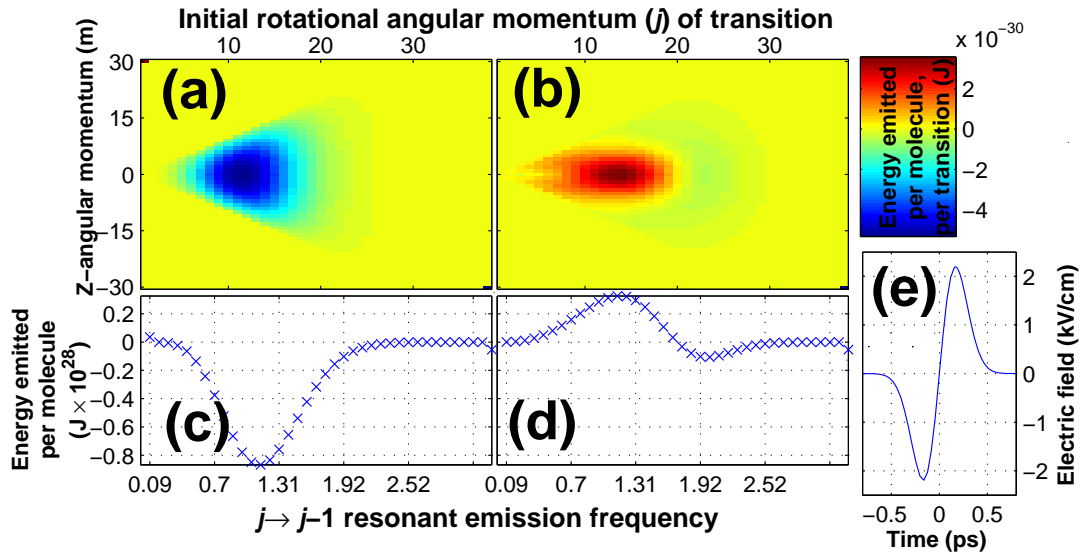
Figure 7.2: Energy absorbed/emitted (ΔE_j^m) by 800 fs-pulse terahertz-driven $j \to j \pm 1$ transitions vs. j and m of the upper state for **(a)** an initially thermal HCN gas and **(b)** the optically-excited rotational populations shown in Fig. 6.2**(c, f)**. Summed over m, this gives energy absorbed/emitted near each resonant frequency $2jf_0$ for **(c)** thermal and **(d)** excited gas. The ~ 800 fs terahertz pulse driving these transitions **(e)** follows at $T_r/2$ after the last optical excitation pulse.

same fluence. The longer pulse better overlaps both the amplification and thermal absorption bands. In the 0-1.6 THz band, each unexcited HCN molecule would absorb about $\sim 8 \times 10^{-28}$ J of energy; with excitation, each molecule instead emits $\sim 3 \times 10^{-28}$ J, giving a more respectable gain of 7.1 nJ/cm^2 per centimeter of propagation per atmosphere of HCN. Note also that there is very little absorption of this pulse by the excited molecules shown in Fig. 7.2(b, d), indicating little pulse reshaping.

The temporal shape of this terahertz emission depends on collisions. The time-domain simulation used here only calculates the energy ΔE absorbed or emitted while the seed pulse interacts with the molecules, so post-pulse terahertz emission is not considered. At low pressures ($\ll 1$ atm), in addition to absorbing or amplifying the original pulse, molecular rotations will remain coherent for many T_r and will also generate a following train of few-cycle terahertz pulses spaced by T_r [70]; this is beyond the scope of our simulation. However, use of a cavity to pass the terahertz pulse repeatedly through the excited low-pressure gas allows collection of this excess energy into the original seed pulse, further increasing gain.

The extracted energy shown in Figures 7.1 and 7.2 is less than 10^{-6} of the absorbed optical pump energy. Maximum extractable energy can be estimated because the first three optical pump pulses drive HCN to the cusp of inversion, and only the fourth optical pump pulse drives population inversion. A strong terahertz pulse which saturates extraction would drive the populations back to this uninverted state, extracting ~ 41 mJ/cm^3 per atmosphere of pressure. For pressures of $\sim 1\%$ of an atmosphere, this is a small fraction of the input pulse.
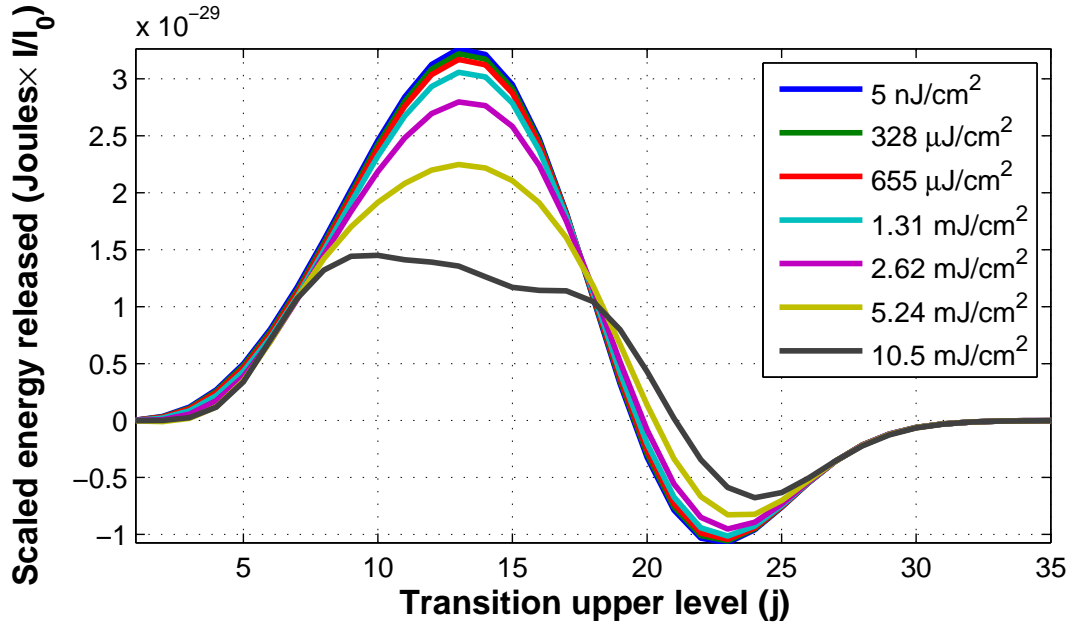
Figure 7.3: Scaled gain vs. frequency for a range of terahertz pulse fluences

Saturated extraction will generally drive population transitions and nonlinear effects, but the 5 nJ/cm^2 terahertz pulse fluence studied here is well below saturation; doubling the terahertz intensity precisely doubles the extracted energy from each transition. Figure 7.3 shows the effects of saturation on gain for high terahertz pulse fluences, comparing the extracted energy per transition shown in Figure 7.2(d) for a 5 nJ/cm^2 terahertz pulse to a range of higher pulse fluences. For easy comparison, this extracted energy is scaled by pulse fluence, so if gain stays linear, the plots will fall on top of one another.

In fact, it takes 16 doublings of pulse fluence to show any significant deviation from this linear behavior; extraction of less than 100 μJ/cm^3 per atmosphere leaves the rotational populations changed by less than one part in 500. For terahertz fluence of $\sim$328 μJ/cm^2, the shape of the gain curve is barely distinguishable from

the 5 nJ/cm² case. Not until ~ 10.5 mJ/cm² does saturation finally drastically change the shape of the gain curve. Since demonstration of a 100 μJ terahertz pulse at a large accelerator facility is a significant achievement [78], and terahertz wavelengths make it difficult to focus to spot areas much smaller than 1 mm² (which would give a fluence of 100 mJ/cm² for the 100 μJ pulse in [78]), this is an extremely promising result.

7.2 Gain at lower temperature

All the data presented in this chapter so far is for low-pressure gas targets where collisions are negligible, corresponding to pressures of $< 10^{-2}$ atmospheres. Gain at these pressures would be fairly low, requiring long interaction lengths for large amplification. Decreasing temperature to decrease collisions without sacrificing density is appealing, but HCN's vapor pressure drops off rapidly for temperatures below 300 K. The use of a gas jet rather than a static gas target allows the use of higher density targets with long collision times. Gas jet targets also have a much lower rotational temperature [96], which makes it easier to drive population inversions, as shown in Figure 6.4 for a low temperature ($T = 50$ K) HCN gas jet target.

Figure 7.4 compares the terahertz gain in this gas jet target to the gain shown in Figure 7.2(**d**), using the same 800 fs single-cycle pulse. The energy extracted per molecule is much larger, about 2.8× more than a room temperature target. This is both because of the steeper population inversions driven in the cold target,
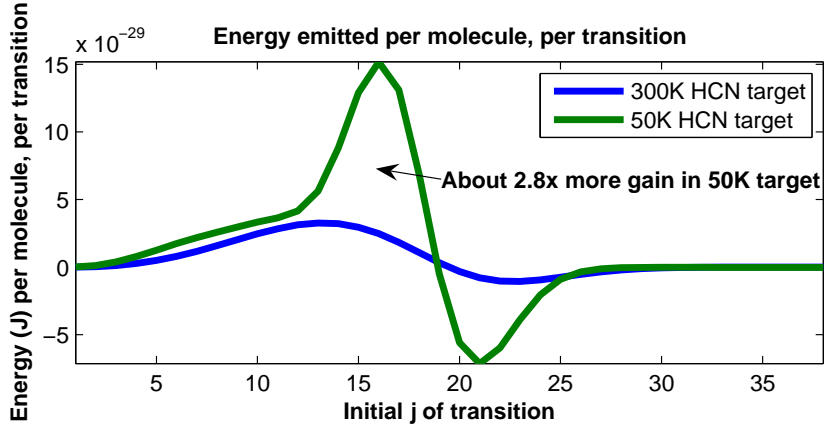
Figure 7.4: Comparison of extracted energy for low- and room-temperature targets.

and because low temperatures concentrate population in low m-states which have a larger effective dipole interaction with terahertz fields. Note that there is more loss at higher frequency in the cold target, indicating that the gain bandwidth of the cold target does not extend quite as high. The 800 fs terahertz pulse used here is not ideally matched to the cold target; a slightly longer pulse with the same fluence would experience even more gain.

Estimating $\gamma_{\text{jet}} = \gamma_{\text{static}}\sqrt{T_{\text{jet}}/T_{\text{static}}}$ and assuming rotational and translational temperatures are similar [94], collisional decay would be 2.5 times slower in 50 K HCN at comparable density. Gas jets can probably achieve even lower rotational and translational temperature [96], allowing higher density with fewer collisions for efficient pumping and long excitation lifetimes, and further increasing terahertz gain.

Chapter 8

Coherent terahertz absorption in laser-aligned molecules

8.1   Suppression or enhancement of absorption

The terahertz amplification shown in Chapter 7 is calculated for a terahertz pulse copropagating with the optical excitation pulses, with constant relative delay $\Delta t = T_r/2$. Interestingly, varying the relative delay between the optical and terahertz pulses can strongly modulate the terahertz absorption or amplification; $\Delta t = T_r/2$ was chosen empirically to optimize amplification.

Chapters 7 and 6 focused on driving population inversions for amplification, but optical pulses that are far too weak to drive changes in population ($\Delta \rho_{j,j}^m \ll \rho_{j,j}^m$) can still create coherence ($\rho_{j,j\pm2}^m \neq 0$). Physically, these pulses are too weak to change the mean rotational energy of a gas of molecules ($\Delta E \ll kT$), but they can still make different molecules in the gas more likely to point in the same direction.

This coherence can have significant impact on terahertz absorption in the excited gas, as shown in Figure 8.1. A 1 TW/cm^2, 100 fs optical pulse weakly aligns a gas of HCN molecules ($|\rho_{j,j\pm2}^m| > 0$ and $\rho_{j,j\pm2}^m/\rho_{k,k\pm2}^m = |\rho_{j,j\pm2}^m/\rho_{k,k\pm2}^m|$ at the peak of the optical pulse) while driving negligible change in populations ($\rho_{j,j}^m \approx \rho_{j,j,\text{thermal}}^m$). The same ~ 200 fs input terahertz pulse as Fig. 7.1 follows the optical alignment pulse with variable Δt; HCN's rotational absorption/emission is wildly modulated by this alignment depending on Δt. For clarity and computational reasons we show
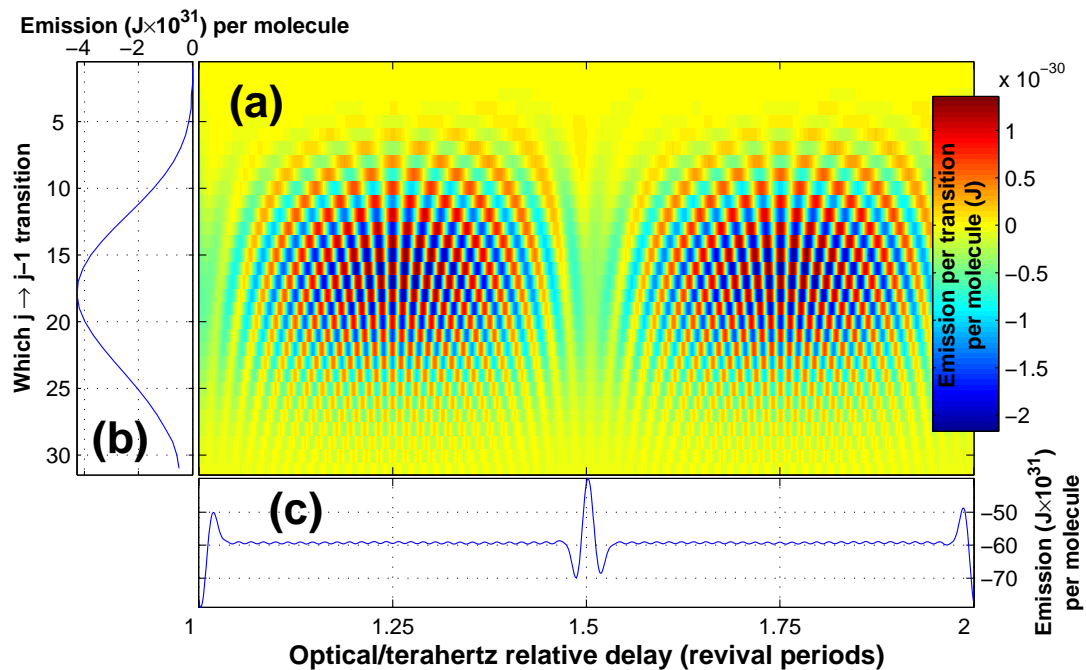
Figure 8.1: A 1 TW/cm^2 optical pulse weakly aligns HCN and strongly modulates (a) terahertz energy absorbed/emitted per molecule, per $m = 0$, $j \rightarrow j - 1$ transition depending on the optical-terahertz relative delay Δt. (b) Averaging over delay shows the 'incoherent' absorption that a terahertz pulse would experience if it was not collinear with the optical pump pulses. (c) Summing over j gives total absorption vs. Δt.

only the $m = 0$ case, but the behavior is similar for all m.

A terahertz pulse copropagating with the optical excitation pulse would have roughly constant Δt, and absorption could be enhanced ($\Delta t = nT_r$, where n is an integer), suppressed ($\Delta t = (n + 1/2)T_r$), or oscillatory in spectrum, as shown in Fig. 8.1(a). In Figure 8.1(c), absorption is summed over j to show absorbed energy ΔE vs. relative delay Δt. Absorption is suppressed by more than 30% at $\Delta t = (n + 1/2)T_r$, and enhanced by $\sim 25\%$ at $\Delta t = nT_r$. If this result for linear molecules could be extended to asymmetric-top molecules like H_2O, then perhaps an optical prepulse could be used to suppress the absorption of terahertz pulses in the atmosphere by water vapor which hampers terahertz remote sensing.

If the terahertz pulse is propagating at some angle to the optical beam path, then Δt will slip, and the terahertz absorption will average over delays as shown in Fig. 8.1(b). The absorption shown in Fig. 8.1(b) is very similar to the thermal absorption for the m=0 portion of Figure 7.1(a). HCN optically driven into a population inversion generally must be described with a much larger density matrix, making an exhaustive scan of Δt computationally infeasible. Our limited simulations (not shown) show that this 'incoherent' delay-averaged absorption depends mainly on populations $\rho_{j,j}^m$ rather than coherences $\rho_{j,k\neq j}^m$, as in [70].

8.2 Extra terahertz revival caused by optical prealignment

As described in Chapter 5, we neglect back-action of the molecular emission on the ensemble. We can calculate transitions driven by the applied pulses but
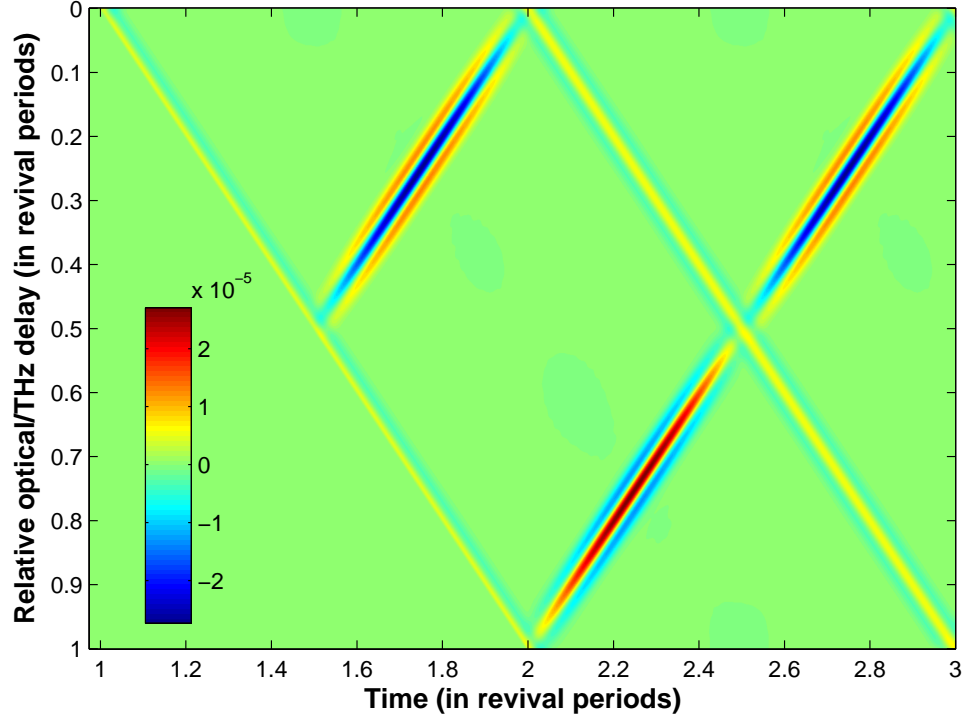
Figure 8.2: Expectation value of orientation $\langle \cos(\theta) \rangle$ vs. time, following the same optical/terahertz pulse pair from Figure 8.1, for different relative delays Δt.

not self-stimulated transitions like those observed in free-induction decay [70]. The absorption shown in figure 8.1 considers only energy absorbed or emitted during the externally applied 200 fs terahertz pulse. Modeling the few-cycle terahertz pulses emitted picoseconds later by free-induction decay would require including nonlocal effects such as propagation (solving the coupled Maxwell-Bloch equations) and increase the simulation burden beyond our resources.

However, we can compute the expectation value of orientation $\langle \cos(\theta) \rangle$ driven by the combination of optical and terahertz pulses. Since this orientation leads directly to macroscopic polarization ($P_z = N\mu\langle \cos(\theta) \rangle$) and emission of short ter-
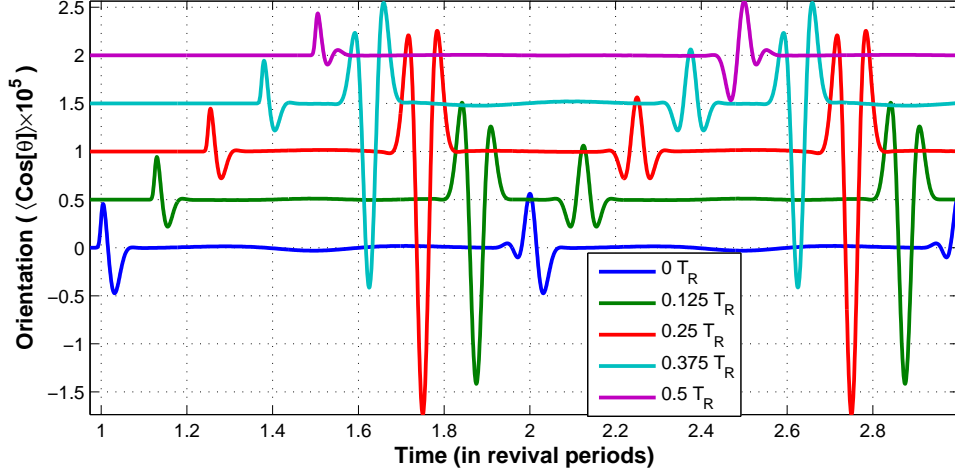
Figure 8.3: Expectation value of orientation $\langle \cos(\theta) \rangle$ vs. time, following the same optical/terahertz pulse pair from Figure 8.1, for selected relative delays Δt. (offset vertically for clarity)

ahertz pulses [70], it is useful for estimating the effects of optical prealignment on terahertz-driven free induction decay.

Figure 8.2 shows $\langle \cos(\theta) \rangle$ vs. time, driven by the same combination of optical and terahertz pulses from Figure 8.1, for a range of relative optical/terahertz delays Δt; the optical pulse arrives at $t = 0$. In the absence of the optical pulse, the terahertz pulse would drive prompt polarization followed by subpicosecond bursts of polarization separated by T_r, as observed in [70].

The addition of the optical pulse causes *extra* revivals, that follow at $nT_r - 2\Delta t$ after the terahertz pulse, where n is an integer. When the 'extra' revivals caused by the optical pulse are well separated from the 'normal' revivals that would occur with the terahertz pulse alone, they are significantly larger. For certain delays ($\Delta t = nT_r/2$), these extra revivals merge into the 'normal' revivals, and become similar in size to 'normal' revivals.

Figure 8.3 shows the same $\langle \cos(\theta) \rangle$ vs. time for selected Δt. Each plot is offset vertically for clarity. The 'extra' revivals are much larger than the 'normal' revivals, as much as five times larger for the $\Delta t = T_r/4$ case. Without considering complicated propagation effects, it is hard to say if this large revival of $\langle \cos(\theta) \rangle$ would give rise to an intense terahertz pulse.

Because of energy conservation, the short terahertz pulses produced in normal free induction decay [70] must contain less energy than the terahertz pulse that drives them. However, the addition of an intense optical prepulse provides an additional reservoir of energy which this process might efficiently transfer to a trailing terahertz pulse. If so, this would represent a promising source of intense terahertz radiation that requires significantly less optical intensity than the amplification scheme described in Chapter 7. We plan to pursue this question in future work.

Chapter 9

Feasibility of experimental study of THz properties of aligned

molecules

9.1   Discussion of gases- HCN, CH_3Cl, OCS, N_2O

Table 9.1 gives an overview of the properties of several linear, dipolar molecular gases that our lab might use to study the effects of molecular alignment on terahertz absorption and emission. The importance of these properties can be understood from Equation 5.9, which describes the time evolution of the rigid rotor density matrix. The effective strength of the terahertz electric field in Eq. 5.9 is multiplied by the dipole moment μ, so a large value of μ is essential for strong terahertz interaction. Similarly, optical field intensity is multipled by $\Delta\alpha$, which is important for strong laser-driven alignment. The rotational revival time T_r (related to moment of inertia I by $T_r = 2\pi I/\hbar$) influences the equation in two ways: it sets the field-free spacing between rotational energy levels through $E_j = (\hbar\pi/T_r)j(j+1)$, which in turn influences the thermal equilibrium distribution of j-states through the Boltzmann factor $\exp\left(\frac{-E_j}{k_B T}\right)$. Effectively, μ, $\Delta\alpha$, and the temperature are all normalized by their product with the moment of inertia I. Finally, the boiling point is important for static gas targets, which give better terahertz amplification when cooled as discussed in Chapter 7. A lower boiling point allows more cooling before condensation limits

gas pressure.

Table 9.1: Overview of dipolar gases for optical/terahertz experiments. Data collected from [63, 86, 97, 98]

Gas	Diff. polarizability $\Delta\alpha$ (esu $\times 10^{-25}$)	Revival time T_r (ps)	Perm. dipole μ (Debye)	Boiling point T_B (K)
HCN	19.1	11.5	2.98	299
CH_3Cl	12.8	37.6	1.9	249
OCS	40-60	83.4	0.709	223
N_2O	27.9	40.5	0.166	185

All of the simulations discussed so far use hydrogen cyanide (HCN) gas. HCN is particularly appealing for optical alignment because of its large ratio of differential polarizibility $\Delta\alpha$ to moment of inertia I, making it easier to drive population inversions; all terms in the rigid rotor equation of HCN's low moment of inertia also means that at a given temperature, more population is concentrated at low j-values which makes it easier to drive population inversion (as shown in Figure 6.4). Low moment of inertia also simplifies multi-pulse optical pumping: a short revival time allows more optical pulses to fit into the same time window, allowing higher pressures before collisions interfere with population inversion. HCN also has a particularly large permanent dipole moment μ, so it interacts strongly with terahertz radiation; the strength of terahertz absorption/amplification generally scales like μ^2 [63]. However, HCN is both poisonous and explosive, which make it undesirable for lab use. Any gas jet target using HCN must solve the difficult engineering problem of how to safely pump the target chamber. HCN's vapor pressure is a bit low, which limits cooling of a static gas target much below room temperature.

Methyl chloride, (CH_3Cl) is inferior in many ways to HCN for optical alignment and terahertz amplification. It has a lower dipole moment, higher moment of inertia, and a smaller differential polarizability. However, CH_3Cl is less dangerous than HCN, so it would be easier to use in a gas jet target, and it has a slightly higher vapor pressure, so it could be cooled more than HCN as a static gas target. CH_3Cl is not a linear molecule, so technically the analysis presented so far does not apply to CH_3Cl. However, since hydrogen is so light, the energy levels corresponding to rotation about the C-Cl axis of CH_3Cl are very widely spaced, and are therefore neglectable for the same reason as vibrational excitation. Finally, the chlorine in CH_3Cl is commonly an isotopic mixture, so unless isotopically pure CH_3Cl is used, multi-pulse optical pumping will discriminate between the two isotopes [99].

Carbonyl sulfide (OCS) is also safer than HCN, and has a very high differential polarizability, which is important for efficiently absorbing energy from optical pulses. The high moment of inertia of OCS makes population inversion difficult to drive, especially at high pressures. Our simulations (not shown) also show initial population inversion in OCS will amplify lower frequencies than HCN, in the 150-450 GHz range; harder optical pumping could drive this amplification to higher frequencies as demonstrated in Figure 6.5. However, once population inversion is achieved in OCS, the high moment of inertia would mean terahertz amplification saturates at much higher energies than in HCN. OCS could be used in a gas jet like CH_3Cl, and can be cooled even more as a static target before condensing. However, the single biggest drawback of OCS is its low dipole moment, leading to a weaker interaction with terahertz than HCN or CH_3Cl. Note that $\Delta\alpha$ of OCS is reported

as $\sim 60 \times 10^{-25}$ esu in [86], but only $\sim 40 \times 10^{-25}$ esu in [100], which would lead to significantly different optical pumping requirements.

Nitrous oxide (N_2O) is even safer than CH_3Cl or OCS, has a low boiling point, and a decent differential polarizability. However, its low dipole moment makes terahertz interactions extremely weak compared to the other gases considered here.

The optical ionization threshold of these gases is also an important parameter, but because the ionization threshold is less clearly defined than the parameters in Table 9.1, it is slightly harder to compare among the different gases. For our purposes, 'ionization threshold' should mean the laser intensity a gas can withstand before the destruction of molecules interferes with amplification and/or the density of free electrons becomes high enough to interfere with the propagation of a terahertz pulse.

Reference [80] estimates an ionization threshold of 140 TW/cm^2 for HCN. If HCN really could withstand this intensity without ionization, a single optical pulse with 60 TW/cm^2 intensity could drive strong population inversion in HCN at extremely high pressure, and a terahertz pulse following close behind could be amplified hundreds of times more strongly than in the low pressure environment required for multi-pulse optical pumping. Experimental investigation is neccesary, but could give a tremendous boost to terahertz amplification.

The ionization threshold of CH_3Cl is well studied in [101], where a laser intensity of 46 TW/cm^2 in a 40 fs pulse produces noticable ionization. Since CH_3Cl requires significantly more laser intensity than HCN to drive population inversion, this probably cannot be done with a single pulse without excessive ionization.

Laser ionization of OCS is studied in [102], and is estimated to occur at 30 TW/cm^2. A single optical pulse with this intensity drives OCS to the cusp of population inversion, so this is certainly worth further study.

9.2   Free space geometry

The suggested terahertz amplification scheme in Figure 6.1 assumes a plane-wave geometry. In practice, construction of a terahertz laser requires getting the propagation of an intense optical pulse and a terahertz pulse to overlap significantly in a dipolar gas. This presents several difficulties:

- A terahertz pulse following an intense optical pulse in a dipolar gas can be amplified, but is strongly absorbed by the same gas in the absence of optical pumping, as shown in Figure 7.1. The terahertz beam must therefore overlap the optical beam nearly everywhere in the amplifying medium.

- Because terahertz radiation has much longer wavelength than optical radiation, a terahertz beam will diffract much more rapidly than an optical beam with the same diameter. This means the optical pump beam must be large to overlap the terahertz beam (at least several mm^2), which requires a high-power optical beam to reach high intensity.

- A beam of optical pulses intense enough to cause rotational population inversion in a gas is typically too intense to touch any solid object (like a lens or mirror) without damaging it; diffraction of the optical pulse can reduce the intensity, but this constrains experimental geometry.
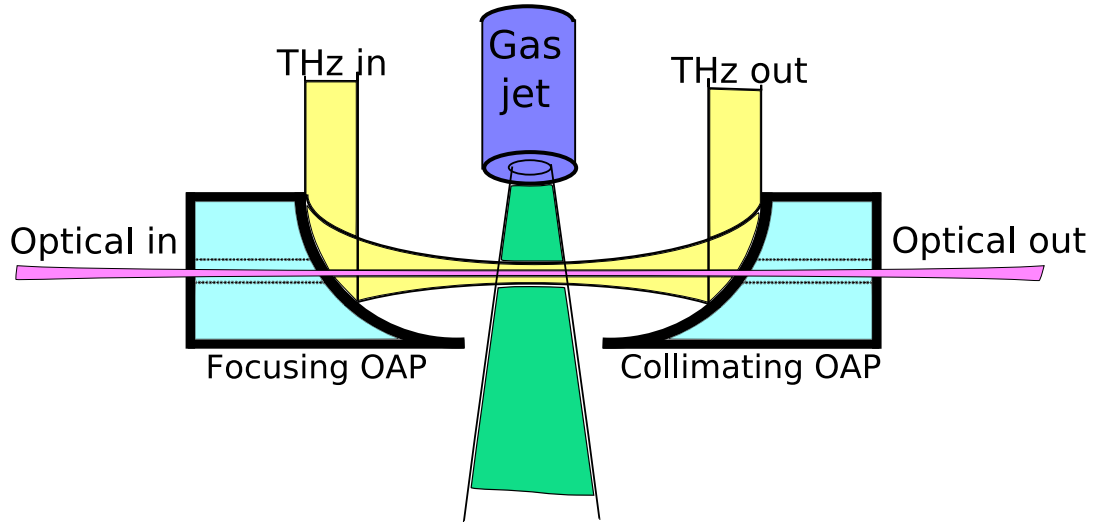
Figure 9.1: Free-space geometry for combining optical and terahertz beams in a molecular gas jet.

- The intense optical beam must not cause excessive ionization of the dipolar gas, which could disrupt terahertz propagation.

Controlling diffraction of the optical and terahertz pulses is essential so that the optical and terahertz beams interact for a long enough distance to give strong amplification.

Figure 9.1 shows one possible way to combine an intense optical beam with a terahertz beam in a gas jet. The optical beam is nearly collimated, with a few-mm diameter beam waist in the center of the figure. The focusing optic for the optical beam is many centimers away from the interaction region, where the beam is large enough to avoid damaging the optic. The terahertz beam has a similarly sized beam waist, but diffracts much more rapidly because of its longer wavelength; it is focused and collimated with a pair of reflective off-axis paraboloids (OAP's) which
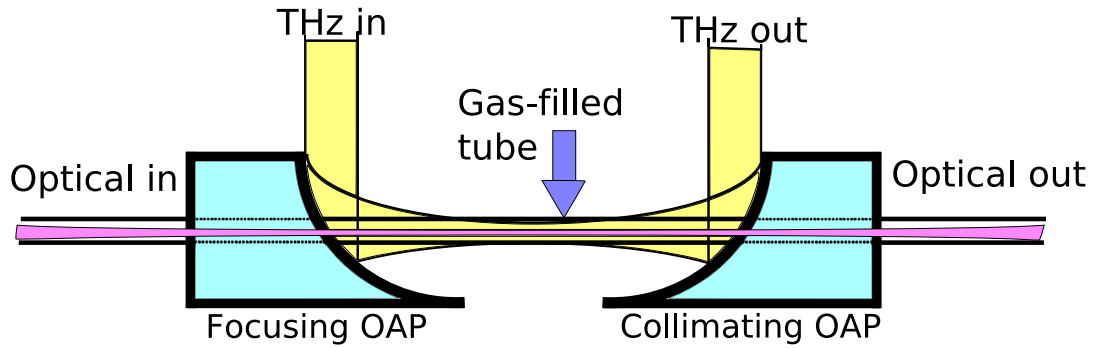
Figure 9.2: Free-space geometry for combining optical and terahertz beams in a static gas-filled tube; the tube is transparent to terahertz radiation.

have a focal length of only a few centimeters. The optical beam passes through a narrow hole drilled in each OAP, and the terahertz and optical beams intersect in a molecular gas jet. The entire assembly is enclosed in a vacuum chamber which must be continuously pumped to keep the backgroud gas pressure low. The terahertz beam only encounters gas directly below the gas jet, which avoids absorption of the terahertz beam before it overlaps the optical beam.

Figure 9.2 shows a similar experimental setup for using a static gas target. The target dipolar gas is confined to the interaction region by a tube made of a material that is transparent to terahertz, such as teflon or polyethylene. The terahertz only passes through gas which is pumped by the intense optical beam, and then diffracts out of the tube to be recollimated by the second OAP. This setup does not require a vacuum chamber or pumping, but the optical beam must enter the gas-filled tube many centimeters from the interaction region to avoid damaging the input window.

In both these cases, spherical aberration of the optical beam is actually desirable; a diffraction-limited spot would be either too intense (ionizing the target gas) and too small (underfilling the terahertz spot), or would diffract very slowly, requiring its focusing optics to be very far from the interaction region.

Diffraction of the terahertz beam limits the interaction length in both these scenarios. A 1 THz beam has a wavelength of $\sim 300\ \mu$m, so if it is focused to a 1 mm^2 spot, it will have a Rayleigh length of only a few millimeters. Weaker focusing to larger spots will give longer interaction lengths, but as the terahertz beam waist grows, the optical beam diameter must also grow. Since optical powers of > 1 TW/cm^2 are required to see strong optical-terahertz interaction, only multi-terawatt lasers could have very long interaction lengths in free-space geometry.

Since the absorption of the optical beam by rotational transitions is very low (as estimated in Chapter 6, in section 6.2), the same optical pump pulse could be recycled and passed through the same gas target many times. Similarly, the terahertz pulse could be passed through the gas for higher gain. Both beams could be placed in a cavity for efficient multi-pass operation.

9.3   Wire guiding geometry

If terahertz diffraction could be suppressed, optical-terahertz interaction lengths could be greatly extended. Of course, the waveguide structure would have to withstand a high-intensity optical beam and allow terahertz radiation to propagate in a dipolar gas.

Wang and Mittleman demonstrated that a bare steel wire can guide terahertz radiation as a surface wave, extending into the gas around the wire [103]. This wire waveguiding method has been used to perform terahertz spectroscopy of lactose powder spread on the surface of the wire [104]. Normally, terahertz spectroscopy requires a high-volume sample [70] for a large-diameter terahertz beam to have a long interaction length. In [104], the wire suppresses diffraction, allowing a very small volume of powder coating the surface of the wire to interact with the terahertz pulse over a long distance. Since the terahertz surface wave only extends ~ 1 mm from the wire, a significant fraction of the beam interacts with the powder over many centimeters of propagation.

If this same wire terahertz waveguide were in a gas chamber surrounded by HCN or CH_3Cl, the guided terahertz pulse would be absorbed by a thin layer of gas surrounding the wire. However, if this thin layer of gas was optically pumped into a rotational population inversion, then the guided terahertz pulse would be amplified. A high-intensity optical pulse could propagate *around* the wire (as described in Section 9.3.2), driving this thin layer into population inversion. Since the hollow optical beam could have a cross sectional area of only a few mm^2, this interaction could be very efficient.

As demonstrated in [103], the $1/e$ attenuation length for wire waveguiding is $>$ 50 cm for frequencies > 0.25 THz. This is near the break-even point for amplification in low-pressure HCN; 1% of an atmosphere of HCN has a gain length of 70 cm for the amplification parameters used in Figure 7.2.

Gain can be increased past this break-even by several methods. Using higher

pressure and an extra pump pulse, as studied in Figure 6.3, can cut the gain length by a factor of two or three. Using a gas jet rather than static gas to surround the wire could increase gain by ~ 10 or more as discussed at the end of Chapter 7, giving gain lengths less than 10 cm. If a single 60 TW/cm^2 optical pulse could drive population inversion in HCN without causing enough ionization to disrupt terahertz guiding, then gas pressures of 1-10 atm could be used, giving centimeter or millimeter gain lengths.

The primary advantage of the wire waveguide is the possibility of extended interaction length. Limited only by diffraction of the optical beam, it could extend interaction for tens or hundreds of centimeters. Since the optical beam needs a cross-section of only a few mm^2, then a regenerative amplifier-based system with a peak power of only a few tens of gigawatts could be used as the optical pump for the coherent effects discussed in Chapter 8. A 2 TW, 100 fs laser system could be used as a pump for the four-pulse population inversion described in Figure 6.2.

9.3.1 Coupling THz onto and off of the wire

Wang and Mittleman use a second steel wire to couple terahertz pulses onto their waveguide [103]. This coupling method is not suitable for the geometry considered here, because it would block the path of the intense optical beam. Cao and Nahata demonstrated an alternative terahertz input coupler by milling a groove directly into the guide wire [105]. This input coupler is well suited for optical/terahertz interaction and would not shadow the optical beam. However, this method suffers

from low coupling efficiency. The same group later improved on this scheme, coating their milled groove with a poled polymer and producing a terahertz pulse directly on the wire [106].

Figure 9.3 shows how this type of terahertz coupling could be used for extended optical/terahertz interaction in a dipolar gas. The input coupler is excited by an optical pulse producing a guided terahertz wave (a pulse from a femtosecond oscillator was used in [106]). The entire assembly is surrounded by a dipolar gas such as HCN. An intense, hollow optical beam precedes the terahertz pulse, driving the surrounding gas into a rotational population inversion. The guided terahertz pulse follows behind and is amplified by the excited gas.

Wire-guided terahertz is most simply outcoupled by terminating the wire; the terahertz rapidly diffracts away [103]. If the wire is not rigid enough and needs support, a deep, wide milled groove like that used in [105] could serve the same purpose. Diffraction will rapidly separate the optical pump beam from the terahertz beam, which could then be divided using a drilled OAP like the ones shown in Figures 9.1 and 9.2. Alternatively, a teflon or polyethylene window in the terahertz path would transmit the terahertz while blocking the optical pulse, preventing absorption of the terahertz radiation by the target gas.
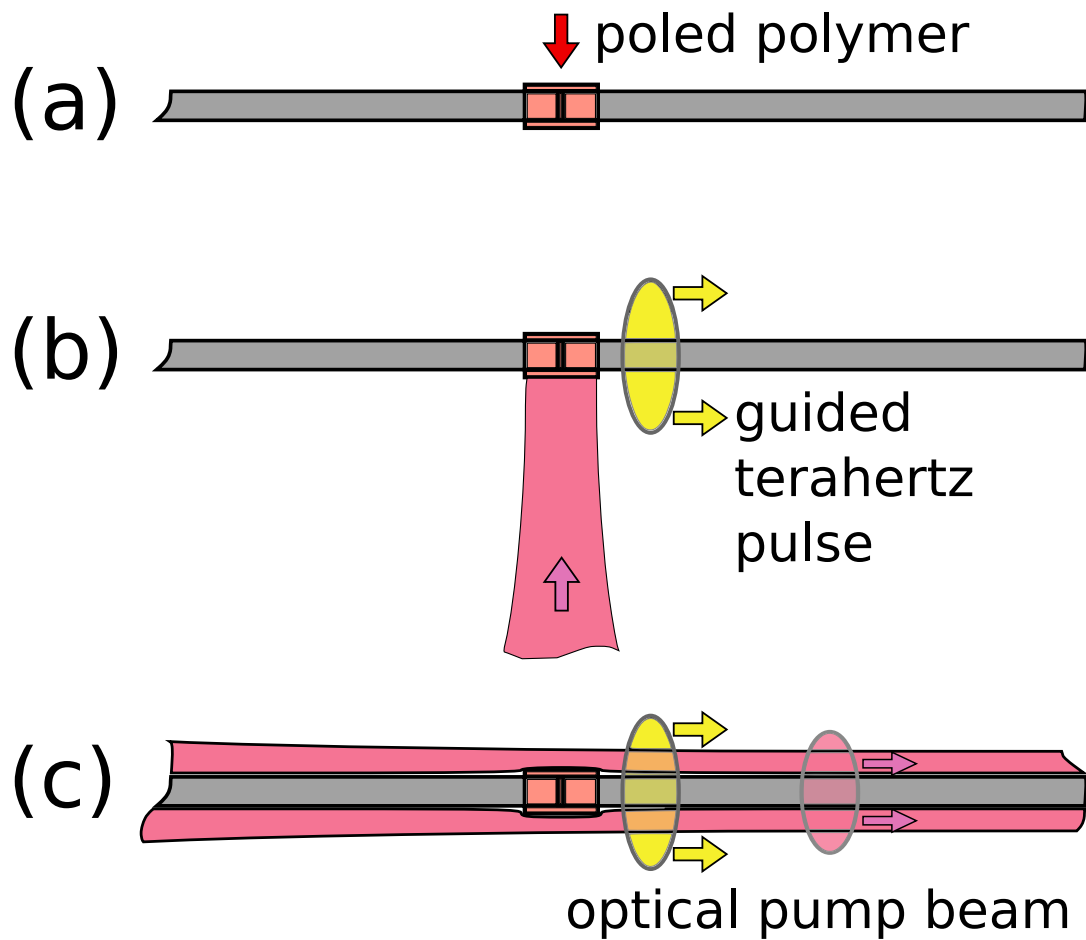
Figure 9.3: **(a)** Steel wire for terahertz waveguiding, coated with a poled polymer [106] and surrounded by a dipolar gas. **(b)** Optical excitation produces a terahertz pulse which is guided along the wire. **(c)** A hollow optical pulse precedes the terahertz pulse, exciting the surrounding dipolar gas to amplify the terahertz.

9.3.2 Skimming the hollow optical beam along the wire: ionization, polarization

It is crucial that the intense optical beam not damage the wire terahertz waveguide. As a preliminary investigation, we suspended a steel wire and surrounded it with an intense optical beam as illustrated in Figure 9.3(c). We used a slightly coverging, 500 GW, 100 fs, 800 nm pulse, and it ranged from ~ 1 cm diameter to ~ 2 mm diameter. No sign of damage could be detected. The wire surface appeared unchanged under a microscope, no 'snapping' noise was audible, and there was no noticable smell. It is possible, of course, that some ionization occured at the surface of the wire, but a more sensitive experiment would be neccesary to measure this effect.

The polarization direction of the optical pulse used in Figure 9.3(c) is also important. All analysis performed in previous chapters considers linearly polarized optical and terahertz polarization, and assumes these polarization vectors point in the same direction. However, the terahertz mode guided by wire waveguides is radially polarized. The optical pump pulse could also be radially polarized for ease of analysis, but this presents experimental complications.

As noted in Chapter 5, circularly polarized light can also drive rotational population inversion. Using a circularly polarized optical pump pulse will generate a cylindrically symmetric gain profile to match the cylindrically symmetric mode of the wire-guided terahertz pulse. Our simulation code currently can only model terahertz polarization in the z-direction, but future work will explore the case of

terahertz linearly polarized in the x or y direction. We expect the optical pump polarization to affect coherent dynamics like those in Chapter 8, but since they drive the same population dynamics as linearly polarized pulses, terahertz gain should be similar.

9.4 Terahertz detection

The detection schemes used in most wire-based terahertz waveguide experiments are multi-shot, scanning techniques [103, 105, 106]. These experiments typically use unamplified femtosecond oscillators with multi-megahertz repetition rates. Molecular alignment typically requires amplified optical pulses with kilohertz or 10-hertz repetion rates, and such systems are not as stable shot-to-shot as unamplified oscillators. Single-shot terahertz detection as used in [107] allows accurate measurement despite shot-to-shot fluctuations. We have constructed a similar terahertz pulse diagnostic based on electro-optic sampling to characterize our terahertz pulses, shown in Figure 9.4. The terahertz beam is combined with an optical beam using a pellicle. Both beams then pass through a zinc telluride (ZnTe) crystal where the terahertz beam underfills the optical beam. The terahertz pulse induces birefringence in the crystal, which distorts the polarization of the optical pulse. The optical pulse is then imaged through a polarizer onto a CCD camera or imaging spectrometer.

The polarizer is oriented to minimize transmission of the optical pulse in the absence of terahertz, so any change in transmission indicates the presence of terahertz radiation. If the optical pulse is transform-limited, the CCD displays a

101
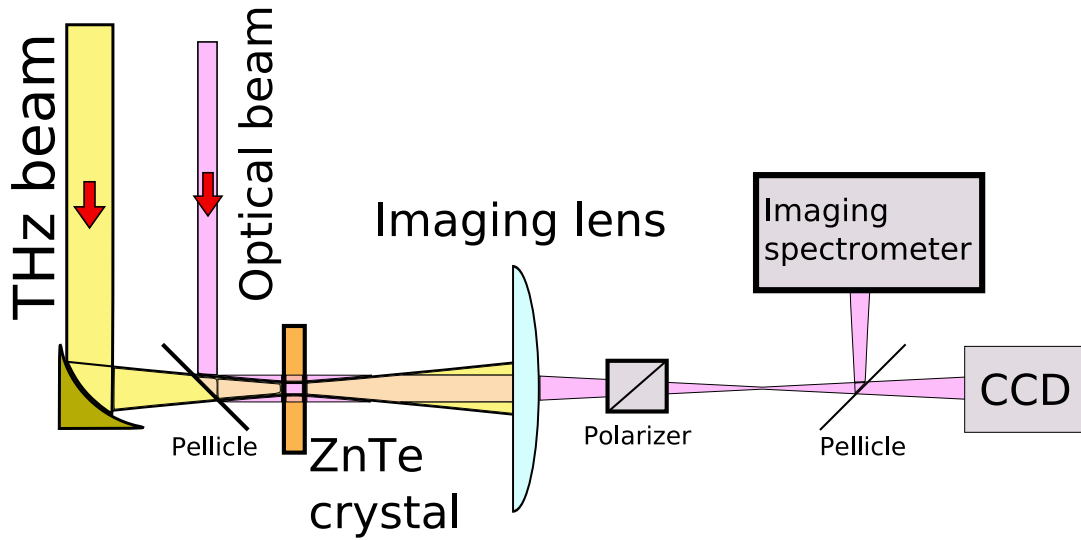
Figure 9.4: Terahertz diagnostic for measuring electric field vs. time and beam profile.

'snapshot' of the terahertz beam profile with time resolution equal to the optical pulse duration. We can measure the electric field vs. time of the terahertz beam by scanning the relative delay between the optical and terahertz beams.

If the optical pulse is chirped, the different frequency components of the optical pulse sample different delays relative to the terahertz pulse. The imaging spectrometer displays the transmission of each frequency component, which can be processed into the electric field vs. time of the terahertz pulse as described in [107].

The pellicle we use has a thickness comparable to our optical wavelength, and exhibits strong variation in reflectivity vs. frequency over the spectrum of the optical pulse. In addition, it is very susceptible to vibration; even a nearbye conversation causes noticable deflection of the optical beam.

The ZnTe crystal [108] shows residual birefringence comparable to the bire-

fringence generated by our terahertz beam. Combined with the spectral modulation of the pellicle and the attenuation due to the grating in our imaging spectrometer, this has prevented us from operating in single-shot mode so far. We plan to replace the pellicle with a small metal mirror. The mirror will block part of the terahertz beam, but will have better stability and higher, more spectrally uniform reflectivity. The brighter probe beam, combined with a more uniform spectrum, should allow single-shot measurement of our terahertz pulse electric field vs. time, with 1-D spatial resolution.

Bibliography

[1] V. Yanovsky, V. Chvykov, G. Kalinchenko, P. Rousseau, T. Planchon, T. Matsuoka, A. Maksimchuk, J. Nees, G. Cheriaux, G. Mourou, and K. Krushelnick. Ultra-high intensity- 300-tw laser at 0.1 hz repetition rate. *Opt. Express*, 16(3):2109–2114, 2008.

[2] http://lasers.coherent.com/lasers/regenerative

[3] T. Ditmire. Nuclear fusion from explosions of femtosecond-laser heated deuterium clusters. *APS Meeting Abstracts*, pages 105–+, November 1999.

[4] K. Kim, I. Alexeev, and H. Milchberg. Single-shot measurement of laser-induced double step ionization of helium. *Opt. Express*, 10(26):1563–1572, 2002.

[5] P. F. Moulton. Spectroscopic and laser characteristics of Ti:Al2O3. *Journal of the Optical Society of America B Optical Physics*, 3:125–133, January 1986.

[6] C. Spielmann, P. F. Curley, T. Brabec, and F. Krausz. Ultrabroadband femtosecond lasers. *IEEE Journal of Quantum Electronics*, 30:1100–1114, April 1994.

[7] D. Strickland and G. Mourou. Compression of amplified chirped optical pulses. *Optics Communications*, 56:219–221, December 1985.

[8] Michael D. Perry and Gerard Mourou. Terawatt to petawatt subpicosecond lasers. *Science*, 264(5161):917–924, 1994.

[9] www.vjultrafast.org/.

[10] A.H. Zewail. Femtochemistry: Atomic-scale dynamics of the chemical bond. *Journal of Physical Chemistry A*, 104(24):5660–5694, 2000.

[11] K. Koenig. Femtosecond laser application in biotechnology and medicine. In I. Miyamoto, H. Helvajian, K. Itoh, K. F. Kobayashi, A. Ostendorf, and K. Sugioka, editors, *Society of Photo-Optical Instrumentation Engineers (SPIE) Conference Series*, volume 5662 of *Society of Photo-Optical Instrumentation Engineers (SPIE) Conference Series*, pages 255–267, October 2004.

[12] J. Krüger, W. Kautek, and H. Newesely. Femtosecond-pulse laser ablation of dental hydroxyapatite and single-crystalline fluoroapatite. *Applied Physics A: Materials Science & Processing*, 69:403–407, 1999.

[13] John L. Hall. Nobel lecture: Defining and measuring optical frequencies. *Reviews of Modern Physics*, 78(4):1279, 2006.

[14] C. Joshi. The development of laser- and beam-driven plasma accelerators as an experimental field. *Physics of Plasmas*, 14(5):055501, 2007.

[15] T Loffler, M Kress, M Thomson, T Hahn, N Hasegawa, and HG Roskos. Comparative performance of terahertz emitters in amplifier-laser-based systems. *Semiconductor Science And Technology*, 20(7):S134–S141, JUL 2005. One should read this reference carefully; they appear to confuse micro-joules with nano-joules in several places (perhaps due to typographical error), overstating terahertz pulse energies by three orders of magnitude.

[16] http://www2.slac.stanford.edu/vvc/accelerators/structure.html.

[17] J. D. Jackson. *Classical electrodynamics*. 92/12/31, New York: Wiley, 1975, 2nd ed., 1975.

[18] Levi Schachter. *Beam-wave interaction in perodic and quasi-periodic structures*. Berlin :Springer-Verlag, 1997.

[19] W. D. Kimura, G. H. Kim, R. D. Romea, L. C. Steinhauer, I. V. Pogorelsky, K. P. Kusche, R. C. Fernow, X. Wang, and Y. Liu. Laser acceleration of relativistic electrons using the inverse cherenkov effect. *Phys. Rev. Lett.*, 74(4):546–549, Jan 1995.

[20] T. Plettner, R. L. Byer, E. Colby, B. Cowan, C. M. S. Sears, J. E. Spencer, and R. H. Siemann. Visible-laser acceleration of relativistic electrons in a semi-infinite vacuum. *Physical Review Letters*, 95(13):134801, 2005.

[21] D. Li and K. Imasaki. Vacuum laser-driven acceleration by a slits-truncated Bessel beam. *Applied Physics Letters*, 86(3):031110–+, January 2005.

[22] J D Lawson. Lasers and accelerators. *Nuclear Science, IEEE Transactions on*, 26(3):4217–4219, June 1979.

[23] Eric Esarey, Phillip Sprangle, and Jonathan Krall. Laser acceleration of electrons in vacuum. *Phys. Rev. E*, 52(5):5443–5453, Nov 1995.

[24] T. Tajima and J. M. Dawson. Laser electron accelerator. *Phys. Rev. Lett.*, 43(4):267–270, Jul 1979.

[25] H. A. H. Boot and R. B. R.-S.-Harvie. Charged Particles in a Non-uniform Radio-frequency Field. *Nature*, 180:1187–+, November 1957.

[26] W. P. Leemans, B. Nagler, A. J. Gonsalves, C. Tóth, K. Nakamura, C. G. R. Geddes, E. Esarey, C. B. Schroeder, and S. M. Hooker. GeV electron beams from a centimetre-scale accelerator. *Nature Physics*, 2:696–699, October 2006.

[27] E. Esarey, P. Sprangle, J. Krall, and A. Ting. Overview of plasma-based accelerator concepts. *Plasma Science, IEEE Transactions on*, 24(2):252–288, Apr 1996.

[28] V. Malka, S. Fritzler, E. Lefebvre, M.-M. Aleonard, F. Burgy, J.-P. Chambaret, J.-F. Chemin, K. Krushelnick, G. Malka, S. P. D. Mangles, Z. Najmudin, M. Pittman, J.-P. Rousseau, J.-N. Scheurer, B. Walton, and A. E. Dangor. Electron acceleration by a wake field forced by an intense ultrashort laser pulse. *Science*, 298(5598):1596–1600, 2002.

[29] "The Light Fantastic", The Economist, Sep 28th 2006.

[30] S. P. D. Mangles, C. D. Murphy, Z. Najmudin, A. G. R. Thomas, J. L. Collier, A. E. Dangor, E. J. Divall, P. S. Foster, J. G. Gallacher, C. J. Hooker, D. A. Jaroszynski, A. J. Langley, W. B. Mori, P. A. Norreys, F. S. Tsung, R. Viskup, B. R. Walton, and K. Krushelnick. Monoenergetic beams of relativistic electrons from intense laser-plasma interactions. *Nature*, 431:535–538, September 2004.

[31] C. G. R. Geddes, C. Toth, J. van Tilborg, E. Esarey, C. B. Schroeder, D. Bruhwiler, C. Nieter, J. Cary, and W. P. Leemans. High-quality electron beams from a laser wakefield accelerator using plasma-channel guiding. *Nature*, 431:538–541, September 2004.

[32] J. Faure, Y. Glinec, A. Pukhov, S. Kiselev, S. Gordienko, E. Lefebvre, J.-P. Rousseau, F. Burgy, and V. Malka. A laser-plasma accelerator producing monoenergetic electron beams. *Nature*, 431:541–544, September 2004.

[33] T. Plettner, P. P. Lu, and R. L. Byer. Proposed few-optical cycle laser-driven particle accelerator structure. *Phys. Rev. ST Accel. Beams*, 9(11):111301, Nov 2006.

[34] B. D. Layer, A. York, T. M. Antonsen, S. Varma, Y.-H. Chen, Y. Leng, and H. M. Milchberg. Ultrahigh-intensity optical slow-wave structure. *Physical Review Letters*, 99(3):035001, 2007.

[35] A. G. York, H. M. Milchberg, J. P. Palastro, and T. M. Antonsen. Direct acceleration of electrons in a corrugated plasma waveguide. *Physical Review Letters*, 100(19):195001, 2008.

[36] H. M. Milchberg, T. R. Clark, C. G. Durfee, III, T. M. Antonsen, and P. Mora. Development and applications of a plasma waveguide for intense laser pulses. *Physics of Plasmas*, 3:2149–2155, May 1996.

[37] J. H. Cooley, T. M. Antonsen, H. M. Milchberg, J. Fan, L. Margolin, and L. Pyatnitskii. Parametric instability in the formation of plasma waveguides. *Physical Review E (Statistical, Nonlinear, and Soft Matter Physics)*, 73(3):036404, 2006.

[38] T. R. Clark and H. M. Milchberg. Optical mode structure of the plasma waveguide. *Phys. Rev. E*, 61(2):1954–1965, Feb 2000.

[39] P Serafim, P Sprangle, and B Hafizi. Optical guiding of a radially polarized laser beam for inverse Cherenkov acceleration in a plasma channel. *IEEE Transactions on Plasma Science*, 28(4):1190–1193, AUG 2000.

[40] CG Durfee and HM Milchberg. Light pipe for high-intensity laser-pulses. *Physical Review Letters*, 71(15):2409–2412, OCT 11 1993.

[41] A. York, B. D. Layer, and H. M. Milchberg. Application of the corrugated plasma waveguide to direct laser acceleration. *Advanced Accelerator Concepts: 12th Advanced Accelerator Concepts Workshop*, 877(1):807–811, 2006.

[42] A. Yariv. *Quantum Electronics*. Wiley, 1989.

[43] Ming Xie. Plasma inverse transition acceleration. *Particle Accelerator Conference, 2001. PAC 2001. Proceedings of the 2001*, 5:3876–3878 vol.5, 2001.

[44] CG Durfee, TR Clark, and HM Milchberg. Mode control in a two-pulse-excited plasma waveguide. *Journal of the Optical Society of America B-Optical Physics*, 13(1):59–67, JAN 1996.

[45] TR Clark and HM Milchberg. Laser-driven implosion of a cylindrical plasma. *Physical Review E*, 57(3, Part B):3417–3422, MAR 1998.

[46] A. Farjadpour, David Roundy, Alejandro Rodriguez, M. Ibanescu, Peter Bermel, J. D. Joannopoulos, Steven G. Johnson, and G. W. Burr. Improving accuracy by subpixel smoothing in the finite-difference time domain. *Opt. Lett.*, 31(20):2972–2974, 2006.

[47] A. York, B. D. Layer, T. M. Antonsen, S. Varma, Y.-H. Chen, and H. M. Milchberg. Ultra-high intensity optical slow wave structure and applications. *AIP Conference Proceedings*, 926(1):152–161, 2007.

[48] R.F. Hubbard, P. Sprangle, and B. Hafizi. Scaling of accelerating gradients and dephasing effects in channel-guided laser wakefield accelerators. *Plasma Science, IEEE Transactions on*, 28(4):1159–1169, Aug 2000.

[49] Andrew G. York, B. D. Layer, J. P. Palastro, T. M. Antonsen, and H. M. Milchberg. Ultrahigh-intensity optical slow-wave structure for direct laser electron acceleration. *J. Opt. Soc. Am. B*, 25(7):B137–B146, 2008.

[50] glue.umd.edu/˜york/scat.mpg.

[51] G. Machavariani, Y. Lumer, I. Moshe, A. Meir, and S. Jackel. Efficient extracavity generation of radially and azimuthally polarized beams. *Opt. Lett.*, 32(11):1468–1470, 2007.

[52] T. van Oudheusden, E. F. de Jong, S. B. van der Geer, W. P. E. M. Op 't Root, O. J. Luiten, and B. J. Siwick. Electron source concept for single-shot sub-100 fs electron diffraction in the 100 kev range. *Journal of Applied Physics*, 102(9):093501, 2007.

[53] T Palchan, S Eisenmann, A Zigler, D Kaganovich, RF Hubbard, M Fraenkel, D Fisher, and Z Henis. All optical electron injector using an intense ultrashort pulse laser and a solid wire target. *Applied Physics B-Lasers and Optics*, 83(2):219–223, MAY 2006.

[54] H. Sheng, K. Y. Kim, V. Kumarappan, B. D. Layer, and H. M. Milchberg. Plasma waveguides efficiently generated by bessel beams in elongated cluster gas jets. *Physical Review E (Statistical, Nonlinear, and Soft Matter Physics)*, 72(3):036411, 2005.

[55] S. P. Nikitin, I. Alexeev, J. Fan, and H. M. Milchberg. High efficiency coupling and guiding of intense femtosecond laser pulses in preformed plasma channels in an elongated gas jet. *Phys. Rev. E*, 59(4):R3839–R3842, Apr 1999.

[56] http://www.iceditors.com/.

[57] http://www.microtronicsinc.com/.

[58] http://www.lps.umd.edu/.

[59] Mitsuo Takeda, Hideki Ina, and Seiji Kobayashi. Fourier-transform method of fringe-pattern analysis for computer-based topography and interferometry. *J. Opt. Soc. Am.*, 72(1):156–160, 1982.

[60] http://www.ni.com/labview/.

[61] Marvin A. Schofield and Yimei Zhu. Fast phase unwrapping algorithm for interferometric applications. *Opt. Lett.*, 28(14):1194–1196, 2003.

[62] Milan Kalal and Keith A. Nugent. Abel inversion using fast fourier transforms. *Appl. Opt.*, 27(10):1956–1959, 1988.

[63] Charles Townes and Arthur Schawlow. *Microwave spectroscopy*. McGraw-Hill, 1955.

[64] H Stapelfeldt. Colloquium: Aligning molecules with strong laser pulses. *Reviews of Modern Physics*, 75(2):543–557, APR 2003.

[65] R Velotta, N Hay, MB Mason, M Castillejo, and JP Marangos. High-order harmonic generation in aligned molecules. *Physical Review Letters*, 8718(18), OCT 29 2001.

[66] RA Bartels, TC Weinacht, N Wagner, M Baertschy, CH Greene, MM Murnane, and HC Kapteyn. Phase modulation of ultrashort light pulses using molecular rotational wave packets. *Phys. Rev. Lett.*, 88(1), JAN 7 2002.

[67] S. Varma, Y.-H. Chen, and H.M. Milchberg. Effect of aligned nitrogen molecules on atmospheric propagation of ultrashort laser pulses. *Lasers and Electro-Optics, 2008 and 2008 Conference on Quantum Electronics and Laser Science. CLEO/QELS 2008. Conference on*, pages 1–2, May 2008.

[68] J. P. Heritage, T. K. Gustafson, and C. H. Lin. Observation of coherent transient birefringence in c$s2$ vapor. *Phys. Rev. Lett.*, 34(21):1299–1302, May 1975.

[69] Y.-H. Chen, S. Varma, A. York, and H. M. Milchberg. Single-shot, space- and time-resolved measurement of rotational wavepacket revivals in H-2, D-2, N-2, O-2, and N2O. *Optics Express*, 15(18):11341–11357, SEP 3 2007.

[70] H Harde and D Grischkowsky. Coherent transients excited by subpicosecond pulses of terahertz radiation. *Journal of the Optical Society of America B-Optical Physics*, 8(8):1642–1651, AUG 1991.

[71] LH Xu, RM Lees, ECC Vasconcellos, SC Zerbetto, LR Zink, and KM Evenson. Methanol and the optically pumped far-infrared laser. *IEEE Journal of Quantum Electronics*, 32(3):392–399, MAR 1996.

[72] http://lasers.coherent.com/lasers/sifir-50.

[73] SH Lee, SJ Petuchowski, AT Rosenberger, and TA DeTemple. Synchronous, mode-locked pumping of gas-lasers. *Optics Letters*, 4(1):6–8, 1979.

[74] AT Rosenberger, HK Chung, and TA DeTemple. Sub-T2 optical pulse generation - application to optically pumped far-infrared lasers. *IEEE Journal of Quantum Electronics*, 20(5):523–532, 1984.

[75] BB Hu, XC Zhang, DH Auston, and PR Smith. Free-space radiation from electrooptic crystals. *Applied Physics Letters*, 56(6):506–508, FEB 5 1990.

[76] DH Auston, KP Cheung, and PR Smith. Picosecond photoconducting Hertzian dipoles. *Applied Physics Letters*, 45(3):284–286, 1984.

[77] K.-L. Yeh, M. C. Hoffmann, J. Hebling, and Keith A. Nelson. Generation of 10 mu J ultrashort terahertz pulses by optical rectification. *Applied Physics Letters*, 90(17), APR 23 2007.

[78] Y. Shen, T. Watanabe, D. A. Arena, C.-C. Kao, J. B. Murphy, T. Y. Tsang, X. J. Wang, and G. L. Carr. Nonlinear cross-phase modulation with intense single-cycle terahertz pulses. *Physical Review Letters*, 99(4), JUL 27 2007.

[79] WP Leemans, CGR Geddes, J Faure, C Toth, J van Tilborg, CB Schroeder, E Esarey, G Fubiani, D Auerbach, B Marcelis, MA Carnahan, RA Kaindl, J Byrd, and MC Martin. Observation of terahertz emission from a laser-plasma accelerated electron bunch crossing a plasma-vacuum boundary. *Physical Review Letters*, 91(7), AUG 15 2003.

[80] CM Dion, A Keller, O Atabek, and AD Bandrauk. Laser-induced alignment dynamics of HCN: Roles of the permanent dipole moment and the polarizability. *Physical Review A*, 59(2):1382–1391, FEB 1999.

[81] Arthur Adel and E. F. Barker. The vibrational energy level system of the linear molecule hcn. *Phys. Rev.*, 45(4):277–279, Feb 1934.

[82] Bretislav Friedrich and Dudley Herschbach. Alignment and trapping of molecules in intense laser fields. *Phys. Rev. Lett.*, 74(23):4623–4626, Jun 1995.

[83] C. H. Lin, J. P. Heritage, T. K. Gustafson, R. Y. Chiao, and J. P. McTague. Birefringence arising from the reorientation of the polarizability anisotropy of molecules in collisionless gases. *Phys. Rev. A*, 13(2):813–829, Feb 1976.

[84] Klaus Hartinger and Randy A. Bartels. Single-shot measurement of ultrafast time-varying phase modulation induced by femtosecond laser pulses with arbitrary polarization. *Applied Physics Letters*, 92(2):021126, 2008.

[85] D. V. Kartashov, A. V. Kirsanov, A. M. Kiselev, A. N. Stepanov, N. N. Bochkarev, Yu. N. Ponomarev, and B. A. Tikhomirov. Nonlinear absorption of intense femtosecond laser radiation in air. *Optics Express*, 14(17):7552–7558, AUG 21 2006.

[86] Joseph Oakland Hirschfelder, Charles F. Curtiss, and Byron R. Bird. *Molecular theory of gases and liquids.* Wiley, 1954.

[87] Andrew G. York and H. M. Milchberg. Broadband terahertz lasing in aligned molecules. *Optics Express*, 16(14):10557–10564, JUL 7 2008.

[88] David Griffiths. *Introduction to Quantum Mechanics.* 2nd edition edition, 2005.

[89] V. Renard, M. Renard, A. Rouzée, S. Guérin, H. R. Jauslin, B. Lavorel, and O. Faucher. Nonintrusive monitoring and quantitative analysis of strong laser-field-induced impulsive alignment. *Phys. Rev. A*, 70(3):033420, Sep 2004.

[90] Michael A. Nielsen and Isaac L. Chuang. *Quantum computation and quantum information.* Cambridge University Press, 2000.

[91] S Ramakrishna and T Seideman. Dissipative dynamics of laser induced nonadiabatic molecular alignment. *Journal Of Chemical Physics*, 124(3), JAN 21 2006.

[92] deepthought.umd.edu.

[93] Alex. G. Smith, Walter Gordy, James W. Simmons, and William V. Smith. Microwave spectroscopy in the region of three to five millimeters. *Phys. Rev.*, 75(2):260–263, Jan 1949.

[94] Roger Campargue. *Atomic and Molecular Beams.* Springer, 2000.

[95] Sebastiaan Y. T. Van De Meerakker, Hendrick L. Bethlem, and Gerard Meijer. Taming molecular beams. *Nature Physics*, 4(8):595–602, AUG 2008.

[96] Vinod Kumarappan, Christer Z. Bisgaard, Simon S. Viftrup, Lotte Holmegaard, and Henrik Stapelfeldt. Role of rotational temperature in adiabatic molecular alignment. *The Journal of Chemical Physics*, 125(19):194309, 2006.

[97] DS Elliott and JF Ward. Polarizability anisotropies of CO2, N2O, and OCS from measurements of the intensity-dependent refractive-index in gases. *Physical Review Letters*, 46(5):317–320, 1981.

[98] http://webbook.nist.gov/chemistry/.

[99] Sharly Fleischer, I. Sh. Averbukh, and Yehiam Prior. Isotope-selective laser molecular alignment. *Physical Review A (Atomic, Molecular, and Optical Physics)*, 74(4):041403, 2006.

[100] D. S. Elliott and J. F. Ward. Polarizability anisotropies of c*o*2, *n*2o, and ocs from measurements of the intensity-dependent refractive index in gases. *Phys. Rev. Lett.*, 46(5):317–320, Feb 1981.

[101] Michinori Tanaka, Masanao Murakami, Tomoyuki Yatsuhashi, and Nobuaki Nakashima. Atomiclike ionization and fragmentation of a series of CH3-X (X : H, F, Cl, Br, I, and CN) by an intense femtosecond laser. *Journal Of Chemical Physics*, 127(10), SEP 14 2007.

[102] V. Loriot, P. Tzallas, E. P. Benis, E. Hertz, B. Lavorel, D. Charalambidis, and O. Faucher. Laser-induced field-free alignment of the OCS molecule. *Journal of Physics B-Atomic Molecular and Optical Physics*, 40(12):2503–2510, JUN 28 2007.

[103] KL Wang and DM Mittleman. Metal wires for terahertz wave guiding. *Nature*, 432(7015):376–379, NOV 18 2004.

[104] Markus Walther, Mark R. Freeman, and Frank A. Hegmann. Metal-wire terahertz time-domain spectroscopy. *Applied Physics Letters*, 87(26):261107, 2005.

[105] H Cao and A Nahata. Coupling of terahertz pulses onto a single metal wire waveguide using milled grooves. *Optics Express*, 13(18):7028–7034, SEP 5 2005.

[106] Wenqi Zhu, Amit Agrawal, Hua Cao, and Ajay Nahata. Generation of broadband radially polarized terahertz radiation directly on a cylindrical metal wire. *Optics Express*, 16(12):8433–8439, JUN 9 2008.

[107] K. Y. Kim, B. Yellampalle, G. Rodriguez, R. D. Averitt, A. J. Taylor, and J. H. Glownia. Single-shot, interferometric, high-resolution, terahertz field diagnostic. *Applied Physics Letters*, 88(4):041123, 2006.

[108] http://www.evproducts.com/.